

Copyright

by

Jennifer S. Sobeck

2007

The Dissertation Committee for Jennifer S. Sobeck
certifies that this is the approved version of the following dissertation:

**An Atomic Physics Viewpoint of Stellar Abundance
Analysis**

Committee:

Chris Sneden, Supervisor

Roger Bengtson, Supervisor

John Lacy

James Lawler

Linda Reichl

J. Craig Wheeler

**An Atomic Physics Viewpoint of Stellar Abundance
Analysis**

by

Jennifer S. Sobeck, BS, MA

Dissertation

Presented to the Faculty of the Graduate School of

The University of Texas at Austin

in Partial Fulfillment

of the Requirements

for the Degree of

Doctor of Philosophy

The University of Texas at Austin

May 2007

To my family (Christina, Dad, Emre, Mom, and Nathan) and all women who
endeavor to be physicists

Acknowledgments

I would like to express my immense gratitude and respect to my supervisor, Chris Sneden. He is one of the most phenomenal scientists that I have ever had the pleasure to work with and I hope to continue to do so. His time management skills constantly amaze me and his level of productivity astounds everyone around him. I am also thankful for the occasional nudge that he would give me (plus, the shared affinity for the Onion and other similar types of humor). I would not have become the astronomer that I am today without his guidance.

I would like to heartily thank my co-supervisor, Roger Bengtson. I have benefited enormously from his introduction of Chris Sneden to me. He is a wise and excellent physicist (he would keep me honest with regard to transition probability data and the applicability of my science). He possesses the qualities of patience and perspective (which helped me in the difficult moments; and, I hope to acquire these attributes one day myself). Under his tutelage, I have become a better physicist (and a finer consumer of wheat-type libations).

I am also very grateful to have worked with Bob Kraft. He is one of the finest scientists and human beings that I know. He has shown me how to become an extraordinary scientist while still maintaining a genuine sense of self and humility. He is an inspiration to me and I endeavor to follow his example.

I am deeply indebted to Jim Lawler for his instruction and advice. I am a better spectroscopist as a result of his teaching (and my affiliation with him allows

me to legitimately retain the appellation “atomic physicist”). The collaboration with Jim has renewed my enthusiasm and enjoyment for atomic spectroscopy (which at one time had faded). I hope to continue to work with him in the future (and bring that additional level of accuracy to abundance analyses).

There are three individuals who played key roles in my scientific development: Inese Ivans, Carlos Allende Prieto, and Lars Koesterke. I have benefited tremendously from my interaction with each of these persons. Inese is an exceptional astronomer and I openly admit to aspiring to be like her. Carlos has an unsurpassed knowledge of stellar astronomy and prompted me to pursue directions and avenues which I had not thought of previously. Lars also pushed me to become a better programmer and I thoroughly enjoyed our conversations (I hope to one day develop spectral synthesis programs similar in caliber and quality to his remarkable, still unnamed, code).

I would also like to thank the members of my committee: John Lacy, Linda Reichl, and Craig Wheeler. I have relied on each of these persons at various points in my scientific career. I am very lucky to have been the recipient of their counsel and training.

My officemates Ivan, Pan, and Rob provided a relaxed and enjoyable work environment. I am amazed at their levels of patience and tolerance for a liberal, caffeine-addled, insomniac, fellow astronomer. It was a serendipitous (and altogether wonderful) event to have been placed in the same office with them.

I am deeply grateful for all of the friendships in Astronomy and Physics that I have cultivated over the years. These relationships kept me sane and happy over the unbelievably long stint of time that I spent at UT. Just off the top of my head, thanks to: Amy, Anna, Andrea, Claudia, Dominik, Emek, Fergal, Ian, Magnus, Michelle, Mike, Reid, Sara, Sonia, and Trish (and everyone else that I absent-mindedly forgot to mention).

All my love and gratitude go to my family: Mom, Dad, and Christina. At every stage of my career, they were there in so many ways for me. I can never thank them enough for their laughter, patience, optimism, understanding, advice...and above all, their constant, interminable belief in me.

I want to express my “astronomic” gratitude to my husband Emre. I am not sure he knew what he was in for when he married me. Over the course of these past 5 years, he has remained steadfastly by my side. He has experienced both the high and lows of my scientific career (with boundless empathy and compassion). I would like to thank him in particular for the all of the trips out to the observatory, late nights, cups of coffee, midnight snacks, and movie jokes/quotes. He made this journey so much easier. I love you.

JENNIFER S. SOBECK

The University of Texas at Austin

May 2007

An Atomic Physics Viewpoint of Stellar Abundance Analysis

Publication No. _____

Jennifer S. Sobeck, Ph.D.

The University of Texas at Austin, 2007

Supervisors: Chris Sneden, Roger Bengtson

Element abundance trends with overall metallicity contain vital clues to the formation and evolution of the Galaxy. Abundances may be used to elucidate nucleosynthesis mechanisms and to ascertain rates of Galactic enrichment.

To obtain accurate abundances, several crucial inputs such as high-quality spectroscopic observations, rigorous calculations of line transfer, and precise atomic data (e.g. transition probabilities) are necessary. The current work endeavors to improve abundance values for key elements with a four-fold approach: accumulation of hundreds of high-resolution stellar spectra in order to commence a systematic and thorough Manganese abundance derivation in cluster and halo field stars; re-

determination of the neutral chromium oscillator strengths and application of this data to stellar abundance analyses; modification of a radiative line transfer code in order to yield accurate abundances from evolved stars; and semi-empirical derivation of transition probabilities to allow for the utilization of spectral features in the red visible and infrared wavelength ranges for abundance determinations.

The first comprehensive investigation of manganese in globular clusters is done in this work. A subsolar Mn abundance trend for both halo globular cluster and field stars is found. The analysis shows that for the metallicity range $-0.7 > [\text{Fe}/\text{H}] > -2.7$ stars of 19 globular clusters have a mean relative abundance of $\langle [\text{Mn}/\text{Fe}] \rangle = -0.37 \pm 0.01$ ($\sigma = 0.10$), a value in agreement with that of the field stars: $\langle [\text{Mn}/\text{Fe}] \rangle = -0.36 \pm 0.01$ ($\sigma = 0.08$). Remarkably, the $\langle [\text{Mn}/\text{Fe}] \rangle$ ratio remains constant in both stellar populations over a 2 orders of magnitude span in metallicity.

Next, the present study employed branching fraction measurements from Fourier transform spectra in conjunction with published radiative lifetimes to determine transition probabilities for 263 lines of neutral chromium. These laboratory values are used to derive a new photospheric abundance for the Sun: $\log \epsilon(\text{Cr I})_{\odot} = 5.64 \pm 0.01$ ($\sigma = 0.07$). In addition, oscillator strengths for singly-ionized chromium recently reported by the FERRUM Project are employed to determine: $\log \epsilon(\text{Cr II})_{\odot} = 5.77 \pm 0.03$ ($\sigma = 0.13$). No indications of departures from LTE are found in the neutral chromium abundances.

The current work then takes advantage of the fact that transition metals exhibit relatively pure LS coupling and employs standard formulae to yield semi-empirical oscillator strengths. These data were then compared to experimental gf values in order to assess accuracy.

Finally, this study undertakes a new abundance investigation of the RGB and RHB stars of the M15 globular cluster. A detailed examination of the both

the metallicity and n-capture elements is performed. This work appears to confirm that star-to-star abundance variations do occur among the M15 giants (which was initially observed by Sneden et al. 1997, 2000).

Contents

Acknowledgments	v
Abstract	viii
List of Tables	xv
List of Figures	xix
Chapter 1 Introduction	1
1.1 Manganese Abundance Determination in Cluster and Field Stars . . .	3
1.2 Transition Probabilities of Neutral Chromium	5
1.3 Semi-Empirical Derivation of Oscillator Strengths from Red Visible and Near Infrared Spectral Features	6
1.4 Abundance Variation in Stars of the Globular Cluster M15	6
Chapter 2 Abundance Determination of Manganese in Globular Clus- ter and Field Stars	8
2.1 Introduction	8
2.2 Observations and Data Reduction	9
2.3 Analysis	12

2.3.1	Model Atmospheres and Techniques	14
2.3.2	Line Parameters	36
2.4	Results	40
2.4.1	Error Analysis	43
2.4.2	M71	47
2.4.3	Comparison of Cluster Results: NGC 6528 and C261	48
2.4.4	Other Mn Abundance Analyses	49
2.5	Discussion	51
Chapter 3 Determination of Neutral Chromium Oscillator Strengths		56
3.1	Radiative Lifetime Measurement Summary	56
3.2	Branching Fractions and Atomic Transition Probabilities	60
3.2.1	Grating Spectrometer Measurements	76
3.2.2	Theoretical Transition Probabilities	77
3.2.3	Comparison to Previous Studies	77
3.3	Solar and Stellar Chromium Abundances	81
3.3.1	Inclusion of Oscillator Strengths for Singly-Ionized Chromium from the FERRUM Project	83
3.3.2	Line Selection and Analysis	83
3.3.3	The Solar Photospheric Chromium Abundance	90
3.3.4	No Detection of non-LTE Effects in Excitation for Neutral Chromium	94
3.3.5	Chromium Abundances in Other Stars	97
3.3.6	Chromium Ionization Imbalance Result of Departures from LTE?	99
3.4	Conclusion	102

Chapter 4	Semi-Empirical Derivations of Infrared Wavelength Transition Probabilities	104
4.1	Introduction	104
4.2	Key Relations in Oscillator Strength Determinations	105
4.3	Derivation of Transition Probabilities for Pure LS Multiplets	107
4.4	Accuracy Determination and Potential Applications	109
Chapter 5	Abundance Investigation of M15 Red Giant Branch and Horizontal Branch Stars	113
5.1	Introduction	113
5.2	Observations and Abundance Analysis	114
5.3	Line Formation in Low Metallicity, Cool Giants	115
5.4	The Difference Equation Approach to the Milne-Eddington Problem	118
5.5	Short Characteristic Solution of Line Transfer	121
5.6	Elimination of Abundance with Wavelength Trend	123
5.7	Presentation of Results and Discussion	126
Chapter 6	Conclusions and Future Study	135
Appendix A	Short Characteristics Subroutine for the MOOG Program	138
A.1	Introduction	138
A.2	Shortcharac.f Subroutine	138
Bibliography		149
Bibliography		150

List of Tables

2.1	LTG Observational Data	10
2.2	Outside Source Cluster Observational Data	11
2.3	LTG Stellar Model Parameters and Individual [Fe/H] and [Mn/Fe] Values	15
2.3	LTG Stellar Model Parameters and Individual [Fe/H] and [Mn/Fe] Values	16
2.3	LTG Stellar Model Parameters and Individual [Fe/H] and [Mn/Fe] Values	17
2.3	LTG Stellar Model Parameters and Individual [Fe/H] and [Mn/Fe] Values	18
2.3	LTG Stellar Model Parameters and Individual [Fe/H] and [Mn/Fe] Values	19
2.3	LTG Stellar Model Parameters and Individual [Fe/H] and [Mn/Fe] Values	20
2.3	LTG Stellar Model Parameters and Individual [Fe/H] and [Mn/Fe] Values	21
2.3	LTG Stellar Model Parameters and Individual [Fe/H] and [Mn/Fe] Values	22

2.3	LTG Stellar Model Parameters and Individual [Fe/H] and [Mn/Fe] Values	23
2.3	LTG Stellar Model Parameters and Individual [Fe/H] and [Mn/Fe] Values	24
2.3	LTG Stellar Model Parameters and Individual [Fe/H] and [Mn/Fe] Values	25
2.3	LTG Stellar Model Parameters and Individual [Fe/H] and [Mn/Fe] Values	26
2.3	LTG Stellar Model Parameters and Individual [Fe/H] and [Mn/Fe] Values	27
2.3	LTG Stellar Model Parameters and Individual [Fe/H] and [Mn/Fe] Values	28
2.3	LTG Stellar Model Parameters and Individual [Fe/H] and [Mn/Fe] Values	29
2.3	LTG Stellar Model Parameters and Individual [Fe/H] and [Mn/Fe] Values	30
2.3	LTG Stellar Model Parameters and Individual [Fe/H] and [Mn/Fe] Values	31
2.4	External Data Source Stellar Model Parameters and Individual [Fe/H] and [Mn/Fe] Values	32
2.4	External Data Source Stellar Model Parameters and Individual [Fe/H] and [Mn/Fe] Values	33
2.4	External Data Source Stellar Model Parameters and Individual [Fe/H] and [Mn/Fe] Values	34

2.4	External Data Source Stellar Model Parameters and Individual [Fe/H] and [Mn/Fe] Values	35
2.5	Line Parameters	39
2.6	LTG Cluster Mean Abundances	42
3.1	Radiative Lifetimes of 65 Cr I Levels from LIF Measurements	58
3.1	Radiative Lifetimes of 65 Cr I Levels from LIF Measurements	59
3.1	Radiative Lifetimes of 65 Cr I Levels from LIF Measurements	60
3.2	FTS Spectra Chosen for Branching Fraction Determination	62
3.3	Atomic Transition Probabilities for Cr I Organized by Increasing Wavelength in λ_{air}	65
3.3	Atomic Transition Probabilities for Cr I Organized by Increasing Wavelength in λ_{air}	66
3.3	Atomic Transition Probabilities for Cr I Organized by Increasing Wavelength in λ_{air}	67
3.3	Atomic Transition Probabilities for Cr I Organized by Increasing Wavelength in λ_{air}	68
3.3	Atomic Transition Probabilities for Cr I Organized by Increasing Wavelength in λ_{air}	69
3.3	Atomic Transition Probabilities for Cr I Organized by Increasing Wavelength in λ_{air}	70
3.3	Atomic Transition Probabilities for Cr I Organized by Increasing Wavelength in λ_{air}	71
3.3	Atomic Transition Probabilities for Cr I Organized by Increasing Wavelength in λ_{air}	72

3.3	Atomic Transition Probabilities for Cr I Organized by Increasing Wavelength in λ_{air}	73
3.3	Atomic Transition Probabilities for Cr I Organized by Increasing Wavelength in λ_{air}	74
3.3	Atomic Transition Probabilities for Cr I Organized by Increasing Wavelength in λ_{air}	75
3.3	Atomic Transition Probabilities for Cr I Organized by Increasing Wavelength in λ_{air}	76
3.4	EW Measurements for the Survey Stars	85
3.4	EW Measurements for the Survey Stars	86
3.4	EW Measurements for the Survey Stars	87
3.4	EW Measurements for the Survey Stars	88
3.5	Solar Photospheric Cr I and Cr II Abundances for Different Models ^a	91
3.6	Comparison to the Blackwell et al. 1989 Solar Abundances ^a	96
4.1	Comparison of Semi-Empirically and Laboratory-Derived Transition Probabilities for Cr I Multiplets	110
4.2	Prospective Cr I Multiplets for Transition Probability Calculation .	111
4.2	Prospective Cr I Multiplets for Transition Probability Calculation .	112
5.1	M15 Stellar Model Atmospheric Parameters	114
5.2	Neutron Capture Abundance Values for the M15 Stars	127

List of Figures

2.1	Comparison of the spectra from globular clusters of differing metallicities. Note that temperature is roughly the same for all of the spectra. The three Mn and two Fe lines used in the abundance analysis are indicated in this figure. As metallicity decreases, some of the spectral features become undetectable.	13
2.2	Comparison of the synthetic and observed spectrum for one M13 star. The top panel displays the observed and synthetic spectra for a wavelength range that encompasses the 6016 and 6021 Å Mn lines. The bottom panel focuses on the 6021 Å Mn feature and highlights the effects of incremental changes in abundance. Changes as small as 0.2 dex cause distinct variation in the synthesized spectrum.	37

2.3	Correlation of $[\text{Mn}/\text{Fe}]$ with $[\text{Fe}/\text{H}]$ for different stellar samples. The top panel displays all of the abundances for the stars of the 19 globular cluster data sample. The middle panel shows the average $[\text{Mn}/\text{Fe}]$ and $[\text{Fe}/\text{H}]$ values for each globular cluster (with associated error bars). Field star abundances are also shown in this panel; label F00 indicates data from Fulbright (2000) and label S04 signifies data from Simmerer et al. (2004). The points for M15 and Pal 12 are designated as they represent the extremes in metallicity for the halo globular clusters of this data set. Moreover, M71 is denoted as its $\langle[\text{Mn}/\text{Fe}]\rangle$ is not consistent with the other globular cluster data points. The bottom panel presents globular cluster values from the literature. Note that the literature Mn abundances agree fairly well with those of the current study. Also, the Mn abundance for M71 from the current data sample is set aside in favor of the value published by Ramirez & Cohen (2002), as explained in §2.4	41
2.4	Interdependence of $[\text{Mn}/\text{Fe}]$ and S/N for the LTG data sample. The top panel presents the entire S/N range of the LTG globular cluster data set as well as those points with $\text{S/N} > 85$. The bottom panel illustrates the correlation of Mn abundances with S/N for LTG globular cluster and field data in the metallicity range $-0.7 > [\text{Fe}/\text{H}] > -2.7$.	44
2.5	Box plots for nine representative globular clusters. For each cluster, the boxed region encompasses the interquartile (middle 50%) of its $[\text{Mn}/\text{Fe}]$ data. Also featured are the median (horizontal line), range (vertical lines; excludes outliers), and outliers (an outlier has a value greater than 1.5 times the interquartile range). The ordering of the clusters is in decreasing $[\text{Fe}/\text{H}]_{\text{avg}}$	45

2.6	Box plots for selected globular clusters. For a few cases, averaging our derived $[Fe/H]$ values with those reported in the literature serves to reduce the spread in metallicity. As a consequence of this averaging process, the median $[Fe/H]$ value for the cluster increases. In general, marginal benefit is gained from the averaging process (as clearly illustrated by M3).	46
2.7	Average abundance ratios with associated standard deviation values for some of the Fe-peak and α -elements in the range $-0.7 > [Fe/H] > -2.7$. Globular cluster data are obtained from the LTG references. The Mn values are provided by the current study. Data for halo field stars for every element except Cu and Co are taken from Gratton et al. (2003) and Fulbright (2000). Cu field star data are obtained from Mishenina et al. (2002) and Co field star data are taken from Johnson (2002). Interestingly, there is a lack of Co data for globular clusters. Note that in almost every case, the average values for globular cluster and halo field stars are roughly equal to one another.	52
3.1	Comparison of the oscillator strength values from the current work to those of Tozzi et al. (1985). The upper panel shows the difference between the $\log(gf_{Tozzi})$ and $\log(gf_{Sobeck})$ as a function of wavelength. The middle panel displays the difference versus the $\log(gf_{Sobeck})$ values. The bottom panel illustrates the difference as a function of upper energy level (E_{upper}).	79

3.2	Comparison of the oscillator strength values from this study to those of Blackwell et al. (1984, 1986). The upper panel shows the difference between the $\log(gf_{Blackwell})$ and $\log(gf_{Sobeck})$ as a function of wavelength. The middle panel displays the difference versus the $\log(gf_{Sobeck})$ values. The bottom panel illustrates the difference as a function of upper energy level (E_{upper}).	80
3.3	Comparison of the oscillator strength values from the present study to those of the NIST compilation. The upper panel shows the difference between the $\log(gf_{NIST})$ and $\log(gf_{Sobeck})$ as a function of wavelength. The middle panel displays the difference versus the $\log(gf_{Sobeck})$ values. The bottom panel illustrates the difference as a function of upper energy level (E_{upper}).	82
3.4	Relative strength factors (RSF) as defined by $\log(gf) - \theta\chi$ for the Cr I transitions. Reduced widths of weak lines should be proportional to these factors. For these computations, $\theta = 0.87$, the inverse of the effective temperature of the Sun. The squares indicate the RSF for all 263 Cr I lines and the stars designate those Cr I lines actually used in the derivation of the solar abundance. The 5844.59 Å line is specially noted in the plot as it is has a small RSF yet is still detectable in the solar spectrum.	89

3.5	Plot of solar Cr I abundances as a function of excitation potential (χ), reduced width ($\log(RW)$), and wavelength (λ). Encircled in each of the three panels are the two most erroneous abundance values. Note that these two abundance data points correspond to lines that originate from major branches. Consequently, the error in these two points cannot be attributed to oscillator strength uncertainties. . . .	93
3.6	Branching Fractions for the Cr I and Cr II lines used in the solar abundance analysis. The lower panel (which is an enlarged view of the upper) shows the average abundance from the Cr I transitions (dashed line) as well as that from the Cr II transitions (dash-dotted line).	101
5.1	Opacity contribution as a function of wavelength for three different models. A typical layer of the atmosphere is chosen for this comparison and all stars have a metallicity of $[M/H] = -1.0$	116
5.2	Ray propagating on a two-dimensional Cartesian grid.	122
5.3	Plot of the Fe I abundance as a function of wavelength for the RGB tip star K341 (model atmosphere parameters: $T_{\text{eff}} = 4320$ K; $\log g = 0.25$; $[\text{Fe}/\text{H}] = -2.2$).	124
5.4	Plot of the Fe I abundance as a function of wavelength for the RHB star B412 (model atmosphere parameters: $T_{\text{eff}} = 6200$ K; $\log g = 2.70$; $[\text{Fe}/\text{H}] = -2.5$).	125
5.5	Plot of light element abundances as a function of metallicity for the M15 RGB stars (red, filled circles) and RHB stars (blue, open circles). 129	

5.6	Plot of n-capture element abundances as a function of temperature for the M15 RGB stars (red, filled circles) and RHB stars (blue, open circles).	130
5.7	Plot of n-capture relative abundances as a function of metallicity for the M15 RGB stars (red, filled circles) and RHB stars (blue, open circles).	131
5.8	Abundance variation in the n-capture elements. The plot also includes the Otsuki et al. 2006 M15 RGB abundances. The one star that the Otsuki et al. and the present study have in common is indicated as a black dot encircled in red.	132
5.9	Abundance as a function of atomic number for a few n-capture elements. All values are normalized to the average Nd abundance of the M15 RGB stars. The plot also includes the HD 221170 abundances from Ivans et al. (2006).	134

Chapter 1

Introduction

Do not look at stars as bright spots only. Try to take in the vastness of the universe.

-Maria Mitchell

Creation of basic elements hydrogen (^1H and ^2H), helium (^3He and ^4He), and lithium (^7Li) was done by Big Bang Nucleosynthesis. Most other element manufacture is the result of nuclear reactions that occur in stellar environments (note that ^9Be , ^{10}B , and ^{11}B are the exceptions). Stars are the primary source of Galactic chemical enrichment.

Element production occurs throughout the lifetime of a star. Specific examples of stellar nucleosynthesis include the proton-proton chain and the triple- α process (phase: Main Sequence (MS); product nuclei: $A < 60$); the slow neutron capture process (phase: Asymptotic Giant Branch (AGB); product nuclei: $A \geq 90$); and, the rapid neutron capture process (phase: massive star progenitor/Type II supernova (SNe); product nuclei: $A \leq 130 - 140$ and $A \geq 130 - 140$) (Truran et al. 2002). Stars inject elements into the surrounding interstellar medium predominantly

via three mechanisms: slow planetary nebula cast off, pressure-driven winds, and explosive SNe events.

The chemical compositions of stars manifest the nucleosynthetic contributions from previous generations and consequently, trace the evolutionary history of the Galaxy. Spectroscopic abundance analysis is used to deduce the makeup of stars. Trends in element abundances over the range of metallicity allow for the comparison and differentiation of stellar populations. Abundances ratios may be used to determine the origin of the elements and establish Galactic structural formation patterns.¹

Accurate abundance derivations rely on four main components: spectroscopic observations, atomic/molecular data, model stellar atmospheres, and line formation computations. Acquisition of high-resolution spectroscopic data is relatively straightforward as the technology of telescope/detector combinations has improved vastly over the past several decades. High signal-to-noise (S/N) observations of extremely faint targets such as outer halo and extragalactic stars may now be done at high resolution (with the implication that instrumental profiles are roughly equivalent to intrinsic stellar line widths). For a spectral transition associated with an element, the relevant atomic data include: ionization energies, partition functions, wavelengths, energy levels, isotopic shifts, hyperfine splitting, oscillator strengths, and damping constants. Most abundance investigations employ stellar model atmospheres which exhibit the general characteristics of a homogeneous, multi-layered, and hydrostatic structure. For both model atmospheres and spectral line formation codes (employed in typical abundance work), the fundamental assumption is that that local thermodynamic equilibrium (LTE) conditions in an one-dimensional environment prevail.

¹Standard abundance notation is employed in that $[X/Y] \equiv \log_{10}(N_X/N_Y)_{star} - \log_{10}(N_X/N_Y)_{sun}$

This dissertation addresses three of the four criteria mentioned in the previous paragraph for high-quality abundance analyses. Chapter 2 depicts the assembly of a large collection of high resolution stellar spectra in order to investigate the abundance of manganese in globular cluster giants (stellar relics located the Galactic halo). Chapter 3 details the use of laboratory measurements to improve the oscillator strengths for the neutral species of chromium and the application of these data to abundance derivations. Chapter 4 reports the initial efforts to employ LS multiplet analysis in the calculation of transition probabilities in the red visible and infrared wavelength regime. Chapter 5 describes the modification of a standard spectral line analysis code to treat isotropic, coherent scattering which in turn permits the derivation of accurate abundances of low temperature, low surface gravity stars. Finally, Chapter 6 contains possible directions for future work. Brief synopses of chapters 2-5 follow below.

1.1 Manganese Abundance Determination in Cluster and Field Stars

With the exception of ω Cen (e.g. Norris & Da Costa 1995), stars of individual globular clusters display monometallicity, i.e. members of a globular cluster possess approximately the same $[\text{Fe}/\text{H}]$ value. Elements of the proton-capture group (C, N, O, Na, Mg, and Al) exhibit large star-to-star abundance variations in most globular clusters, and these discrepancies are inordinately large as compared to those seen in halo field stars (Gratton et al. 2004, and references therein). In contrast, members of the α -element (e.g. Si, Ca, and Ti) and neutron-capture element (e.g. Y, Ba, La, and Eu) groups display similar mean abundance patterns in most globular cluster and halo field stars. Likewise, the relative abundances of several Fe-peak elements

(notably Sc, V, Cr, and Ni) appear to be almost identical in the two stellar populations. The vast majority of the Fe-group members have roughly solar abundance ratios with two exceptions: copper and manganese. The relative abundance of Cu is known to be exceedingly subsolar in metal-poor field stars (at metallicities $[\text{Fe}/\text{H}] < -2$, $[\text{Cu}/\text{Fe}]$ approaches -1 ; Sneden et al. 1991a, Mishenina et al. 2002). An analogous deficiency of Cu in globular cluster stars has recently been reported by Simmerer et al. (2003). In the two stellar groups, the trend of $[\text{Cu}/\text{Fe}]$ with $[\text{Fe}/\text{H}]$ is identical within the limit of observational uncertainty.

Mn also has an established abundance deficiency in metal-poor stars. Helfer et al. (1960) and Wallerstein (1962) were the first to report sub-solar Mn and in 1978, Beynon verified these initial observations. Later, Gratton (1989) improved Mn abundance determinations by employing hyperfine structure (HFS) data from Booth et al. (1984) to derive $\langle [\text{Mn}/\text{Fe}] \rangle = -0.34 \pm 0.06$ for stars of metallicity $[\text{Fe}/\text{H}] < -1$. Three factors have hindered Mn abundance determinations: the lack of adequate hyperfine structure computations, the uncertainty of damping parameter values, and the absence of available transitions in the red portion of the visible spectrum (Gratton 1989; Prochaska & McWilliam 2000).

Several surveys of metal-poor field stars have derived highly accurate $[\text{Mn}/\text{Fe}]$ values (Gratton & Sneden 1991; McWilliam et al. 1995; Johnson 2002; Francois et al. 2003; Cohen et al. 2004b). However, a systematic and comprehensive study of Mn abundances in globular cluster stars has not yet taken place. This dissertation presents the first-ever major abundance investigation of Mn in stars of globular and open clusters.

1.2 Transition Probabilities of Neutral Chromium

Chromium is a member of the iron peak group ($Z = 24$) with one dominant, naturally occurring isotope (^{52}Cr). The synthesis of chromium is directly dependent on iron as the parent nucleus of ^{52}Cr is ^{52}Fe (e.g. Nakamura et al. 1999). Prior to the mid-90's, abundance surveys found $[\text{Cr}/\text{Fe}] \simeq 0$ for stars across the entire range of metallicity (e.g. Magain 1989, Ryan et al. 1991, Gratton & Sneden 1991). Taking into consideration both the nucleosynthetic linkage and the observational data, $[\text{Cr}/\text{Fe}]$ was believed to remain at its solar ratio independent of metallicity. However McWilliam et al. (1995) examined abundances in a sample of extremely metal-poor stars, finding that $[\text{Cr}/\text{Fe}] \sim 0$ until approximately $[\text{Fe}/\text{H}] = -2.5$, and then starts to decrease steadily with $[\text{Fe}/\text{H}]$. Additional observations by Cayrel et al. (2004) and Aoki et al. (2005) supported this finding. Note that most of these abundance analyses employed only Cr I transitions.

The literature contains multiple studies of Cr oscillator strengths. The major investigations include those of Wujec & Weniger (1981; Cr I/II), Tozzi et al. (1985; Cr I) and Blackwell et al. (1984a, 1986; Cr I). However, this species has not been the subject of a large-scale laboratory study in the past 20 years. A new investigation of transition probabilities for singly-ionized chromium from the FERRUM Project has recently been published (Nilsson et al. 2006). With these Cr II results as additional motivation, this dissertation undertakes a new comprehensive study of Cr I oscillator strengths. Unlike prior surveys of the solar photosphere, this work uses high-quality transition probability data for both Cr I and Cr II to determine the abundance and to examine closely its ionization equilibrium.

1.3 Semi-Empirical Derivation of Oscillator Strengths from Red Visible and Near Infrared Spectral Features

Two factors encourage the initiation of abundance investigations in the red visible and near infrared (NIR) spectral ranges: the advancement NIR detector technology and the desire for high S/N spectra of prime target objects (red giant branch stars emit peak flux in these wavelength regimes). Transition probabilities for many red and infrared lines are either inaccurate or not known. In conjunction with laboratory measurements of radiative lifetimes, LS multiplet calculations may be used to derive oscillator strengths for the high spin states of transition metals. In this dissertation, a preliminary code is developed to calculate semi-empirical gf values for Cr I lines. The ultimate goal of the code is to compute reliable oscillator strengths for infrared transitions (which will be employed in abundance analyses).

1.4 Abundance Variation in Stars of the Globular Cluster M15

There are two principal types of neutron capture reactions, the slow (*s*-) process (which is further subdivided into weak and main scenarios) and the rapid (*r*-) process. The *r*-process transpires in Type II SNe (a neutron-rich environment) while the main *s*-process takes place in asymptotic giant branch (AGB) stars and the weak *s*-process occurs in late-evolutionary stage massive stars (Travaglio et al. 2004). An enhancement of the *r*-process component of a neutron capture element in a stellar population would serve as an (additional) indicator of the prevalence of Type II SNe

events. The derivation of an [r-process/s-process] ratio would directly quantify the relative contributions of high-mass and intermediate-mass (AGB) stars (Travaglio et al. 2004; Gratton et al. 2004).

The surveys of Sneden et al. (1997, 2000) found star-to-star abundance scatter of the light elements and the neutron-capture elements in M15 Red Giant Branch (RGB) stars. Further examination of three select RGB tip stars revealed a distinct r-process nucleosynthetic signature (consistent with a scaled solar system r-process abundance distribution).

As part of a general survey of metal-poor red horizontal branch (RHB) stars, Preston et al. (2006) observed six RHB members of M15. They detected some star-to-star abundance scatter in both the light and n-capture elements. However, Preston et al. found that the mean metallicity of these stars was significantly lower (by roughly 0.2 dex) than their RGB counterparts. RHB stars provide interesting comparisons to RGB tip stars as they have temperatures bracketing turn-off stars and surface gravities similar to red giants.

Three factors motivate the M15 efforts of this dissertation: availability of new high-quality sets of oscillator strength data (in particular for n-capture elements), potential reconciliation of abundances of stars from a variety of evolutionary states, and incorporation of a methodology to properly consider isotropic, coherent scattering in stellar atmospheres (the Milne-Eddington Problem).

Chapter 2

Abundance Determination of Manganese in Globular Cluster and Field Stars

2.1 Introduction

Mn abundances for several hundred cluster and field stars in the metallicity range of $0.0 \geq [Fe/H] \geq -2.7$ are reported in this dissertation. The intent of the survey is two-fold: first, ascertain whether globular cluster stars have the same Mn abundance as stars of the halo field; and second, confirm the Mn abundance trend across the entire metallicity spectrum, as well as across the stellar populations, in order to further resolve the nucleosynthetic origin of this element. §2.2 relays the particulars about each data set and characterizes the general nature of the data. A justification of line selection and a description of the analysis is found in §2.3. An account of all abundance values is given in §2.4. Finally in §2.5, a discussion of these Mn results

ensues.

2.2 Observations and Data Reduction

In this study, Mn abundance measurements were made in three stellar populations: globular clusters, open clusters, and the halo field. Spectroscopic and equivalent width data were acquired from numerous sources. A significant portion of the globular cluster and halo field data were gathered by the Lick-Texas group (LTG). These LTG data constitute a basis set for our Mn abundance survey. Table 2.1 lists the relevant observational parameters and literature sources for the LTG data. Cluster sample size varies from as few as 2 to as many as 23 stars. The two field star surveys each have a sample size in excess of 80 stars. Stars in the field data sample exist in a variety of evolutionary states whereas the bulk of the globular cluster data are red giants. Three facilities were used for the LTG observations: the Keck I 10.0 m telescope equipped with the High Resolution Echelle Spectrometer (HIRES; Vogt et al. 1994), the Lick 3.0 m telescope equipped with the Hamilton spectrograph (Vogt 1987), and the McDonald 2.7 m telescope equipped with the “2d-coudé” spectrograph (Tull et al. 1995). For the various instrument configurations, the resolution ($R \equiv \lambda/\Delta\lambda$) ranges from 30,000 to 60,000, and the estimated signal-to-noise ratio (S/N) varies between 25 and 180. The software packages IRAF¹ and SPECTRE (Fitzpatrick & Sneden 1987) were used for standard data reduction processes such as bias and flat-field correction, order extraction, cosmic ray elimination, continuum adjustment, and wavelength correction.

The remainder of the globular and open cluster spectra were obtained from

¹IRAF is distributed by the National Optical Astronomy Observatories, which are operated by the Association of Universities for Research in Astronomy, Inc., under cooperative agreement with the National Science Foundation.

Table 2.1. LTG Observational Data

Cluster	Program Stars ^a	Instrument ^b	Reference ^c	S/N Range ^d
NGC 5272 (M3)	20	Keck(45)	1	40-150 D
NGC 5904 (M5)	8	Lick(30)	2	25-145 A
	23	Keck(45)		
NGC 6121 (M4)	20	McD(30:60)	3	40-170 B
NGC 6205 (M13)	17	Lick(30)	4	65-180 A
NGC 6254 (M10)	12	Lick(30)	5	60-180 A
NGC 6341 (M92)	4	Keck(45)	6	60-85 A
NGC 6838 (M71)	10	Lick(30)	7	55-85 A
NGC 7006	6	Keck(45)	8	55-95 B
NGC 7078 (M15)	5	Keck(45)	9	75-150 C
	6	Lick(50)		
Pal 5	4	Keck(34)	10	60-100 B
Halo Field Survey	130	Lick(50)	11	40-240 F
	*	Keck(45)		
	*	ESO (40)		
Halo Field Survey	86	McD(60)	12	≈100 E

^aNote that the number of program stars does not always equal those found in the original paper. In some cases, the S/N ratio was too low in specified wavelength range to obtain a [Mn/Fe] ratio.

^bESO (50): ESO 3.6m telescope-CASPEC spectrograph with $R \simeq 40,000$; Keck(34), Keck (45): Keck I 10.0m telescope-HIRES spectrograph with $R \simeq 34,000$ or $R \simeq 45,000$; Lick(30): Pre-1995 configuration of Lick 3.0m telescope-Hamilton echelle with $R \simeq 30,000$; Lick(50): Current configuration of Lick 3.0m telescope-Hamilton echelle with $R \simeq 50,000$; McD(30-60): McDonald 2.7m telescope-”2d-coudé” with $R \simeq 30,000$ or $R \simeq 60,000$.

^c(1) Sneden et al. 2004. (2) Ivans et al. 2001. (3) Ivans et al. 1999. (4) Kraft et al. 1997. (5) Kraft et al. 1995. (6) Shetrone et al. 1998. (7) Sneden et al. 1994. (8) Kraft et al. 1998. (9) Sneden et al. 1997. (10) Smith et al. 2002. (11) Fulbright 2000. (12) Simmerer et al. 2004.

^dApproximate S/N at A: 6300 Å; B: 6350 Å; C: 6363 Å; D: 6460 Å; E: 4100 Å; F: 5500 Å.

Table 2.2. Outside Source Cluster Observational Data

Cluster	Program Stars ^a	Instrument ^b	Reference ^c	S/N Range ^d
Cr 261	4	CTIO(30)	1	75-100
NGC 288	13	CTIO(30)	2	60-125 B
NGC 362	12	CTIO(30)	2	70-95 B
NGC 3201	14	CTIO(30)	3	40-70 C
NGC 6287	2	CTIO(30)	4	\simeq 95
NGC 6293	2	CTIO(30)	4	95 \sim 100
NGC 6528	3	VLT	5	30-40
NGC 6541	2	CTIO(30)	4	95 \sim 135
NGC 6705 (M11)	6	CTIO(24)	6	85-130
	4	APO(34)		
NGC 6752	4	VLT(40:60)	7, 8	\simeq 100 B
Pal 12	4	Keck(34)	9	>100 A

^aNote that the number of program stars does not always equal those found in the original paper. In some cases, the S/N ratio was too low in specified wavelength range to obtain a [Mn/Fe] ratio.

^bKeck(34): Keck I 10.0m telescope-HIRES spectrograph with $R \simeq 34,000$; CTIO(24), CTIO(30): CTIO 4.0m telescope-echelle spectrograph with $R \simeq 24,000$ or $R \simeq 30,000$; VLT(40:60): VLT telescope-UVES spectrograph with $R \simeq 40,000$ or $R \simeq 60,000$; APO(34): APO 3.5m telescope-echelle spectrograph with $R \simeq 34,000$.

^c(1) Friel et al. 2003. (2) Shetrone & Keane 2000. (3) Gonzalez & Wallerstein 1998. (4) Lee & Carney 2002. (5) Zoccali et al. 2004. (6) Gonzalez & Wallerstein 2000. (7) Grundahl et al. 2002. (8) Yong et al. 2005. (9) Cohen 2004a.

^dApproximate S/N at A: 5865 Å; B: 6700 Å; C: 7500 Å

several external sources. Data contributors, as well as observational details, are found in Table 2.2. These data were collected at several facilities: the Very Large Telescope (VLT), Apache Point Observatory (APO), Cerro Tololo Inter-American Observatory (CTIO), and Keck. The various telescope-spectrograph combinations yielded resolutions of $24,000 \leq R \leq 60,000$ and S/N values between 30 and 135. A variety of data reduction and analysis programs were used by the contributors, and for further details the reader should consult the original references (as listed in Table 2.2).

2.3 Analysis

Line selection was based on metallicity and effective temperature parameters. A considerable number of the globular cluster and halo field stars in the data sample have $T_{\text{eff}} \leq 4850$ K. Accordingly, analysis of the strong Mn lines at 4030 Å and 4823 Å was not feasible due to the flux constraints of the data and the probable saturation of these features. In addition, most extant cluster spectra do not extend to the blue-violet wavelength region.

To ascertain Mn abundance in these stars, a wavelength range of 6000-6030 Å was chosen, which encompasses three Mn I spectral features at 6013.51, 6016.64, and 6021.82 Å. These lines are the sole strong transitions of Mn in the yellow-red spectral regime. Two Fe lines at 6024.06 and 6027.05 Å which are roughly of the same excitation potential as the Mn features, were employed for a local iron abundance determination. The use of these nearby Fe transitions eliminates possible discrepancies in continuous opacity and issues with regard to first-order continuum placement. And although the convenience of these two lines must not be understated (as they lie on the same spectral order as the three Mn features), our goal was to

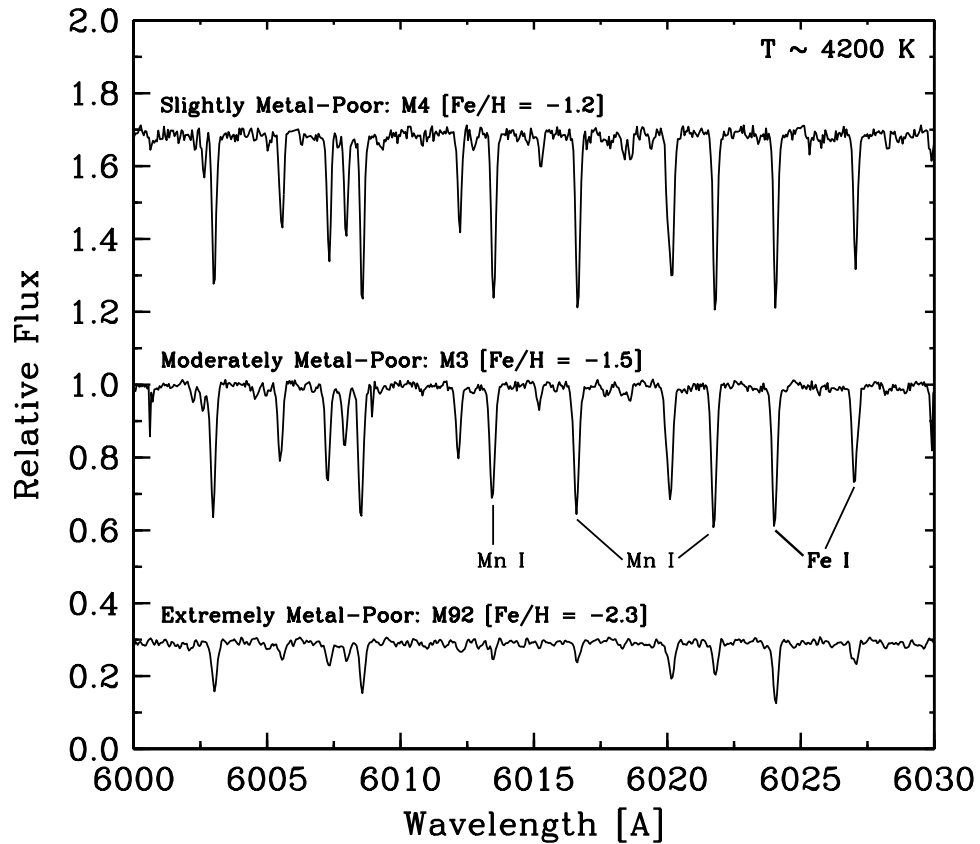


Figure 2.1 Comparison of the spectra from globular clusters of differing metallicities. Note that temperature is roughly the same for all of the spectra. The three Mn and two Fe lines used in the abundance analysis are indicated in this figure. As metallicity decreases, some of the spectral features become undetectable.

obtain local $[\text{Fe}/\text{H}]$ values for the $[\text{Mn}/\text{Fe}]$ determination, not to replace the more extensive $[\text{Fe}/\text{H}]$ assessments done in previous LTG studies. Figure 2.1 features all of the lines used for analysis and roughly illustrates line strength as a function of metallicity.

2.3.1 Model Atmospheres and Techniques

For the LTG data, stellar atmospheric parameters as reported by the original papers were adopted. Model stellar atmospheres were employed that were originally generated for those papers from the MARCS (Gustaffson et al. 1975) and ATLAS (Kurucz 1993) codes. Table 2.3 presents the T_{eff} , v_t , and $\log g$ numbers for the LTG data set. Model atmospheres did not normally accompany the data from outside sources. The stellar atmospheric parameters as reported by the contributors were used to generate the models for these quantities from the grid of ATLAS models without convective overshoot (Castelli et al. 1997) using software originally provided by A. McWilliam. Table 2.4 displays the parameters for the stars of the external source data set.

Table 2.3. LTG Stellar Model Parameters and Individual [Fe/H] and [Mn/Fe] Values

Association	Star	T_{eff} (K)	log g	v_t (km s ⁻¹)	[Fe/H] LIT ^a	[Fe/H]	[Mn/Fe]
NGC 5272 (M3)	B21	4725	1.65	1.20	-1.61	-1.48	-0.61
NGC 5272 (M3)	B23	4800	2.10	1.40	-1.70	-1.63	-0.61
NGC 5272 (M3)	B24	4450	1.00	1.90	-1.59	-1.52	-0.48
NGC 5272 (M3)	B33	4550	1.30	1.65	-1.55	-1.48	-0.55
NGC 5272 (M3)	B34	3850	0.00	2.00	-1.62	-1.55	-0.55
NGC 5272 (M3)	B11	4400	1.10	1.50	-1.56	-1.59	-0.41
NGC 5272 (M3)	B12	4400	1.10	1.80	-1.62	-1.74	-0.34
NGC 5272 (M3)	B13	3900	0.00	2.05	-1.54	-1.58	-0.41
NGC 5272 (M3)	B14	4175	0.70	1.70	-1.58	-1.60	-0.39
NGC 5272 (M3)	B15	4350	1.10	1.50	-1.67	-1.67	-0.43
NGC 5272 (M3)	B41	4075	0.40	1.70	-1.54	-1.57	-0.41
NGC 5272 (M3)	B42	4100	0.40	1.70	-1.56	-1.56	-0.43
NGC 5272 (M3)	B43	4750	1.40	1.60	-1.75	-1.71	-0.39
NGC 5272 (M3)	B44	5050	2.00	1.50	-1.71	-1.71	-0.41
NGC 5272 (M3)	B45	5100	2.40	1.00	-1.58	-1.73	-0.28
NGC 5272 (M3)	F24	4600	1.70	1.20	-1.54	-1.51	-0.41
NGC 5272 (M3)	I21	4175	0.70	1.70	-1.52	-1.57	-0.39
NGC 5272 (M3)	IV-101	4200	0.75	1.70	-1.50	-1.46	-0.48
NGC 5272 (M3)	IV-77	4300	0.85	1.80	-1.52	-1.60	-0.33
NGC 5272 (M3)	VZ1397	3925	0.10	2.00	-1.53	-1.57	-0.37
NGC 5904 (M5)	G2	3900	-0.10	1.75	-1.33	-1.38	-0.48

Table 2.3 (cont'd)

Association	Star	T_{eff} (K)	$\log g$	v_t (km s^{-1})	$[Fe/H]$ LIT ^a	$[Fe/H]$	$[Mn/Fe]$
NGC 5904 (M5)	I-14	4250	0.75	1.60	-1.34	-1.36	-0.38
NGC 5904 (M5)	I-2	4500	1.10	1.45	-1.31	-1.29	-0.38
NGC 5904 (M5)	I-20	4050	0.00	2.00	-1.44	-1.60	-0.18
NGC 5904 (M5)	I-50	4525	1.15	1.40	-1.33	-1.28	-0.48
NGC 5904 (M5)	I-55	4700	0.85	1.80	-1.47	-1.56	-0.38
NGC 5904 (M5)	I-58	4350	0.80	1.50	-1.27	-1.34	-0.35
NGC 5904 (M5)	I-61	4400	1.00	1.50	-1.32	-1.36	-0.35
NGC 5904 (M5)	I-68	4066	0.63	2.20	-1.44	-1.45	-0.58
NGC 5904 (M5)	I-71	4360	1.12	1.65	-1.32	-1.38	-0.37
NGC 5904 (M5)	II-50	4525	1.15	1.35	-1.24	-1.31	-0.38
NGC 5904 (M5)	II-59	4463	1.15	1.65	-1.33	-1.32	-0.56
NGC 5904 (M5)	II-74	4525	1.30	1.30	-1.17	-1.08	-0.58
NGC 5904 (M5)	II-85	4009	0.54	1.80	-1.30	-1.37	-0.31
NGC 5904 (M5)	III-122	4001	0.44	2.00	-1.26	-1.23	-0.54
NGC 5904 (M5)	III-18	4475	0.55	1.70	-1.43	-1.42	-0.45
NGC 5904 (M5)	III-3	4076	0.63	1.95	-1.31	-1.41	-0.41
NGC 5904 (M5)	III-36	4227	0.91	1.65	-1.28	-1.28	-0.47
NGC 5904 (M5)	III-52	4625	1.50	1.45	-1.38	-1.39	-0.36
NGC 5904 (M5)	III-53	4700	1.05	1.75	-1.52	-1.64	-0.33
NGC 5904 (M5)	III-59	4575	1.20	1.35	-1.30	-1.24	-0.45
NGC 5904 (M5)	III-78	4154	0.78	1.95	-1.32	-1.38	-0.45

Table 2.3 (cont'd)

Association	Star	T_{eff} (K)	$\log g$	v_t (km s ⁻¹)	$[Fe/H]$ LIT ^a	$[Fe/H]$	$[Mn/Fe]$
NGC 5904 (M5)	IV-19	4125	0.50	1.70	-1.39	-1.32	-0.43
NGC 5904 (M5)	IV-26	4650	1.05	1.40	-1.41	-1.43	-0.38
NGC 5904 (M5)	IV-30	4625	1.00	1.75	-1.47	-1.47	-0.43
NGC 5904 (M5)	IV-34	4275	0.65	1.55	-1.28	-1.33	-0.40
NGC 5904 (M5)	IV-36	4575	1.50	1.35	-1.27	-1.28	-0.38
NGC 5904 (M5)	IV-4	4625	1.55	1.20	-1.24	-1.40	-0.38
NGC 5904 (M5)	IV-47	4110	0.50	1.85	-1.34	-1.30	-0.53
NGC 5904 (M5)	IV-59	4229	0.79	2.10	-1.40	-1.44	-0.45
NGC 5904 (M5)	IV-81	3945	0.00	1.90	-1.35	-1.37	-0.38
NGC 6121 (M4)	1408	4525	1.30	1.70	-1.18	-1.23	-0.41
NGC 6121 (M4)	1411	3950	0.60	1.65	-1.21	-1.26	-0.35
NGC 6121 (M4)	1514	3875	0.35	1.95	-1.23	-1.34	-0.36
NGC 6121 (M4)	1701	4625	1.50	1.65	-1.20	-1.20	-0.44
NGC 6121 (M4)	2206	4325	1.35	1.55	-1.18	-1.21	-0.34
NGC 6121 (M4)	2208	4350	1.40	1.70	-1.12	-1.17	-0.38
NGC 6121 (M4)	2307	4075	0.85	1.45	-1.20	-1.28	-0.34
NGC 6121 (M4)	2406	4100	0.45	2.45	-1.22	-1.26	-0.40
NGC 6121 (M4)	3207	4700	1.65	1.70	-1.18	-1.21	-0.44
NGC 6121 (M4)	3209	3975	0.60	1.75	-1.22	-1.26	-0.37
NGC 6121 (M4)	3215	4775	1.40	1.85	-1.17	-1.24	-0.43
NGC 6121 (M4)	3413	4175	1.20	1.65	-1.18	-1.33	-0.27

Table 2.3 (cont'd)

Association	Star	T_{eff} (K)	$\log g$	v_t (km s^{-1})	$[Fe/H]$ LIT ^a	$[Fe/H]$	$[Mn/Fe]$
NGC 6121 (M4)	3612	4250	1.10	1.45	-1.20	-1.21	-0.41
NGC 6121 (M4)	3624	4225	1.10	1.45	-1.16	-1.24	-0.40
NGC 6121 (M4)	4201	4450	1.35	1.85	-1.19	-1.19	-0.44
NGC 6121 (M4)	4302	4775	1.45	1.80	-1.18	-1.22	-0.50
NGC 6121 (M4)	4511	4150	1.10	1.55	-1.16	-1.16	-0.43
NGC 6121 (M4)	4513	5250	1.00	1.65	-1.20	-1.43	-0.22
NGC 6121 (M4)	4611	3725	0.30	1.70	-1.16	-1.20	-0.52
NGC 6121 (M4)	4613	3750	0.20	1.65	-1.19	-1.26	-0.49
NGC 6205 (M13)	L-629	3950	0.20	2.00	-1.68	-1.72	-0.36
NGC 6205 (M13)	II-90	4000	0.30	2.00	-1.60	-1.65	-0.46
NGC 6205 (M13)	II-67	3950	0.20	2.10	-1.58	-1.65	-0.37
NGC 6205 (M13)	I-48	3920	0.30	2.00	-1.60	-1.66	-0.47
NGC 6205 (M13)	L-598	3900	0.00	2.10	-1.64	-1.67	-0.38
NGC 6205 (M13)	IV-22	4700	1.90	1.50	-1.56	-1.63	-0.37
NGC 6205 (M13)	II-9	4700	1.70	1.50	-1.59	-1.63	-0.42
NGC 6205 (M13)	II-28	4850	1.75	2.00	-1.68	-1.78	-0.33
NGC 6205 (M13)	IV-25	4000	0.15	2.25	-1.61	-1.64	-0.37
NGC 6205 (M13)	L-835	4090	0.55	1.90	-1.56	-1.63	-0.34
NGC 6205 (M13)	I-54	4975	1.70	1.75	-1.71	-1.77	-0.41
NGC 6205 (M13)	I-72	4850	1.90	1.45	-1.65	-1.75	-0.37
NGC 6205 (M13)	II-1	4850	2.10	1.25	-1.58	-1.62	-0.44

Table 2.3 (cont'd)

Association	Star	T_{eff} (K)	$\log g$	v_t (km s ⁻¹)	$[Fe/H]$ LIT ^a	$[Fe/H]$	$[Mn/Fe]$
NGC 6205 (M13)	I-12	4600	1.50	1.60	-1.58	-1.66	-0.37
NGC 6205 (M13)	IV-19	4650	1.50	1.60	-1.59	-1.64	-0.36
NGC 6205 (M13)	II-41	4750	2.00	1.75	-1.51	-1.60	-0.36
NGC 6205 (M13)	III-52	4335	1.00	2.00	-1.54	-1.72	-0.35
NGC 6254 (M10)	A-I-2	3975	0.00	2.10	-1.47	-1.64	-0.33
NGC 6254 (M10)	A-I-60	4400	1.10	1.60	-1.53	-1.48	-0.55
NGC 6254 (M10)	A-I-61	4550	1.00	2.00	-1.69	-1.74	-0.40
NGC 6254 (M10)	A-II-24	4050	0.10	2.00	-1.50	-1.55	-0.48
NGC 6254 (M10)	A-III-16	4150	0.90	2.00	-1.52	-1.62	-0.39
NGC 6254 (M10)	A-III-21	4060	0.50	2.10	-1.49	-1.64	-0.28
NGC 6254 (M10)	A-III-5	4400	1.20	1.75	-1.36	-1.48	-0.26
NGC 6254 (M10)	C	4200	0.75	2.00	-1.66	-1.80	-0.37
NGC 6254 (M10)	D	4200	1.05	2.00	-1.50	-1.59	-0.40
NGC 6254 (M10)	E	4350	0.80	2.00	-1.61	-1.83	-0.34
NGC 6254 (M10)	H-I-15	4225	0.75	1.75	-1.52	-1.59	-0.42
NGC 6254 (M10)	H-I-367	4135	0.60	1.70	-1.54	-1.68	-0.41
NGC 6341 (M92)	III-13	4180	0.10	2.15	-2.24	-2.39	-0.36
NGC 6341 (M92)	III-65	4260	0.30	1.80	-2.25	-2.46	-0.43
NGC 6341 (M92)	VII-122	4300	0.70	1.85	-2.32	-2.52	-0.39
NGC 6341 (M92)	VII-18	4220	0.20	2.00	-2.27	-2.43	-0.30
NGC 6838 (M71)	A4	4100	0.80	2.25	-0.78	-1.34	-0.07

Table 2.3 (cont'd)

Association	Star	T_{eff} (K)	$\log g$	v_t (km s^{-1})	$[Fe/H]$ LIT ^a	$[Fe/H]$	$[Mn/Fe]$
NGC 6838 (M71)	I	4300	1.00	2.00	-0.89	-1.26	-0.05
NGC 6838 (M71)	1-77	4100	0.95	2.00	-0.78	-1.22	0.03
NGC 6838 (M71)	1-45	4050	0.80	2.00	-0.76	-1.21	-0.20
NGC 6838 (M71)	1-53	4300	1.40	2.00	-0.79	-1.21	0.04
NGC 6838 (M71)	1-113	3950	0.70	2.00	-0.85	-1.12	-0.42
NGC 6838 (M71)	1-46	4000	0.80	2.15	-0.77	-1.10	-0.26
NGC 6838 (M71)	S	4300	1.25	2.00	-0.72	-1.00	-0.21
NGC 6838 (M71)	1-21	4350	1.45	2.00	-0.73	-0.91	-0.25
NGC 6838 (M71)	A9	4200	1.20	2.00	-0.85	-0.90	-0.24
NGC 7006	I-1	3900	0.10	2.25	-1.55	-1.72	-0.39
NGC 7006	II-103	4200	0.75	1.85	-1.55	-1.58	-0.33
NGC 7006	II-18	4300	0.90	1.85	-1.56	-1.46	-0.48
NGC 7006	II-46	4200	0.50	2.25	-1.60	-1.54	-0.43
NGC 7006	V19	4100	0.30	2.40	-1.62	-1.69	-0.39
NGC 7006	V54	4500	0.80	2.25	-1.65	-1.72	-0.54
NGC 7078 (M15)	K341	4275	0.45	2.00	-2.35	-2.46	-0.29
NGC 7078 (M15)	K387	4400	0.65	1.85	-2.42	-2.51	-0.38
NGC 7078 (M15)	K969	4625	1.30	2.60	-2.42	-2.56	-0.44
NGC 7078 (M15)	K431	4375	0.50	2.30	-2.43	-2.50	-0.39
NGC 7078 (M15)	K146	4450	0.80	1.90	-2.46	-2.58	-0.42
NGC 7078 (M15)	K386	4200	0.15	1.85	-2.43	-2.51	-0.45

Table 2.3 (cont'd)

Association	Star	T_{eff} (K)	$\log g$	v_t (km s^{-1})	$[Fe/H]$ LIT ^a	$[Fe/H]$	$[Mn/Fe]$
NGC 7078 (M15)	K583	4275	0.30	1.90	-2.40	-2.51	-0.46
NGC 7078 (M15)	K702	4325	0.25	1.90	-2.44	-2.45	-0.44
NGC 7078 (M15)	K462	4225	0.30	1.85	-2.45	-2.48	-0.36
NGC 7078 (M15)	K490	4350	0.60	1.65	-2.44	-2.59	-0.06
NGC 7078 (M15)	K634	4225	0.30	1.85	-2.38	-2.44	-0.31
Pal 5	E	4500	1.45	1.65	-1.39	-1.63	-0.22
Pal 5	F	4500	1.50	1.60	-1.33	-1.43	-0.38
Pal 5	G	4535	1.55	1.55	-1.31	-1.43	-0.28
Pal 5	H	4750	1.55	1.70	-1.32	-1.53	-0.28
FIELD (JF)	171	5275	4.1	1.05	-1.00	-0.91	-0.27
FIELD (JF)	2413	5050	2.2	1.60	-1.96	-2.01	-0.38
FIELD (JF)	3026	5950	3.9	1.40	-1.32	-1.32	-0.24
FIELD (JF)	3086	5700	4.1	1.00	-0.17	-0.06	-0.29
FIELD (JF)	5336	5250	4.4	0.90	-0.98	-0.83	-0.32
FIELD (JF)	5445	5150	2.8	1.50	-1.58	-1.61	-0.32
FIELD (JF)	5458	4450	1.4	1.55	-1.04	-0.87	-0.33
FIELD (JF)	6710	4625	1.2	1.95	-1.83	-1.90	-0.28
FIELD (JF)	7217	5550	4.2	0.70	-0.48	-0.41	-0.36
FIELD (JF)	10140	5425	4.1	0.85	-1.14	-0.97	-0.41
FIELD (JF)	10449	5650	4.4	1.00	-0.98	-0.90	-0.43
FIELD (JF)	11349	5375	4.3	0.80	-0.29	-0.15	-0.22

Table 2.3 (cont'd)

Association	Star	T_{eff} (K)	$\log g$	v_t (km s ⁻¹)	$[Fe/H]$ LIT ^a	$[Fe/H]$	$[Mn/Fe]$
FIELD (JF)	12306	5650	4.1	1.05	-0.63	-0.51	-0.35
FIELD (JF)	13366	5700	4.2	0.95	-0.77	-0.72	-0.33
FIELD (JF)	14086	5075	3.6	1.10	-0.71	-0.68	-0.32
FIELD (JF)	15394	5150	3.4	1.00	-0.30	-0.08	-0.29
FIELD (JF)	16214	4825	2.0	1.45	-1.74	-1.72	-0.39
FIELD (JF)	17085	6500	4.2	1.70	-0.22	-0.13	-0.20
FIELD (JF)	17147	5800	4.3	1.10	-0.91	-0.83	-0.34
FIELD (JF)	17666	5050	4.5	0.60	-1.10	-0.93	-0.47
FIELD (JF)	18235	4950	3.2	0.90	-0.72	-0.63	-0.45
FIELD (JF)	18915	4700	4.8	1.35	-1.85	-1.77	-0.33
FIELD (JF)	18995	5575	2.2	2.05	-1.26	-1.24	-0.37
FIELD (JF)	19007	5150	4.5	1.20	-0.62	-0.51	-0.03
FIELD (JF)	19378	4500	1.2	1.70	-1.73	-1.75	-0.34
FIELD (JF)	21000	6200	4.1	1.40	-0.16	-0.11	-0.22
FIELD (JF)	21586	4850	4.1	0.25	-0.91	-0.67	-0.35
FIELD (JF)	21609	5200	3.8	1.55	-1.76	-1.70	-0.36
FIELD (JF)	21648	4300	0.4	1.70	-1.88	-1.84	-0.40
FIELD (JF)	21767	5650	4.5	0.70	-0.44	-0.35	-0.31
FIELD (JF)	22246	5200	4.5	1.20	-0.38	-0.33	-0.13
FIELD (JF)	22632	5825	4.3	1.35	-1.59	-1.61	-0.40
FIELD (JF)	26688	6500	4.1	1.50	-0.60	-0.61	-0.14

Table 2.3 (cont'd)

Association	Star	T_{eff} (K)	$\log g$	v_t (km s ⁻¹)	$[Fe/H]$ LIT ^a	$[Fe/H]$	$[Mn/Fe]$
FIELD (JF)	27654	4550	2.1	1.50	-0.94	-0.87	-0.32
FIELD (JF)	28188	6175	4.6	1.25	-0.62	-0.63	-0.17
FIELD (JF)	30668	5150	3.1	1.05	-1.50	-1.54	-0.52
FIELD (JF)	30990	5825	4.0	1.30	-0.89	-0.93	-0.29
FIELD (JF)	31188	5750	4.1	1.65	-0.80	-0.63	-0.24
FIELD (JF)	31639	5300	4.3	0.60	-0.62	-0.47	-0.30
FIELD (JF)	32308	5175	4.1	1.00	-0.64	-0.42	-0.27
FIELD (JF)	33582	5725	4.3	1.25	-0.74	-0.80	-0.12
FIELD (JF)	34146	6300	4.2	1.95	-0.40	-0.43	-0.16
FIELD (JF)	34548	6250	4.5	1.40	-0.46	-0.45	-0.12
FIELD (JF)	36491	5800	4.4	1.10	-0.93	-0.87	-0.31
FIELD (JF)	36849	5850	4.1	1.10	-0.88	-0.88	-0.27
FIELD (JF)	38541	5300	4.7	0.85	-1.79	-1.74	-0.50
FIELD (JF)	38621	4700	1.7	2.25	-1.81	-1.88	-0.26
FIELD (JF)	38625	5200	4.4	0.30	-0.86	-0.73	-0.34
FIELD (JF)	40068	5225	3.0	1.35	-2.05	-1.98	-0.40
FIELD (JF)	44075	5900	4.2	1.25	-0.91	-0.90	-0.29
FIELD (JF)	44116	6275	4.1	1.45	-0.58	-0.53	-0.23
FIELD (JF)	44716	5000	2.1	1.70	-1.08	-1.10	-0.32
FIELD (JF)	44919	6350	3.8	1.80	-0.65	-0.68	-0.08
FIELD (JF)	47139	4600	1.3	1.80	-1.46	-1.48	-0.38

Table 2.3 (cont'd)

Association	Star	T_{eff} (K)	$\log g$	v_t (km s ⁻¹)	$[Fe/H]$ LIT ^a	$[Fe/H]$	$[Mn/Fe]$
FIELD (JF)	47640	6600	4.4	1.50	-0.08	-0.05	-0.24
FIELD (JF)	48146	6200	4.6	1.05	-0.05	-0.02	-0.19
FIELD (JF)	49371	4950	2.3	1.75	-1.95	-1.89	-0.38
FIELD (JF)	50139	5600	4.3	0.35	-0.68	-0.56	-0.31
FIELD (JF)	54858	5250	2.0	2.15	-1.17	-1.20	-0.34
FIELD (JF)	57265	5875	4.0	1.50	-1.10	-1.05	-0.36
FIELD (JF)	57850	4375	0.8	2.75	-1.78	-1.78	-0.29
FIELD (JF)	58229	5875	4.1	1.25	-0.94	-0.92	-0.43
FIELD (JF)	58357	5050	3.4	1.20	-0.65	-0.72	-0.25
FIELD (JF)	59239	5125	2.1	1.55	-1.49	-1.50	-0.39
FIELD (JF)	59330	5750	4.1	1.25	-0.75	-0.73	-0.26
FIELD (JF)	59750	6200	4.4	1.10	-0.78	-0.64	-0.45
FIELD (JF)	60551	5725	4.4	1.05	-0.86	-0.87	-0.24
FIELD (JF)	62747	4285	2.2	1.45	-1.54	-1.51	-0.45
FIELD (JF)	62882	5600	3.7	0.04	-1.26	-1.12	-0.55
FIELD (JF)	63970	6075	4.4	1.00	-0.09	0.03	-0.26
FIELD (JF)	64115	4650	2.4	1.10	-0.74	-0.62	-0.48
FIELD (JF)	64426	5800	4.1	1.25	-0.82	-0.78	-0.30
FIELD (JF)	65268	6250	4.1	1.50	-0.67	-0.60	-0.23
FIELD (JF)	66246	4400	1.0	2.55	-1.91	-2.00	-0.19
FIELD (JF)	66509	5350	4.2	0.60	-0.68	-0.53	-0.43

Table 2.3 (cont'd)

Association	Star	T_{eff} (K)	$\log g$	v_t (km s ⁻¹)	$[Fe/H]$ LIT ^a	$[Fe/H]$	$[Mn/Fe]$
FIELD (JF)	66665	5500	3.8	1.05	-0.97	-0.78	-0.48
FIELD (JF)	66815	5875	4.5	0.95	-0.64	-0.63	-0.26
FIELD (JF)	68796	5725	4.5	0.90	-0.52	-0.43	-0.24
FIELD (JF)	68807	4575	1.1	1.90	-1.83	-1.82	-0.33
FIELD (JF)	70681	5450	4.5	0.80	-1.25	-1.23	-0.38
FIELD (JF)	71886	6400	4.1	1.50	-0.40	-0.32	-0.24
FIELD (JF)	71887	6100	4.3	1.20	-0.49	-0.45	-0.26
FIELD (JF)	71939	6300	4.4	1.50	-0.37	-0.36	-0.18
FIELD (JF)	73385	5575	3.6	1.35	-1.59	-1.59	-0.31
FIELD (JF)	73960	4500	1.4	2.10	-1.37	-1.33	-0.38
FIELD (JF)	74033	5675	4.1	1.05	-0.78	-0.80	-0.38
FIELD (JF)	74067	5575	4.3	1.10	-0.90	-0.88	-0.28
FIELD (JF)	74079	5825	4.0	1.30	-0.83	-0.75	-0.31
FIELD (JF)	74234	4750	4.5	0.70	-1.51	-1.33	-0.51
FIELD (JF)	74235	4850	4.5	0.70	-1.57	-1.42	-0.47
FIELD (JF)	80837	5800	4.1	1.15	-0.83	-0.74	-0.37
FIELD (JF)	81170	5175	4.7	0.30	-1.26	-1.23	-0.38
FIELD (JF)	81461	5600	4.1	1.20	-0.65	-0.46	-0.31
FIELD (JF)	85007	5900	4.2	1.20	-0.50	-0.38	-0.34
FIELD (JF)	85378	5625	4.0	1.10	-0.64	-0.53	-0.35
FIELD (JF)	85757	5450	3.8	1.05	-0.76	-0.65	-0.35

Table 2.3 (cont'd)

Association	Star	T_{eff} (K)	$\log g$	v_t (km s ⁻¹)	$[Fe/H]$ LIT ^a	$[Fe/H]$	$[Mn/Fe]$
FIELD (JF)	86013	5750	4.4	1.15	-0.82	-0.84	-0.25
FIELD (JF)	86431	5675	4.1	1.15	-0.64	-0.54	-0.37
FIELD (JF)	88010	5200	4.0	0.70	-1.49	-1.41	-0.38
FIELD (JF)	88039	5700	4.0	1.30	-0.96	-0.88	-0.33
FIELD (JF)	91058	6025	4.1	1.40	-0.54	-0.49	-0.22
FIELD (JF)	92167	4575	2.4	1.40	-1.47	-1.80	-0.51
FIELD (JF)	92532	5825	4.3	1.00	-0.56	-0.44	-0.25
FIELD (JF)	92781	5650	4.2	0.95	-0.75	-0.57	-0.48
FIELD (JF)	94449	5625	3.7	1.15	-1.26	-1.22	-0.34
FIELD (JF)	96185	5700	4.1	1.00	-0.58	-0.53	-0.35
FIELD (JF)	97023	5800	3.8	1.30	-0.48	-0.35	-0.27
FIELD (JF)	97468	4450	1.1	1.90	-1.71	-1.73	-0.32
FIELD (JF)	98020	5325	4.6	1.10	-1.67	-1.58	-0.49
FIELD (JF)	98532	5550	3.6	1.30	-1.23	-1.18	-0.33
FIELD (JF)	99423	5650	3.8	1.30	-1.50	-1.43	-0.43
FIELD (JF)	99938	5650	4.0	1.20	-0.74	-0.65	-0.31
FIELD (JF)	100568	5650	4.4	1.10	-1.17	-1.12	-0.36
FIELD (JF)	100792	5875	4.2	1.40	-1.23	-1.19	-0.34
FIELD (JF)	101346	6000	3.9	1.40	-0.65	-0.68	-0.14
FIELD (JF)	101382	5125	4.0	0.40	-0.66	-0.38	-0.39
FIELD (JF)	103269	5300	4.6	0.85	-1.81	-1.80	-0.48

Table 2.3 (cont'd)

Association	Star	T_{eff} (K)	$\log g$	v_t (km s ⁻¹)	$[Fe/H]$ LIT ^a	$[Fe/H]$	$[Mn/Fe]$
FIELD (JF)	104659	5825	4.3	1.00	-1.12	-1.03	-0.38
FIELD (JF)	104660	5500	3.9	1.15	-0.96	-0.78	-0.41
FIELD (JF)	105888	5700	4.3	1.00	-0.75	-0.63	-0.34
FIELD (JF)	107975	6275	3.9	1.50	-0.64	-0.54	-0.33
FIELD (JF)	109067	5300	4.3	0.85	-0.97	-0.88	-0.37
FIELD (JF)	109390	4800	2.2	1.50	-1.34	-1.33	-0.43
FIELD (JF)	112796	4525	1.0	2.85	-2.25	-2.26	-0.16
FIELD (JF)	114962	5825	4.3	1.40	-1.54	-1.33	-0.44
FIELD (JF)	115610	4800	4.1	1.20	-0.63	-0.35	-0.13
FIELD (JF)	115949	4500	0.9	2.75	-2.19	-2.17	-0.28
FIELD (JF)	116082	6275	3.7	1.60	-0.82	-0.80	-0.22
FIELD (JF)	117029	5425	3.8	1.05	-0.81	-0.75	-0.30
FIELD (JF)	117041	5300	4.2	0.90	-0.88	-0.81	-0.25
FIELD (JS)	B-010306	5550	4.19	1.50	-1.13	-1.10	-0.30
FIELD (JS)	B-012582	5148	2.86	1.20	-2.21	-2.26	-0.41
FIELD (JS)	B+191185	5500	4.19	1.10	-1.09	-1.09	-0.31
FIELD (JS)	B+521601	4911	2.10	2.05	-1.40	-1.49	-0.33
FIELD (JS)	G005-001	5500	4.32	0.80	-1.24	-1.18	-0.31
FIELD (JS)	G009-036	5625	4.57	0.65	-1.17	-1.17	-0.44
FIELD (JS)	G017-025	4966	4.26	0.80	-1.54	-1.37	-0.42
FIELD (JS)	G023-014	5025	3.00	1.30	-1.64	-1.57	-0.44

Table 2.3 (cont'd)

Association	Star	T_{eff} (K)	$\log g$	v_t (km s ⁻¹)	$[Fe/H]$ LIT ^a	$[Fe/H]$	$[Mn/Fe]$
FIELD (JS)	G028-043	5061	4.50	0.80	-1.64	-1.58	-0.42
FIELD (JS)	G029-025	5225	4.28	0.80	-1.09	-0.91	-0.44
FIELD (JS)	G040-008	5200	4.08	0.50	-0.97	-0.80	-0.37
FIELD (JS)	G058-025	6001	4.21	1.05	-1.40	-1.49	-0.36
FIELD (JS)	G059-001	5922	3.98	0.40	-0.95	-0.76	-0.38
FIELD (JS)	G063-046	5705	4.25	1.30	-0.90	-0.85	-0.28
FIELD (JS)	G068-003	4975	3.50	0.95	-0.76	-0.65	-0.28
FIELD (JS)	G074-005	5668	4.24	1.50	-1.05	-1.03	-0.28
FIELD (JS)	G090-025	5303	4.46	1.20	-1.78	-1.83	-0.53
FIELD (JS)	G095-57A	4965	4.40	0.90	-1.22	-1.08	-0.37
FIELD (JS)	G095-57B	4800	4.57	0.60	-1.06	-1.03	-0.30
FIELD (JS)	G102-020	5254	4.44	0.90	-1.25	-1.23	-0.32
FIELD (JS)	G102-027	5600	3.75	1.05	-0.59	-0.50	-0.35
FIELD (JS)	G113-022	5525	4.25	1.10	-1.18	-1.19	-0.40
FIELD (JS)	G122-051	4864	4.51	1.40	-1.43	-1.42	-0.43
FIELD (JS)	G123-009	5487	4.75	1.50	-1.25	-1.30	-0.29
FIELD (JS)	G126-036	5487	4.50	0.60	-1.06	-0.96	-0.36
FIELD (JS)	G126-062	5941	3.98	2.00	-1.59	-1.75	-0.28
FIELD (JS)	G140-046	4980	4.42	0.70	-1.30	-1.18	-0.43
FIELD (JS)	G153-021	5700	4.36	1.40	-0.70	-0.71	-0.18
FIELD (JS)	G176-053	5593	4.50	1.20	-1.34	-1.41	-0.37

Table 2.3 (cont'd)

Association	Star	T_{eff} (K)	$\log g$	v_t (km s ⁻¹)	[Fe/H] LIT ^a	[Fe/H]	[Mn/Fe]
FIELD (JS)	G179-022	5082	3.20	1.20	-1.35	-1.28	-0.40
FIELD (JS)	G180-024	6059	4.09	0.50	-1.34	-1.38	-0.28
FIELD (JS)	G188-022	5827	4.27	1.20	-1.52	-1.48	-0.36
FIELD (JS)	G191-055	5770	4.50	1.00	-1.63	-1.77	-0.19
FIELD (JS)	G192-043	6085	4.50	1.50	-1.50	-1.56	-0.33
FIELD (JS)	G221-007	5016	3.37	0.90	-0.98	-0.86	-0.33
FIELD (JS)	2665	4990	2.34	2.00	-1.99	-2.17	-0.38
FIELD (JS)	3008	4250	0.25	2.60	-2.08	-2.14	-0.33
FIELD (JS)	6755	5105	2.93	2.50	-1.68	-1.78	-0.29
FIELD (JS)	8724	4535	1.40	1.40	-1.91	-1.79	-0.51
FIELD (JS)	21581	4870	2.27	1.40	-1.71	-1.75	-0.43
FIELD (JS)	23798	4450	1.06	2.50	-2.26	-2.32	-0.29
FIELD (JS)	25329	4842	4.66	0.60	-1.67	-1.67	-0.40
FIELD (JS)	25532	5396	2.00	1.20	-1.34	-1.17	-0.50
FIELD (JS)	26297	4322	1.11	1.80	-1.98	-1.92	-0.41
FIELD (JS)	29574	4250	0.80	2.20	-2.00	-2.00	-0.43
FIELD (JS)	37828	4350	1.50	1.85	-1.62	-1.59	-0.40
FIELD (JS)	44007	4851	2.00	2.00	-1.72	-1.74	-0.39
FIELD (JS)	63791	4675	2.00	2.00	-1.90	-1.86	-0.39
FIELD (JS)	74462	4700	2.00	1.90	-1.52	-1.55	-0.29
FIELD (JS)	82590	6005	2.75	3.00	-1.50	-1.57	-0.30

Table 2.3 (cont'd)

Association	Star	T_{eff} (K)	$\log g$	v_t (km s ⁻¹)	$[Fe/H]$ LIT ^a	$[Fe/H]$	$[Mn/Fe]$
FIELD (JS)	85773	4268	0.50	2.00	-2.62	-2.50	-0.29
FIELD (JS)	101063	5150	3.25	1.70	-1.33	-1.38	-0.31
FIELD (JS)	103036	4200	0.25	3.00	-2.04	-1.93	-0.48
FIELD (JS)	103545	4666	1.64	2.00	-2.45	-2.41	-0.38
FIELD (JS)	105546	5190	2.49	1.60	-1.48	-1.52	-0.25
FIELD (JS)	105755	5701	3.82	1.20	-0.83	-0.76	-0.30
FIELD (JS)	106516	6166	4.21	1.10	-0.81	-0.76	-0.38
FIELD (JS)	108317	5234	2.68	2.00	-2.18	-2.25	-0.17
FIELD (JS)	110184	4250	0.50	2.50	-2.72	-2.66	-0.32
FIELD (JS)	121135	4934	1.91	1.60	-1.54	-1.49	-0.50
FIELD (JS)	122563	4572	1.36	2.90	-2.72	-2.68	-0.25
FIELD (JS)	122956	4508	1.55	1.60	-1.95	-1.85	-0.44
FIELD (JS)	124358	4688	1.57	2.10	-1.91	-1.88	-0.40
FIELD (JS)	132475	5425	3.56	2.30	-1.86	-1.80	-0.37
FIELD (JS)	135148	4183	0.25	2.90	-2.17	-2.17	-0.25
FIELD (JS)	141531	4356	1.14	2.20	-1.79	-1.84	-0.33
FIELD (JS)	165195	4237	0.78	2.30	-2.60	-2.56	-0.43
FIELD (JS)	166161	5350	2.56	2.25	-1.23	-1.36	-0.33
FIELD (JS)	171496	4952	2.37	1.40	-0.67	-0.57	-0.33
FIELD (JS)	184266	6000	2.74	3.00	-1.43	-1.52	-0.30
FIELD (JS)	186478	4598	1.43	2.00	-2.56	-2.64	-0.48

Table 2.3 (cont'd)

Association	Star	T_{eff} (K)	$\log g$	v_t (km s ⁻¹)	$[Fe/H]$ LIT ^a	$[Fe/H]$	$[Mn/Fe]$
FIELD (JS)	187111	4271	1.05	1.90	-1.97	-1.90	-0.40
FIELD (JS)	188510	5564	4.51	1.00	-1.32	-1.50	-0.43
FIELD (JS)	193901	5750	4.46	1.50	-1.08	-1.13	-0.36
FIELD (JS)	194598	6044	4.19	1.00	-1.08	-1.12	-0.37
FIELD (JS)	201891	5909	4.19	1.00	-1.09	-1.06	-0.37
FIELD (JS)	204543	4672	1.49	2.00	-1.87	-1.95	-0.40
FIELD (JS)	206739	4647	1.78	1.90	-1.72	-1.77	-0.30
FIELD (JS)	210295	4750	2.50	1.55	-1.46	-1.48	-0.41
FIELD (JS)	214362	5727	2.62	2.00	-1.87	-1.93	-0.50
FIELD (JS)	218857	5103	2.44	1.90	-1.90	-2.08	-0.28
FIELD (JS)	221170	4410	1.09	1.70	-2.35	-2.30	-0.38
FIELD (JS)	232078	3875	0.50	2.10	-1.69	-1.74	-0.50
FIELD (JS)	233666	5157	2.00	1.70	-1.79	-1.86	-0.22

^aAs discussed in text, literature values of $[Fe/H]$ are provided.

Note. — Field stars from the Fulbright (2000) survey (labeled as JF) have Hipparcos identifications. Similarly, target stars of the Simmerer et al. (2004) survey (designated as JS) have Henry Draper identifications unless otherwise indicated.

Table 2.4. External Data Source Stellar Model Parameters and Individual [Fe/H] and [Mn/Fe] Values

Association	Star	T_{eff} (K)	log g	v_t (km s ⁻¹)	[Fe/H] LIT	[Fe/H] ^a	[Mn/Fe]
Cr 261	1045	4400	1.50	1.20	-0.16	-0.14	-0.41
Cr 261	1080	4490	2.20	1.20	-0.11	-0.25	-0.45
Cr 261	1871	4000	0.70	1.50	-0.31	-0.59	-0.22
Cr 261	2105	4300	1.50	1.50	-0.32	-0.47	-0.21
NGC 288	20	4050	0.60	1.75	-1.44	-1.62	-0.31
NGC 288	231	4300	1.10	1.50	-1.41	-1.50	-0.32
NGC 288	245	4250	0.80	1.40	-1.41	-1.47	-0.30
NGC 288	274	4025	0.70	1.90	-1.37	-1.48	-0.33
NGC 288	281	4125	0.60	1.71	-1.42	-1.65	-0.29
NGC 288	287	4350	1.20	1.40	-1.45	-1.34	-0.44
NGC 288	297	4330	1.20	1.70	-1.41	-1.62	-0.23
NGC 288	307	4350	1.20	1.35	-1.40	-1.63	-0.24
NGC 288	338	4325	1.30	1.60	-1.37	-1.55	-0.28
NGC 288	344	4180	0.80	1.60	-1.36	-1.45	-0.32
NGC 288	351	4330	1.20	1.55	-1.30	-1.53	-0.36
NGC 288	403	3950	0.20	1.90	-1.43	-1.59	-0.32
NGC 288	531	3780	0.10	1.60	-1.31	-1.70	-0.42
NGC 362	1137	4000	0.70	2.00	-1.37	-1.51	-0.31
NGC 362	1159	4125	0.80	1.90	-1.27	-1.37	-0.34
NGC 362	1334	3975	0.40	1.95	-1.30	-1.37	-0.42
NGC 362	1401	3875	0.00	1.90	-1.32	-1.39	-0.34

Table 2.4 (cont'd)

Association	Star	T_{eff} (K)	$\log g$	v_t (km s ⁻¹)	[Fe/H] LIT ^a	[Fe/H]	[Mn/Fe]
NGC 362	1423	3950	0.10	2.35	-1.37	-1.42	-0.41
NGC 362	1441	3975	0.20	1.90	-1.31	-1.44	-0.29
NGC 362	2115	3900	0.00	2.30	-1.38	-1.49	-0.32
NGC 362	2127	4110	0.60	2.25	-1.30	-1.52	-0.39
NGC 362	2423	4000	0.40	1.85	-1.32	-1.42	-0.41
NGC 362	77	4075	0.20	2.50	-1.34	-1.41	-0.34
NGC 362	MB2	4100	0.60	2.25	-1.30	-1.58	-0.20
NGC 362	V2	3950	0.10	2.70	-1.30	-1.58	-0.48
NGC 3201	5	4750	1.80	1.70	-1.38	-1.53	-0.42
NGC 3201	8	4410	1.50	1.80	-1.17	-1.56	-0.28
NGC 3201	9	4600	1.90	1.70	-1.18	-1.45	-0.34
NGC 3201	42	4500	1.50	2.00	-1.32	-1.65	-0.29
NGC 3201	112	4350	1.30	1.60	-1.38	-1.64	-0.18
NGC 3201	121	4000	0.00	2.00	-1.40	-1.56	-0.42
NGC 3201	168	4100	0.20	1.80	-1.42	-1.61	-0.30
NGC 3201	238	4250	0.90	1.80	-1.42	-1.53	-0.44
NGC 3201	293	4250	1.20	1.80	-1.39	-1.56	-0.38
NGC 3201	301	4250	1.00	2.20	-1.49	-1.65	-0.33
NGC 3201	312	4250	0.70	1.80	-1.47	-1.49	-0.49
NGC 3201	318	4350	0.80	1.90	-1.52	-1.59	-0.39
NGC 3201	357	4150	0.70	2.00	-1.55	-1.78	-0.21

Table 2.4 (cont'd)

Association	Star	T_{eff} (K)	$\log g$	v_t (km s ⁻¹)	$[Fe/H]$ LIT ^a	$[Fe/H]$	$[Mn/Fe]$
NGC 3201	419	4500	1.20	1.70	-1.28	-1.40	-0.58
NGC 6287	1491	4375	1.00	1.75	-2.15	-2.28	-0.30
NGC 6287	1387	4250	0.80	1.90	-2.10	-2.33	-0.26
NGC 6293	2673	4250	0.50	1.90	-2.16	-2.24	-0.35
NGC 6293	3857	4450	0.70	1.75	-2.18	-2.40	-0.39
NGC 6528	I-42	4200	1.60	1.20	-0.14	-0.34	-0.23
NGC 6528	I-36	4300	1.50	1.50	-0.13	-0.37	-0.21
NGC 6528	I-18	4800	2.00	1.50	-0.05	-0.03	-0.33
NGC 6541	I-44	4250	0.70	1.85	-1.85	-1.95	-0.28
NGC 6541	II-113	4200	0.50	1.80	-1.86	-1.91	-0.36
NGC 6705 (M11)	660	4500	1.50	2.00	0.05	0.03	-0.43
NGC 6705 (M11)	669	4500	1.40	2.00	0.09	0.18	-0.32
NGC 6705 (M11)	686	4600	2.00	2.00	0.13	0.13	-0.45
NGC 6705 (M11)	779	4250	1.60	2.50	-0.01	-0.07	-0.49
NGC 6705 (M11)	916	4500	1.30	2.00	0.01	-0.04	-0.34
NGC 6705 (M11)	926	4500	1.50	2.00	-0.21	-0.59	-0.38
NGC 6705 (M11)	1184	4600	2.20	2.00	0.24	0.24	-0.30
NGC 6705 (M11)	1223	4750	2.50	2.00	0.19	-0.06	-0.39
NGC 6705 (M11)	1256	4600	2.50	2.00	0.31	0.28	-0.17
NGC 6705 (M11)	1423	4750	2.90	2.50	0.21	0.04	-0.05
NGC 6752	1	4749	1.95	1.41	-1.58	-1.69	-0.43

Table 2.4 (cont'd)

Association	Star	T_{eff} (K)	$\log g$	v_t (km s^{-1})	$[Fe/H]$ LIT	$[Fe/H]$ a	$[Mn/Fe]$
NGC 6752	2	4779	1.98	1.39	-1.59	-1.69	-0.48
NGC 6752	3	4796	2.03	1.42	-1.64	-1.74	-0.39
NGC 6752	4	4806	2.04	1.40	-1.61	-1.66	-0.46
NGC 6752	6	4804	2.06	1.40	-1.61	-1.87	-0.38
NGC 6752	7	4829	2.10	1.33	-1.84	-1.74	-0.53
NGC 6752	8	4910	2.15	1.33	-1.62	-1.60	-0.43
NGC 6752	9	4824	2.11	1.38	-1.63	-1.72	-0.41
NGC 6752	10	4836	2.13	1.37	-1.60	-1.63	-0.52
NGC 6752	11	4829	2.13	1.32	-1.64	-1.65	-0.47
NGC 6752	12	4841	2.15	1.34	-1.62	-1.72	-0.40
NGC 6752	15	4850	2.19	1.35	-1.61	-1.75	-0.45
NGC 6752	16	4906	2.24	1.32	-1.60	-1.73	-0.44
NGC 6752	19	4928	2.32	1.29	-1.61	-1.75	-0.49
NGC 6752	20	4929	2.33	1.32	-1.59	-1.69	-0.48
Pal 12	S1	3900	0.63	1.80	-0.76	-0.81	-0.31
Pal 12	1118	4000	0.84	1.80	-0.80	-0.82	-0.35
Pal 12	1128	4260	1.30	1.70	-0.82	-0.84	-0.40
Pal 12	1305	4465	1.62	1.70	-0.80	-0.84	-0.38

^aAs discussed in text, literature values of $[Fe/H]$ are provided.

In order to refine the line list, a portion of the solar spectrum (6000-6030 Å) was synthesized. The observed center-of-disk photospheric spectrum is that of Delbouille et al. (1990)². A Holweger-Müller model was selected with a microturbulent velocity of $v_t = 0.80 \text{ km s}^{-1}$, a value in accord with other solar abundance surveys (Holweger & Müller 1974; Grevesse & Sauval 1999). The standard LTG value of $\log \epsilon(\text{Fe})_{sun} = 7.52$ was used as set by Sneden et al. (1991b). The initial basis for this value originates from the work of Anders & Grevesse (1989). Further confirmation of this value was done by Anstee et al. (1997), who used neutral iron lines to derive an iron abundance for the Sun of 7.51 ± 0.01 . Several other studies arrive at approx-

²We employed the electronic version available on the website of the Base de donnes Solaire Sol: <http://bass2000.obspm.fr/home.php>

imately the same value (to within 0.1 dex) for the solar photospheric abundance of iron (e.g. Raassen & Uylings 1998; Asplund et al. 2000). The $\log\epsilon(\text{Mn})_{sun} = 5.39$ is also adopted as recommended by Anders & Grevesse (1989). Note, however, that there is a significant discrepancy between the solar photospheric and meteoritic CI chondrite [$\log\epsilon(\text{Mn})_{meteor} = 5.50$; Lodders 2003] values for Mn.

Spectrum synthesis was employed to determine the abundances as accurate determinations from transitions with multiple HFS components necessitate this technique. Abundance derivations that rely solely on the measurement of equivalent width values do not properly account for lines containing HFS without the introduction of an artifact (i.e., an arbitrary increase in microturbulent velocity; Cohen 1978). To generate synthetic spectra and to calculate abundances, the current version of the LTE line analysis code MOOG (Snedden 1973) was used. The raw relative flux values generated by this code were convolved with Gaussian broadening functions to reproduce the combined effects of astrophysical (i.e. macroturbulence) and instrumental (i.e. spectrograph slit) origin. Figure 2.2 shows a sample spectrum synthesis. In cases in which the spectra were not available, literature values of the equivalent width measurements were employed. In those instances, the synthetic spectrum fluxes were computed and then were summed to force-fit the observed equivalent width values. This technique was verified in some spectra for which synthetic fits were also made to observed spectra.

2.3.2 Line Parameters

Two Fe I features (6024 and 6027 Å) are available for abundance determinations in the specified wavelength range. A reliable Fe abundance may be obtained from these neutral lines as their excitation potential is large ($\chi > 4.0$ eV); consequently, they are

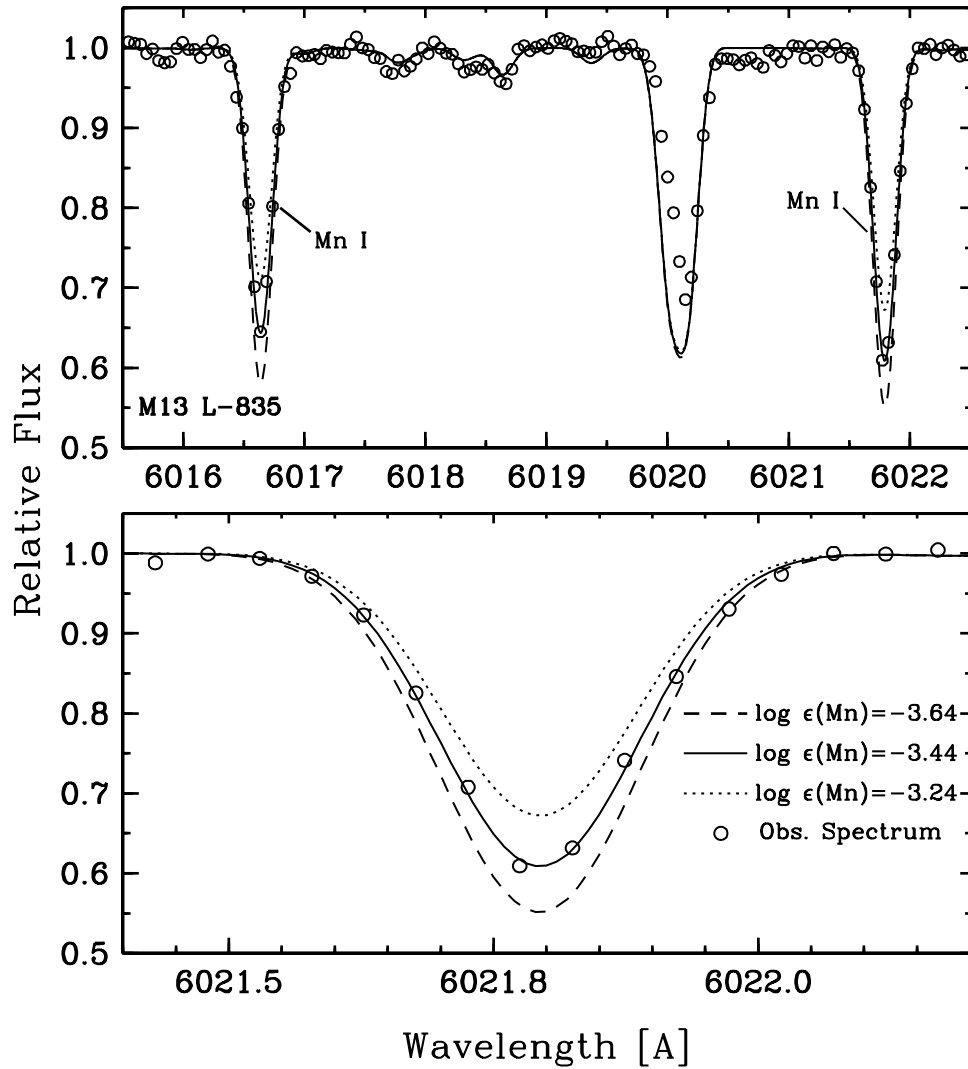


Figure 2.2 Comparison of the synthetic and observed spectrum for one M13 star. The top panel displays the observed and synthetic spectra for a wavelength range that encompasses the 6016 and 6021 Å Mn lines. The bottom panel focuses on the 6021 Å Mn feature and highlights the effects of incremental changes in abundance. Changes as small as 0.2 dex cause distinct variation in the synthesized spectrum.

not as susceptible to temperature effects and departures from LTE (Grevesse et al. 1996). Multiple literature sources give a transition probability for the 6027 Å feature. The emission measurement technique of O’Brian et al. (1991) yielded a gf-value for the 6027 Å line that is in good agreement with that found by the absorption line technique of Blackwell et al. (1982) . We adopted the O’Brian et al. log (gf) value for this line.

Unfortunately, neither O’Brian et al. (1991) nor Blackwell et al. (1982) give a transition probability for the 6024 Å feature. Literature sources for this line include the early work of Wolnik et al. (1970), log (gf)= -0.06 ± 0.00 ; the solar line inversion value of Thévenin (1990), log (gf)= -0.02 ± 0.02 ; and the semi-empirical derivation of Kurucz (1993), log (gf)= -0.120 . Taking into consideration the lack of modern laboratory atomic physics input into these numbers, we opted to perform an empirical derivation of the 6024 Å gf-value. An initial line list (in the specified 30 Å wavelength range) was assembled from Kurucz (1993) data. A synthetic spectrum was generated from this list and compared to the observed solar spectrum. Modification of the line list (i.e. revision of gf-values and deletion of non-essential features) occurred until the difference between the observed spectrum and the synthetic spectrum was minimized. With the refined line list in place, the iterative determination of the 6024 Å gf-value proceeded. The abundances of Mn and Fe were set to their corresponding solar values and the smoothing and continuum were fixed. Then the transition probability and the van der Waals damping parameter (C6) of the 6024 Å line were allowed to vary until a good fit was achieved. A final value of $\log(\text{gf})_{6024} = 0.04$ was obtained, with associated enhancement of the C6 damping parameter of $E\gamma = 2.2$. The result for the damping parameter enhancement is in agreement with the finding of Anstee et al. (1997 and references therein) that lines with an

Table 2.5. Line Parameters

Element	λ [Å]	χ [eV]	$\log(gf)$	E_γ
Fe I	6024.06	4.545	0.040	2.2
Fe I	6027.05	4.073	-1.089	2.0
Mn I	6013.51	3.070	-0.251	1.5
Mn I	6016.64	3.071	-0.216	1.5
Mn I	6021.82	3.073	0.034	1.5

excitation potential greater than 3.0 eV generally have an $E_\gamma > 2.1$.

With a nuclear spin of $I = 5/2$ and a magnetic dipole moment of $\mu_I = 3.4687 \mu_N$ (Lederer & Shirley 1978), Mn has a sizable HFS. The effect of HFS is to desaturate and broaden the lines of Mn. The strongest transitions of Mn are particularly susceptible. To ensure the accurate computation of Mn abundance, HFS was taken into account. Oscillator strengths for the 6013 and 6021 Å Mn lines were taken from Booth et al. (1983, 1984). Additional data were acquired from the Kurucz (1993) line list. Neither Booth et al. (1983) nor the NIST database³ (Martin et al. 1999) give a transition probability for the 6016 Å line. As before, the gf value for the 6016 Å Mn line was determined iteratively via a fit to the observed solar spectrum. Notably, the 6016 line possesses a significant Fe contaminant, whereas the 6013 and 6021 Å features do not contain any prominent blends. So, little weight is accorded to the abundance derived from the 6016 Å feature due to line contamination and slight uncertainty in oscillator strength value (it is used for a consistency check only). Final transition probabilities for all lines are reported in Table 2.5.

³The associated NIST website is: <http://physics.nist.gov/PhysRefData/ASD/index.html>.

2.4 Results

The essential finding is that in the metallicity range $-0.7 > [\text{Fe}/\text{H}] > -2.7$ the Mn abundances in globular cluster stars are equivalent to those of halo field stars. Figure 2.3 displays the $[\text{Mn}/\text{Fe}]$ ratio as a function of $[\text{Fe}/\text{H}]$ for all data. The mean abundance in the specified metallicity range is $\langle [\text{Mn}/\text{Fe}] \rangle = -0.37 \pm 0.01$ ($\sigma = 0.10$) for globular cluster stars and $\langle [\text{Mn}/\text{Fe}] \rangle = -0.36 \pm 0.01$ ($\sigma = 0.08$) for halo field stars. Figure 2.4 presents the correlation of S/N with $[\text{Mn}/\text{Fe}]$ for the LTG data set. As shown in the bottom panel, very high S/N data ($\text{S/N} > 175$) give an extremely consistent $[\text{Mn}/\text{Fe}]$ value. In Figure 2.5 the scatter in $[\text{Mn}/\text{Fe}]$ is shown for selected globular clusters with large data samples. Intra-cluster variations with respect to Mn abundance are nominal, and scatter is within observational error. However, the chosen Fe features contribute to scatter in Fe, as demonstrated in Figure 2.6. In a few cases the spread in metallicity is larger than 0.3 dex. The inclusion of more Fe lines (of both ionization states) would somewhat improve the abundance determination. So for the LTG clusters, the $[\text{Fe}/\text{H}]$ values are listed, as well as the $[\text{Fe}/\text{H}]$ ratios averaged with those reported by the original reference. Table 2.6 presents the $[\text{Fe}/\text{H}]$ and $[\text{Mn}/\text{Fe}]$ values that result from this averaging process. In the designated $[\text{Fe}/\text{H}]$ range, literature $[\text{Mn}/\text{Fe}]$ data points were found for five globular clusters: M55, M68, NGC 104, M71, and M30. These literature $[\text{Mn}/\text{Fe}]$ values are in fairly good agreement with those reported here. A few clusters in the sample were a bit problematic, and these clusters are discussed in the following sections. The noticeable data gaps in the extremely-poor metallicity range ($[\text{Fe}/\text{H}] < -2.7$ dex) and the slightly-metal poor range ($[\text{Fe}/\text{H}] > -0.7$ dex) are also addressed in section §2.4.4.

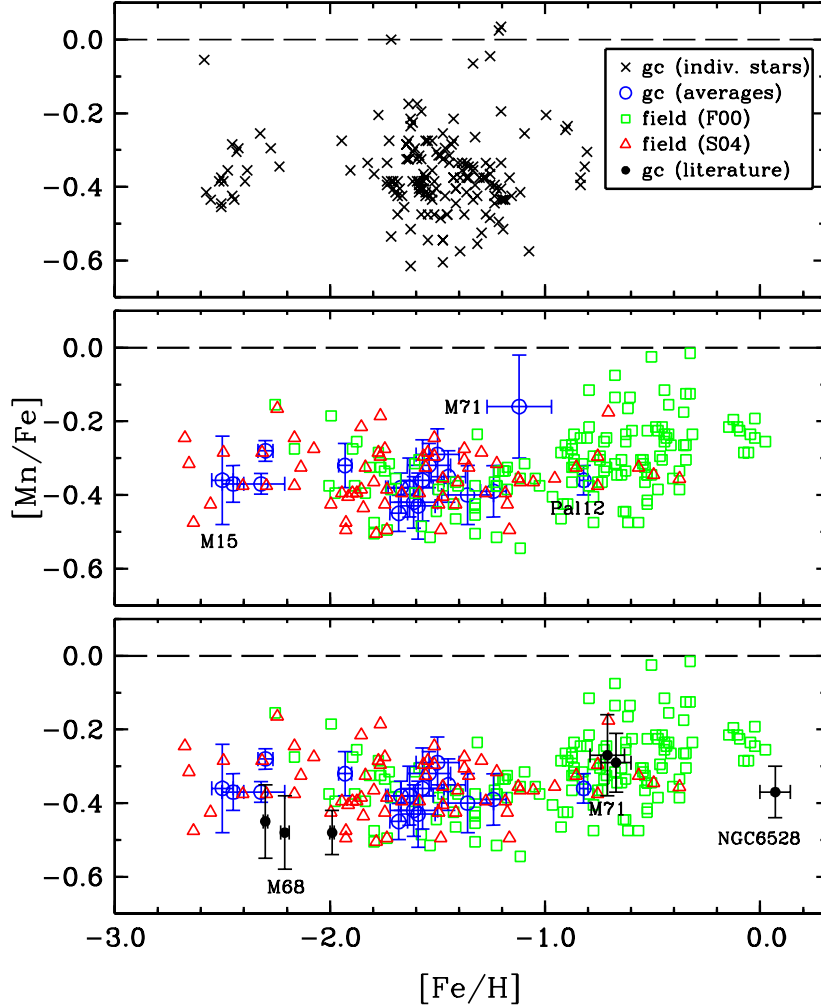


Figure 2.3 Correlation of $[\text{Mn}/\text{Fe}]$ with $[\text{Fe}/\text{H}]$ for different stellar samples. The top panel displays all of the abundances for the stars of the 19 globular cluster data sample. The middle panel shows the average $[\text{Mn}/\text{Fe}]$ and $[\text{Fe}/\text{H}]$ values for each globular cluster (with associated error bars). Field star abundances are also shown in this panel; label F00 indicates data from Fulbright (2000) and label S04 signifies data from Simmerer et al. (2004). The points for M15 and Pal 12 are designated as they represent the extremes in metallicity for the halo globular clusters of this data set. Moreover, M71 is denoted as its $\langle [\text{Mn}/\text{Fe}] \rangle$ is not consistent with the other globular cluster data points. The bottom panel presents globular cluster values from the literature. Note that the literature Mn abundances agree fairly well with those of the current study. Also, the Mn abundance for M71 from the current data sample is set aside in favor of the value published by Ramirez & Cohen (2002), as explained in §2.4

Table 2.6. LTG Cluster Mean Abundances

Cluster	N_{Stars}	$\langle[Fe/H]\rangle$	σ	$\langle[Fe/H]\rangle_{LIT}$	σ	$[Fe/H]_{AVG}$ ^a	$\langle[Mn/Fe]\rangle$	σ	$\langle[Mn/Fe]\rangle_{AVG}$ ^b
NGC 5272 (M3)	20	-1.59	0.08	-1.59	0.07	-1.59	-0.43	0.09	-0.43
NGC 5904 (M5)	31	-1.37	0.11	-1.34	0.08	-1.35	-0.40	0.08	-0.41
NGC 6121 (M4)	20	-1.24	0.06	-1.19	0.02	-1.21	-0.39	0.07	-0.42
NGC 6205 (M13)	17	-1.67	0.06	-1.60	0.05	-1.64	-0.38	0.04	-0.41
NGC 6254 (M10)	12	-1.64	0.11	-1.53	0.09	-1.58	-0.38	0.08	-0.43
NGC 6341 (M92)	4	-2.45	0.05	-2.27	0.04	-2.36	-0.37	0.05	-0.45
NGC 6838 (M71)	10	-1.13	0.15	-0.79	0.05	-0.96	-0.16	0.14	-0.32
NGC 7006	6	-1.62	0.11	-1.59	0.04	-1.60	-0.42	0.07	-0.43
NGC 7078 (M15)	11	-2.51	0.05	-2.42	0.03	-2.46	-0.36	0.12	-0.40
Pal 5	4	-1.51	0.10	-1.34	0.04	-1.42	-0.29	0.07	-0.36

^aThese values are the average of the $[Fe\ I/H]$ values from this study and literature.

^bThese values are computed using $[Fe/H](AVG)$.

2.4.1 Error Analysis

Four main factors contribute to possible errors in the abundances: choice of model, sensitivity to stellar parameters, quality of observational data, and modification of elements of the spectral fit process. To assess the ramifications of model/parameter variation across the entire data set, we studied representative stars of three metallicity classes: slightly metal-poor (SMP), moderately metal-poor (MMP), and extremely metal-poor (EMP). The selection of the stellar atmosphere model (be it MARCS or Kurucz) seemed to have little effect on either $[\text{Mn}/\text{H}]$ or $[\text{Fe}/\text{H}]$ (with a maximum change of 0.07 dex in $[\text{Fe}/\text{H}]$ for a SMP star). The relative abundances are not very responsive to slight changes in the stellar parameters. For a change of ± 100 K in T_{eff} , the largest effect was seen in the $[\text{Fe}/\text{H}]$ (± 0.10 dex) of SMP stars. An alteration in the $\log g$ value of ± 0.20 dex had a maximum response in the $[\text{Fe}/\text{H}]$ of EMP stars with a change of ± 0.10 dex. The $[\text{Mn}/\text{H}]$ value responded similarly, but taken together in the ratio $[\text{Mn}/\text{Fe}]$ the effect cancels out. And for $\Delta v_t = \pm 0.20 \text{ km s}^{-1}$, the greatest change is seen in EMP stars with ± 0.09 dex in both $[\text{Mn}/\text{H}]$ and $[\text{Fe}/\text{H}]$. Overall, the abundance error from the variation of these stellar parameters does not exceed ± 0.10 dex.

The S/N across the entire data set did vary by a substantial amount: $25 \leq S/N \leq 180$. For data of generally high quality ($S/N > 75$), the abundance determined via spectral synthesis fit is good to within ± 0.05 dex. Conversely, the fit for low quality data is not as solid and may fluctuate by as much as ± 0.10 dex. Further considerations are continuum normalization and smoothing parameters of the fit. Placement of the continuum might affect the fit by as much as ± 0.03 dex, whereas alteration of the FWHM of the fitting function (normally a Gaussian for most stars) may result in an abundance change of roughly ± 0.05 dex.

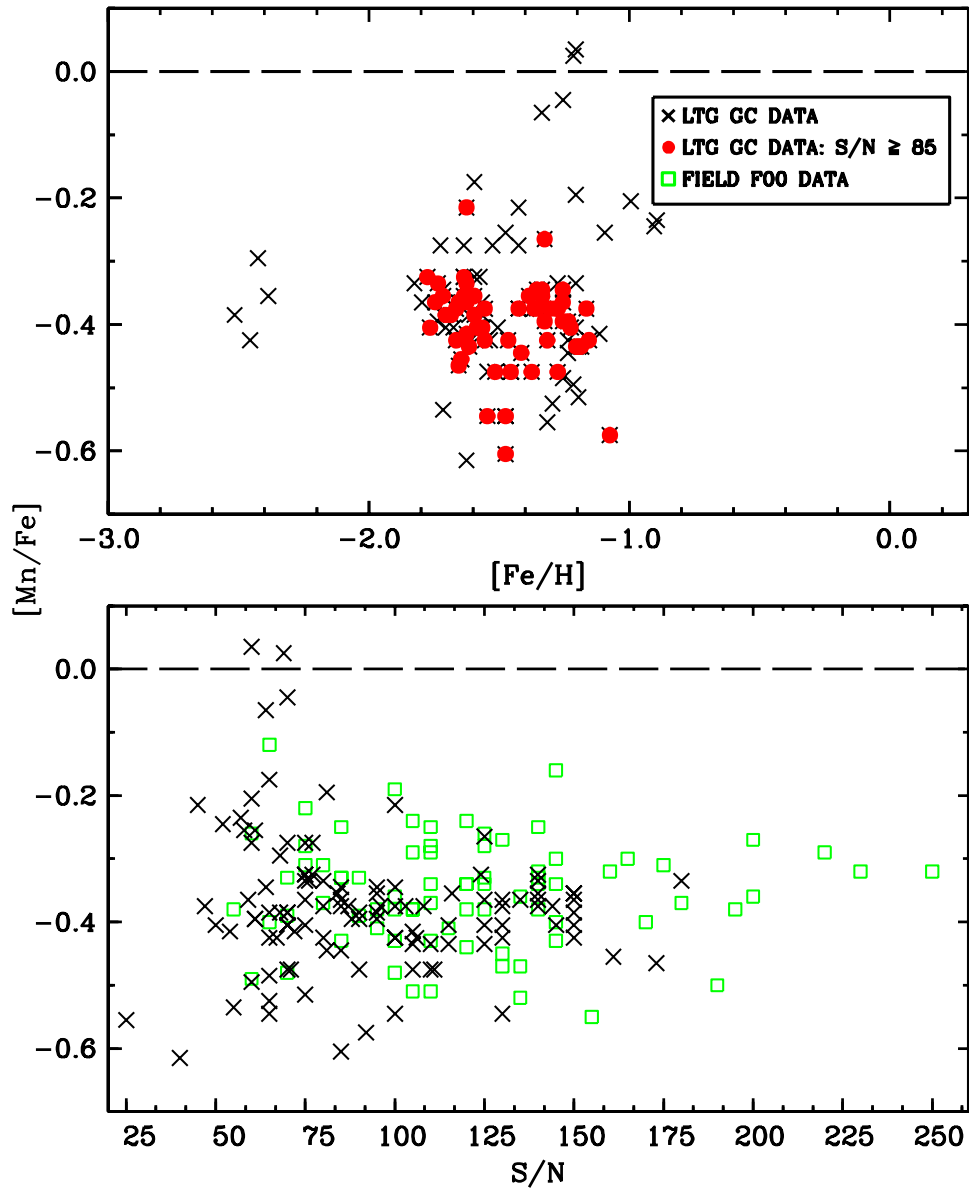


Figure 2.4 Interdependence of $[Mn/Fe]$ and S/N for the LTG data sample. The top panel presents the entire S/N range of the LTG globular cluster data set as well as those points with $S/N > 85$. The bottom panel illustrates the correlation of Mn abundances with S/N for LTG globular cluster and field data in the metallicity range $-0.7 > [Fe/H] > -2.7$.

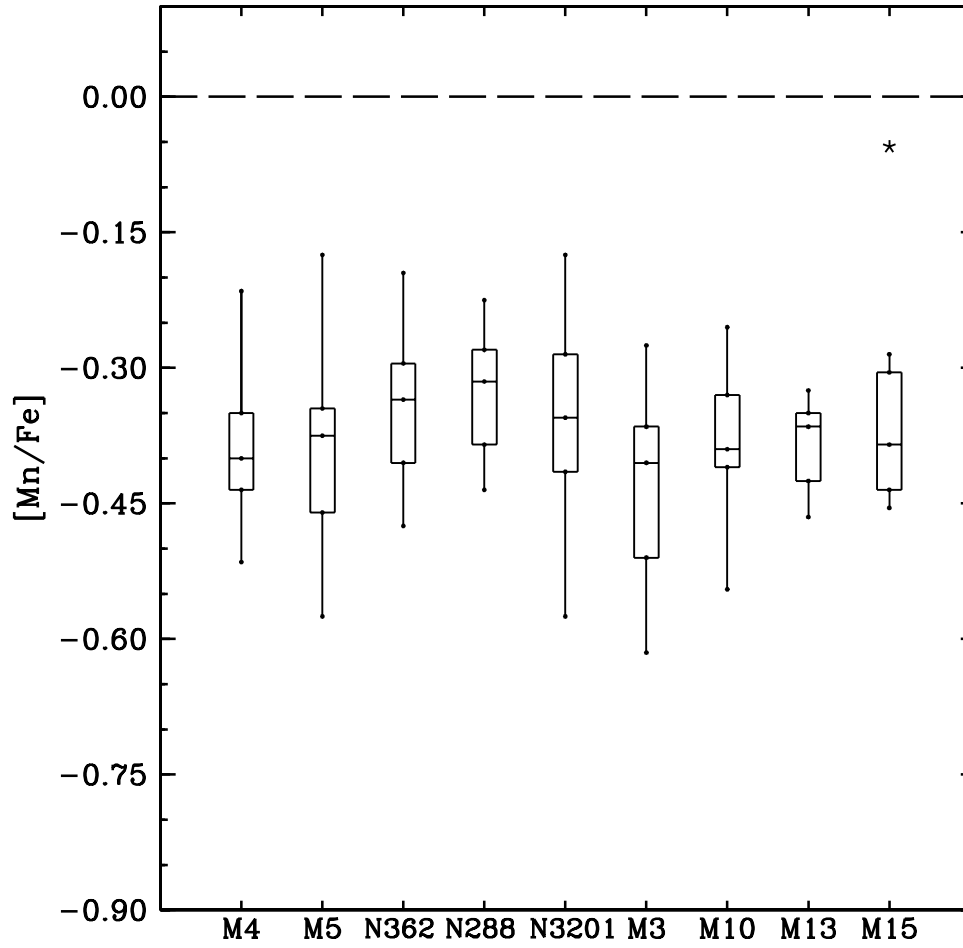


Figure 2.5 Box plots for nine representative globular clusters. For each cluster, the boxed region encompasses the interquartile (middle 50%) of its [Mn/Fe] data. Also featured are the median (horizontal line), range (vertical lines; excludes outliers), and outliers (an outlier has a value greater than 1.5 times the interquartile range). The ordering of the clusters is in decreasing $[\text{Fe}/\text{H}]_{avg}$.

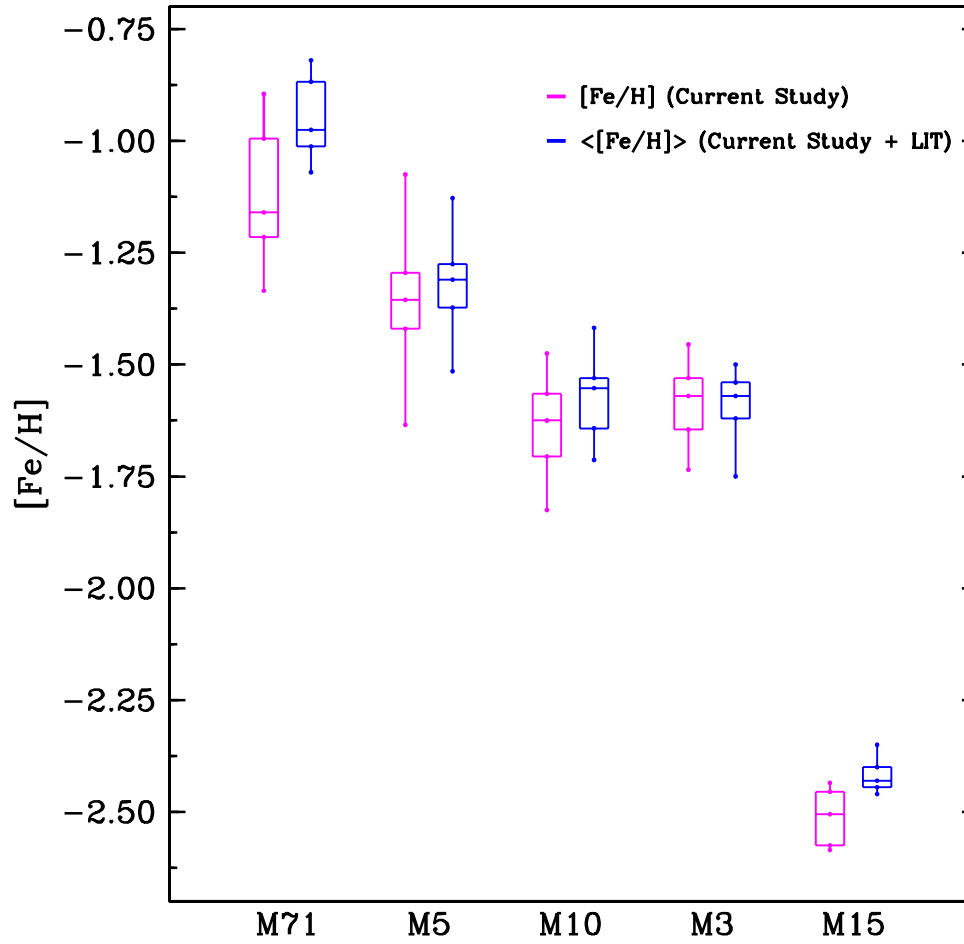


Figure 2.6 Box plots for selected globular clusters. For a few cases, averaging our derived $[Fe/H]$ values with those reported in the literature serves to reduce the spread in metallicity. As a consequence of this averaging process, the median $[Fe/H]$ value for the cluster increases. In general, marginal benefit is gained from the averaging process (as clearly illustrated by M3).

Non-LTE effects should also be taken into consideration. For metal-poor stars, overionization (and its impact on surface gravity) is indeed a factor (Thevenin & Idiart 1999), but to what degree is not clear (Kraft & Ivans 2003; Korn 2004). To date, no non-LTE Mn abundance calculations have been published for stars of any type. In a survey of metal-poor giants, Johnson (2002) attempted to quantify the effect on Mn by estimating a non-LTE $\log g$. Johnson demonstrated that modification of the $\log g$ value elicited a change of roughly -0.10 dex in Mn abundance. Ivans et al. (2001) suggest that as long as the abundance ratio consists of two neutral species (as is the case in our study) the relative non-LTE effects are minimized.

2.4.2 M71

The initial result for M71 indicated a high Mn abundance as compared to other globular clusters in our data sample. For 10 stars, $\langle[\text{Mn}/\text{Fe}]\rangle = -0.16$ ($\sigma = 0.14$) was derived with an average metallicity of $\langle[\text{Fe}/\text{H}]\rangle = -1.12$ ($\sigma = 0.15$). The data have an unusually large scatter in both Mn and Fe. It must be taken into consideration the fact that the M71 observational runs at the Lick 3.0 m telescope occurred in 1989 and 1991, prior to the update of the echelle spectrograph. If the four most anomalous data points are discounted (which correspond to the lowest S/N values), then the $\langle[\text{Fe}/\text{H}]\rangle$ for M71 becomes -1.04 ($\sigma = 0.12$) and the $\langle[\text{Mn}/\text{Fe}]\rangle$ is -0.26 ($\sigma = 0.08$). Also, if the $[\text{Fe}/\text{H}]$ ratios are averaged with those reported in the original LTG M71 study, then $\langle[\text{Fe}/\text{H}]\rangle = -0.91$ ($\sigma = 0.06$) and $\langle[\text{Mn}/\text{Fe}]\rangle = -0.38$ ($\sigma = 0.11$). With regard to these considerations, the M71 abundances are much more in line with other data points of similar metallicity. Using Keck I data acquired in 2002, Ramirez & Cohen were able to ascertain Mn abundances for M71. For this cluster, they derive $\langle[\text{Fe I}/\text{H}]\rangle = -0.71 \pm 0.08$ and $\langle[\text{Mn}/\text{Fe}]\rangle =$

-0.27 ± 0.11 . Due to the higher resolution and S/N of the Ramirez & Cohen (2002) data, their abundance values are to be preferred (Figure 2.3, bottom).

2.4.3 Comparison of Cluster Results: NGC 6528 and C261

It is possible to compare the derived [Mn/Fe] ratios of the present study to literature values for two clusters of high metallicity, NGC 6528 and Collinder 261 (Cr 261). NGC 6528 presents an opportunity to study the cluster populations of the Galactic Bulge. It lies in Baade's window and thus has only moderate reddening. Although Cr 261 is an open cluster, it may be likened to globular clusters, as it is similar in age (roughly 9 Gyr; Janes & Phelps (1994)).

For three red horizontal branch stars of NGC 6528, Carretta et al. (2001) found

$\langle [\text{Fe I}/\text{H}] \rangle = 0.07$ ($\sigma = 0.02$) and $\langle [\text{Mn}/\text{Fe}] \rangle = -0.37$ ($\sigma = 0.07$). In our examination of three different stars from this cluster, we derive mean values of $\langle [\text{Fe}/\text{H}] \rangle = -0.24$ ($\sigma = 0.19$) and $\langle [\text{Mn}/\text{Fe}] \rangle = -0.25$ ($\sigma = 0.06$). As Zoccali et al. (2004) have pointed out in their study of NGC 6528, factors that affect abundance derivations include effective temperature assessment (both spectroscopically and photometrically derived parameters contain inherent errors) and continuum determination (placement of the continuum may be largely variable due to the presence of molecular bands and α enhancement). The Fe values from the current work for this cluster do show a large spread: $-0.37 \leq [\text{Fe}/\text{H}] \leq -0.03$ (the temperature range of the sample stars is a likely factor). Also, special attention should be paid to the broadening factors used in abundance determination (Zoccali et al. 2004). While taking into consideration all the issues mentioned above, a substantial underabundance of Mn in NGC 6528 is still found.

Carretta et al. (2005) also observed six red clump and red giant branch stars in Cr 261. For this cluster, they found $\langle[\text{Fe I}/\text{H}]\rangle = -0.03$ ($\sigma = 0.04$) and $\langle[\text{Mn}/\text{Fe}]\rangle = -0.03$ ($\sigma = 0.04$). A different data set (Friel et al. 2003) was employed that contains four of the stars that were in the Carretta et al. (2005) sample. The current study’s analysis of Cr 261 giants yields $\langle[\text{Fe}/\text{H}]\rangle = -0.36$ ($\sigma = 0.21$) and $\langle[\text{Mn}/\text{Fe}]\rangle = -0.32$ ($\sigma = 0.13$). Data concerns might include instrument resolution and S/N values. Moreover, there is definite sensitivity in the data to the selection of v_t , transition probabilities, and $\log g$ values (Carretta et al. 2005). Note that there is significant scatter in the Fe abundance, and it is indeed a rather low value. In both studies, one target star gave consistently low $[\text{Fe}/\text{H}]$ and $[\text{Mn}/\text{Fe}]$ values as compared to other stars in the data set. None of the studies chose to exclude this star (most likely due to the small data sample for Cr 261). These are preliminary investigations of clusters in the metallicity regime $[\text{Fe}/\text{H}] > -0.70$ and the acquisition of more data in this range will be necessary. Future efforts will also focus on open cluster abundances.

2.4.4 Other Mn Abundance Analyses

Several investigations of the Mn abundance ratio have been done in various metallicity regimes and stellar populations. We briefly detail some of those here along with the associated $[\text{Mn}/\text{Fe}]$ results. For field stars of low metallicity ($[\text{Fe}/\text{H}] < -1.7$), Johnson (2002) obtained a subsolar Mn abundance. Studies by Cohen et al. (2004) and Francois et al. (2003) find that Mn decreases steadily below metallicity $[\text{Fe}/\text{H}] \sim -3.0$.

Examinations of Mn in metal-rich field stars are plentiful in the literature. Solar neighborhood stars in the range $-0.15 < [\text{Fe}/\text{H}] < 0.45$ have been found by Chen

et al. (2003) to possess a relatively constant $[\text{Mn}/\text{Fe}]$ ratio hovering roughly at zero. Alternatively, the solar neighborhood survey of Allende Prieto et al. (2004) reported that $[\text{Mn}/\text{Fe}]$ rises in step with $[\text{Fe}/\text{H}]$. Mn abundance determinations of the disk field stars include Feltzing & Gustafsson (1998), Prochaska et al. (2000b), and Reddy et al. (2003). Generally, these studies find that as $[\text{Fe}/\text{H}]$ approaches zero, so, accordingly, does the Mn abundance with respect to Fe (with the rough determination of the solar Mn abundance level at solar metallicity). In addition, these studies report that above $[\text{Fe}/\text{H}] = 0$, increases in $[\text{Fe}/\text{H}]$ correspond to attendant increases in $[\text{Mn}/\text{Fe}]$. E. Carretta et al. (2006, in preparation) have conducted Mn abundance analyses of several open clusters. They have found that the open clusters of their data sample do mimic the trend of the disk. Now, Prochaska et al. (2000) contend that Mn abundance differs between the thick disk and the thin disk. They conclude that Mn in the thick disk is normally underabundant with respect to the thin disk. This finding is being subjected to further scrutiny (Reddy et al. 2006).

Bulge globular clusters have not been well analyzed and remain somewhat of a mystery (the notable exception, of course, being NGC 6528). McWilliam et al. (2003) have discovered that the $[\text{Mn}/\text{Fe}]$ values of bulge giants follow the trend of disk stars. In a separate study, McWilliam et al. (2003) examined the $[\text{Mn}/\text{Fe}]$ ratio in the Sagittarius dwarf spheroidal galaxy and found a fairly consistent underabundance with respect to the stars of the bulge and disk populations. In order to have a more complete view of these metal-rich stellar populations, further study is requisite.

2.5 Discussion

Mn abundances for hundreds of globular cluster, open cluster, and halo field stars have been derived. Spectral synthesis was used in order to obtain a $[\text{Fe}/\text{H}]$ and $[\text{Mn}/\text{Fe}]$ ratio for each star. In the range $-0.7 > [\text{Fe}/\text{H}] > -2.7$, globular cluster stars exhibit a mean relative abundance of $\langle [\text{Mn}/\text{Fe}] \rangle = -0.37 \pm 0.01$ ($\sigma = 0.10$), which is the same (to within the levels of uncertainty) as that of halo field stars, $\langle [\text{Mn}/\text{Fe}] \rangle = -0.36 \pm 0.01$ ($\sigma = 0.08$). There is no statistically significant difference with regard to Mn abundance between the halo field and globular clusters.

Figure 2.7 displays the average abundance ratios of Fe-peak elements in halo field and globular cluster stars in the metallicity range $-0.7 > [\text{Fe}/\text{H}] > -2.7$. Several points may be gleaned from this plot. First, and most important, the elemental abundance ratios are equivalent in the two stellar populations. Second, the relative abundances for many members of the Fe group (Sc, V, Cr, Co, and Ni) are roughly solar over this metallicity range. And third, the abundances of a few odd Z -numbered elements (namely, Mn and Cu) are deficient with respect to their even Z -numbered Fe-peak counterparts.

Nucleosynthesis of Mn occurs primarily via decay of ^{55}Co (Nakamura et al. 1999). Another possible nucleosynthetic pathway for Mn is α -capture by ^{51}V . The main site for Mn formation is the incomplete explosive Si-burning region (Nakamura et al. 1999). In the metallicity range of interest ($-0.7 > [\text{Fe}/\text{H}] > -2.7$), core-collapse supernovae (SNe) are predominantly responsible for the production of Mn. Yields of Mn rely heavily upon the neutron excess (Umeda & Nomoto 2002). The $[\text{Mn}/\text{Fe}]$ ratio depends on the mass cut (as Fe has two production sites: the incomplete and complete Si-burning regions) and the explosion energy (with little dependence on stellar mass; Umeda & Nomoto 2002).

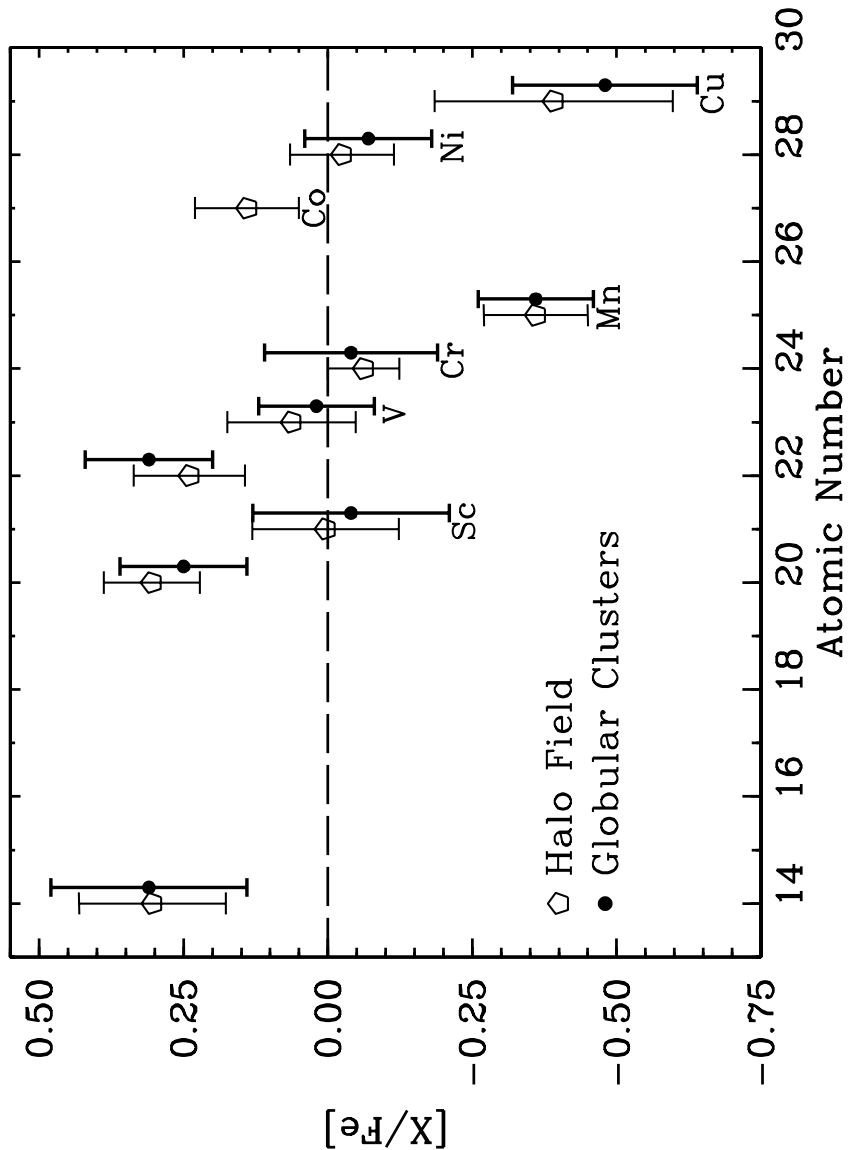


Figure 2.7 Average abundance ratios with associated standard deviation values for some of the Fe-peak and α -elements in the range $-0.7 > [Fe/H] > -2.7$. Globular cluster data are obtained from the LTG references. The Mn values are provided by the current study. Data for halo field stars for every element except Cu and Co are taken from Gratton et al. (2003) and Fulbright (2000). Cu field star data are obtained from Mishenina et al. (2002) and Co field star data are taken from Johnson (2002). Interestingly, there is a lack of Co data for globular clusters. Note that in almost every case, the average values for globular cluster and halo field stars are roughly equal to one another.

The single-valued $[\text{Mn}/\text{Fe}]$ ratio in the range $-0.7 > [\text{Fe}/\text{H}] > -2.7$ may be described as a plateau (Figure 2.3). Though the metallicity changes by roughly a factor of 100, $\langle [\text{Mn}/\text{Fe}] \rangle$ does not vary in either globular cluster or halo field stars. In the specified range, the $[\text{Mn}/\text{Fe}]$ ratio of (either stellar population) is not metallicity-dependent. These data indicate that the contribution from stars that undergo core collapse SNe (i.e., medium to moderately high mass stars) is uniform and does not change. Furthermore, the data suggest that the initial mass function (IMF) associated with these stars is essentially invariant. As Thielemann et al. (1996) contend, in the range $-1.0 \geq [\text{Fe}/\text{H}] \geq -2.5$, constant abundance ratios of elements (like those of the Fe peak) should be expected as the core collapse SNe of the entire mass range of progenitor stars occurs.

Beyond $[\text{Fe}/\text{H}] \sim -1.0$, there is an increase in the $[\text{Mn}/\text{Fe}]$ scatter for the field star data points, and the relative Mn abundance rises steadily as solar metallicity is approached (Figure 2.3). A possible explanation for the increase in scatter is that in this metallicity regime stars of three populations are present (halo, thin disk, and thick disk). Notably, Reddy et al. (2006) present data that show no difference in the Mn abundance between the stars of the thin and thick disk (of the same metallicity). The emergence of Type Ia SN events is likely responsible for the observable increase in the levels of Mn. This follows as the production of Mn occurs mostly in Type Ia SNe (e.g., Samland 1998; Iwamoto et al. 1999).

It would be advantageous to use the $[\text{O}/\text{Mn}]$ ratio in the examination of the evolution of very massive stars (the highest end of the IMF). Virtually all synthesis of O occurs in massive stars. The full extent of the mass range of core collapse progenitors produces Fe (Thielemann et al. $\sigma = 0.10$ 1996). Mn differs from Fe in that its manufacture occurs in a wide but limited portion of that mass range

for Type II SNe. Consequently, the $[\text{O}/\text{Mn}]$ ratio could provide constraints on the uppermost portion of the IMF. Unfortunately, as it pertains to this discussion, significant star-to-star variation of O abundance occurs in evolved stars of globular clusters with the diminution of O being due to the CNO and NeNa cycles of H burning (the proton-capture reactions; Denissenkov & Weiss 2004; Gratton et al. 2004). As the bulk of the current study data is from globular cluster stars, little about nucleosynthesis in massive stars would be learned from $[\text{O}/\text{Mn}]$ correlations. Work on this issue should be pursued with large field star samples that are extremely metal-poor ($[\text{Fe}/\text{H}] < -3.0$) or metal-rich ($[\text{Fe}/\text{H}] > -0.5$) in nature.

Few recent theoretical reviews of elemental yields and abundances in the metallicity range of interest, $-0.7 > [\text{Fe}/\text{H}] > -2.7$, have been published. The comprehensive investigation by Timmes et al. (1995) examined the chemical evolution of 76 stable isotopes in this range using the output from the Type II SN models of Woosley & Weaver (1995). Timmes et al. found excellent agreement between their calculations and the observational data for Cr and Ni. Although the trends for Mn, Sc, and V were well reproduced, the calculations of Timmes et al. predicted systematically lower abundance values for these elements than those found by observation. The trend for Cu was fairly well duplicated, although the actual values for the calculated abundance were quite low in contrast to observational values. The disagreement between theoretical calculations and observational results widens as the extremely low metallicity regime is considered. Limongi & Chieffi (2005) compared their yields from zero metallicity core collapse SNe to the extremely metal-poor star data of Cayrel et al. (2004). The observational data for the abundance ratios of the Fe-peak elements could not be simultaneously reproduced by any of the models (regardless of the choice of mass cut). This discrepancy encourages the continued

development of theoretical calculations.

Further elucidation of the metal-rich regime is necessary, with special emphasis paid to bulge and disk clusters. It must be determined whether NGC 6528 is unique in its chemical evolution history (as suggested by McWilliam & Rich 2004) or, indeed, whether it is representative of all bulge clusters. In addition, verification of the Mn abundance trend in the IR wavelength range and extension of this study to metal rich candidates is paramount. It would also be valuable to re-investigate Fe-peak elements such as Co and Sc with large abundance uncertainties.

Chapter 3

Determination of Neutral Chromium Oscillator Strengths

In this dissertation, branching fraction measurements from Fourier transform spectra in conjunction with published radiative lifetimes are used to determine transition probabilities for 263 lines of neutral chromium. These laboratory values were employed to derive a new photospheric abundance for the Sun. §2 contains a summary of the radiative lifetimes employed by this work. §3 describes the use of National Solar Observatory (NSO) digital archive spectra to measure Cr I branching fractions and provides a list of the new Cr I oscillator strengths. A report of the determinations of the Cr abundance in Sun and three other stars is found in §4, along with a discussion of the implications of the Cr abundance analysis.

3.1 Radiative Lifetime Measurement Summary

Cooper et al. (1997) reported radiative lifetime measurements for 131 levels of Cr I. They employed a time-resolved Laser Induced Fluorescence (LIF) technique on a

slow atomic beam of Cr atoms from a hollow cathode discharge. Cooper et al. were attentive to possible systematic errors from: (1) electronic bandwidth, linearity, and fidelity limitations, (2) flight-out-of view effects, (3) radiation trapping, (4) collisional quenching, and (5) Zeeman quantum beats. Most importantly they re-measured certain "benchmark" lifetimes to check the accuracy of their apparatus during their work on Cr I. Table 3.1 is a list of radiative lifetimes from Cooper et al. for the 65 Cr I levels included in our branching fraction study.

The $\pm 5\%$ accuracy claim of Cooper et al. (1997) may be verified by matching up their results to other (less extensive) Cr I LIF measurements. Specific comparisons of the average and the root mean square (RMS) differences between their lifetimes and other literature values are as follows: $+0.9\%$ and 2.5% respectively for three levels in common with the study by Measures et al. (1977), $+8.5\%$ and 9.0% respectively for six levels shared with the determination by Marek (1975), and -2.0% and 5.1% respectively for twenty-three levels in common with the study of Kwiatkowski et al. (1981)¹. The slightly larger discrepancy between the Cooper et al. lifetimes and those of Marek is not a concern as Marek claimed 8% uncertainty on his measurements. Two separate individual LIF lifetime measurements by Cooper et al. are in good agreement with values reported by Kwong & Measures (1980) and Hannaford & Lowe (1981). In addition, their results compare relatively well to measurements with non-LIF techniques. For example, six lifetimes determined by Marek and Richter (1973; phase-shift method) agree with the Cooper et al. measurements, as do six lifetimes measured by Becker et al. (1977; level-crossing technique).

The comparison to the National Institute of Standards and Technology (NIST) critical compilation (Martin et al. 1988) in Table 3.1 involved the summation over

¹The reference values for these differences are the Cooper et al. data.

Table 3.1. Radiative Lifetimes of 65 Cr I Levels from LIF Measurements

Configuration	Term	J	Level [cm ⁻¹]	τ [ns]		τ [ns]
				Cooper et al. 1997	Other LIF ^a	Martin et al. 1988
3d ⁵ (⁶ S)4p	z ⁷ P ^o	2	23305.01	32.2 ± 1.6	31.42 ± 0.25 ^a	31.6
					31.2 ± 1.0 ^b	...
		3	23386.35	31.5 ± 1.6	32.22 ± 0.17 ^a	32.5
		4	23498.84	30.3 ± 1.5	31.15 ± 0.08 ^a	31.7
					31.8 ± 2.5 ^c	...
					31.6 ± 0.5 ^e	...
3d ⁵ (⁶ S)4p	z ⁵ P ^o	3	26787.50	16.2 ± 0.8	17.5 ± 0.9 ^d	17.0
		2	26796.28	16.2 ± 0.8	16.7 ± 0.8 ^d	16.5
		1	26801.93	16.0 ± 0.8	17.3 ± 0.9 ^d	16.7
3d ⁴ (⁵ D)4s4p(³ P ^o)	y ⁷ P ^o	2	27728.87	6.6 ± 0.3	...	6.2
		3	27820.23	6.6 ± 0.3	...	6.7
		4	27935.26	6.6 ± 0.3	...	6.8
3d ⁴ (⁵ D)4s4p(³ P ^o)	y ⁵ P ^o	1	29420.90	76.6 ± 3.8	72.8 ± 5.5 ^d	75.8
		2	29584.62	72.9 ± 3.6	70.6 ± 3.6 ^d	72.5
		3	29824.75	69.1 ± 3.5	63.5 ± 3.0 ^d	66.5
3d ⁴ (⁵ D)4s4p(³ P ^o)	z ⁵ F ^o	1	30787.30	101 ± 5	...	110
		2	30858.82	99.1 ± 5.0	...	89.5
		3	30965.46	99.9 ± 5.0	...	89.9
		4	31106.37	94.5 ± 4.7	...	73.0
		5	31280.35	91.3 ± 4.6	...	83.3
3d ⁴ (⁵ D)4s4p(³ P ^o)	z ⁵ D ^o	0	33338.20	122 ± 6	...	103
		1	33423.79	102 ± 5	...	87.0
		2	33542.11	88.7 ± 4.4	...	79.4

all of the Einstein A-coefficients for the transitions from the upper level. In some cases the sum is incomplete and only an upper limit can be determined. The NIST critical compilation included results from a variety of techniques. Although it is not expected to be as accurate as individual LIF measurements, the NIST compilation actually agrees well with the Cooper et al. results.

Table 3.1 (cont'd)

Configuration	Term	J	Level [cm ⁻¹]	τ [ns] Cooper et al. 1997	τ [ns] Other LIF ^a	τ [ns] Martin et al. 1988
3d ⁴ (⁵ D)4s4p(¹ P ^o)	y ⁵ F ^o	3	33671.55	83.9 ± 4.2	...	77.5
		4	33816.06	83.7 ± 4.2	...	87.7
		1	40906.46	3.4 ± 0.2	...	2.8
		2	40971.29	4.5 ± 0.2	...	< 8.6
		3	41086.26	3.4 ± 0.2	...	< 9.1
3d ⁴ (⁵ D)4s4p(¹ P ^o)	x ⁵ P ^o	4	41224.78	3.4 ± 0.2	...	< 18.5
		5	41393.47	3.5 ± 0.2	...	3.3
		1	40930.31	5.6 ± 0.3	...	< 12.0
		3	41043.35	6.1 ± 0.3	...	< 6.0
		3d ⁴ (⁵ D)4s4p(¹ P ^o)	y ⁵ D ^o	0	41224.80	5.0 ± 0.3
3d ⁴ (a ³ P)4s4p(³ P ^o)	x ⁵ D ^o	1	41289.17	4.8 ± 0.2	...	< 4.0
		2	41409.03	4.7 ± 0.2	...	< 4.0
		3	41575.10	4.6 ± 0.2	...	< 6.1
		4	41782.19	4.5 ± 0.2	...	< 23.3
		0	42218.37	13.4 ± 0.7	...	7.7
3d ⁵ (⁴ G)4p	z ⁵ G ^o	1	42292.96	13.7 ± 0.7	...	8.6
		2	42438.82	14.5 ± 0.7	...	11.0
		3	42648.26	16.0 ± 0.8	...	10.0
		4	42908.57	17.6 ± 0.9	...	12.5
		2	42515.35	48.7 ± 2.4	48.5 ± 2.5 ^d	49.3
3	42538.81	49.0 ± 2.5	46.0 ± 2.5 ^d	46.3		
4	42564.85	48.8 ± 2.4	46.9 ± 2.5 ^d	47.2		
5	42589.25	48.7 ± 2.4	48.2 ± 2.5 ^d	48.8		

Table 3.1 (cont'd)

Configuration	Term	J	Level [cm ⁻¹]	τ [ns]		τ [ns] Martin et al. 1988
				Cooper et al. 1997	Other LIF ^a	
3d ⁵ (⁶ S)5p	w ⁵ P ^o	6	42605.81	50.0 ± 2.5	50.2 ± 2.5 ^d	51.0
		1	44125.90	5.5 ± 0.3	...	< 4.3
		2	44186.92	5.4 ± 0.3	...	< 3.9
3d ⁵ (⁴ G)4p	z ³ H ^o	3	44259.36	5.2 ± 0.3	...	3.8
		6	45348.73	15.6 ± 0.8	...	20
		5	45354.18	15.6 ± 0.8	...	< 21.1
3d ⁵ (⁴ G)4p	y ⁵ H ^o	4	45358.63	15.5 ± 0.8	...	< 16.7
		3	45566.02	8.8 ± 0.4	...	< 9.3
		4	45614.88	8.9 ± 0.4	...	< 9.2
		5	45663.28	8.9 ± 0.4	...	< 357.
		6	45707.36	8.8 ± 0.4	...	< 8.2
3d ⁴ 4s5s	f ⁷ D	7	45741.49	8.5 ± 0.4	...	7.7
		1	46448.60	8.7 ± 0.4	9.2 ± 0.7 ^c	< 12.0
		2	46524.84	8.7 ± 0.4	9.5 ± 0.8 ^c	< 15.8
		3	46637.21	8.6 ± 0.4	9.2 ± 0.7 ^c	< 15.4
		4	46783.06	8.7 ± 0.4	9.7 ± 0.8 ^c	< 14.8
3d ⁴ (³ H)4s4p(³ P ^o)	x ⁵ G ^o	5	46958.98	8.7 ± 0.4	9.8 ± 0.8 ^c	< 17.6
		2	47047.47	16.3 ± 0.8	15.0 ± 1.5 ^d	15.9
		3	47125.70	16.9 ± 0.8	15.2 ± 1.0 ^d	16.4
		4	47189.87	16.0 ± 0.8	...	< 476.
		6	47222.27	13.2 ± 0.7	13.9 ± 0.7 ^d	12.3
		5	47228.80	14.9 ± 0.7	14.8 ± 0.7 ^d	< 455.

^aLIF Literature References: (a) Measures et al. 1977. (b) Kwong & Measures 1980. (c) Marek 1975. (d) Kwiatowski et al. 1981. (e) Hannaford & Lowe 1981.

3.2 Branching Fractions and Atomic Transition Probabilities

The original intention of a June 2005 Kitt Peak run was to record new spectra on a variety of Fe-group species. Maintenance problems with the NSO 1.0 m Fourier Transform Spectrometer (FTS) prevented the acquisition of new data and led to an extended shutdown of this important FTS facility. Despite this setback, it was still possible to generate an expanded set of Cr I transition probabilities with existing

FTS spectra.

The primary specifications of the FTS instrument are: (1) wavenumber accuracy of 1 part in 10^8 , (2) broad spectral coverage range from the UV to the IR, (3) optimal resolution limit of 0.01 cm^{-1} , and (4) spectrum recording capability of 10^6 points in 10 minutes (Brault 1976). The FTS interferogram is a simultaneous measurement on spectral resolution elements from the UV to near IR. This gives the FTS an advantage over single-channel, sequentially-scanned grating monochromators which are more vulnerable to branching fraction errors from drifts in source performance.

A search of all spectra in the publicly-accessible digital archives of the NSO was performed. Numerous chromium spectra were located, however based on various selection criteria (i.e. range of lamp currents and relatively low buffer gas pressures) only seven were deemed acceptable. General characteristics of the spectral data set include: hollow cathode discharge (HCD) lamp sources with fused silica windows, argon or neon fills, interferograms with multiple co-adds, applied currents in the range 0.1-1.5 A, and buffer gas pressures in the range of 0.65-4.00 Torr. Details regarding the chosen spectra may be found in Table 3.2. The majority of spectra were recorded at high discharge currents. Though high current spectra yield good S/N measurements of weak lines, radiation trapping or optical depth effects arise. For instance, spectra 3-5 have serious problems of this sort even for emission lines terminating on Cr levels with 1 eV excitation potentials. Spectrum 6, although not the lowest current spectrum, has minimal optical depth problems for Cr I lines to the 1 eV lower levels. In order to resolve these optical depth problems and to improve the radiometric calibration in the near IR, additional laboratory measurements were made with a grating spectrometer which will be described in the next section.

Table 3.2. FTS Spectra Chosen for Branching Fraction Determination

Spectrum Number	Date Recorded	HC Discharge	$I_{Discharge}$ [Amps]	P_{Buffer} [Torr]	Spectral Coverage [cm^{-1}]	Limit of Resolution [cm^{-1}]	Beam Splitter	Filters	Photodiode Detector
1	06-25-1982	Cr-Ar	0.50	0.65	7664-44591	0.057	UV	CS 9-54	Mid Range Si
2	06-26-1982	Cr-Ar	0.10	1.00	7664-44591	0.057	UV	CS 9-54	Mid Range Si
3	07-26-1984	Cr-Ne	0.75	3.00	7985-45407	0.054	UV	WG295	Mid Range Si
4	07-26-1984	Cr-Ne	1.50	3.30	7985-45407	0.054	UV	WG295	Mid Range Si
5	07-26-1984	Cr-Ne	1.50	3.30	7985-45407	0.054	UV	WG295	Mid Range Si
6	02-28-1980	Cr-Ar	0.50	2.50	7908-28921	0.035	Vis	GG375	Super Blue Si
7	03-25-1980	Cr-Ne	0.95	4.00	13489-27089	0.034	Vis	GG400/CS 4.96	Super Blue Si

Essential to the branching ratio measurement is the accurate determination of the relative radiometric calibration or efficiency of the FTS. In effect, the radiometric efficiency is the quantification of the FTS instrument response. A methodology to arrive at a radiometric calibration has been established by Adams & Whaling (1981) which involves the use of selected sets of Ar I and Ar II lines in the range 4300-35,000 cm^{-1} . Confirmation and refinement of these lists of Ar I and Ar II branching ratios have subsequently been done by Danzmann & Kock (1982), Hashiguchi & Hasikuni (1985) and Whaling et al. (1993). The apparent intensity of subsets of Ar I and Ar II lines from a common upper level divided by the branching ratios of these lines is used to determine the FTS radiometric efficiency as a function of wavenumber. The radiometric calibration includes efficiency variations as a function of wavenumber from the optical components of the FTS and lamp system. Calibrations based solely on the Ar line technique were used for spectra 1, 2, and 6. Spectra of the Kitt Peak Optronics 15 A tungsten strip lamp were recorded during the 1984 run shortly before and after the Cr-Ne hollow cathode lamp spectra. This tungsten filament lamp is a secondary standard with a known spectral radiance and its spectra were used to establish a relative radiometric calibration of Cr-Ne spectra 3, 4, and 5 from 1984. A spectrum of a 6.25 A tungsten filament lamp from March 25, 1980 was used to smooth the Ar line calibration of spectrum 7 from the same date. We do not have access to the calibration curve for this standard lamp, but we were able to reconstruct a calibration using other archived FTS data from the same period. Note that tungsten filament lamp calibrations are most useful near the decline in FTS sensitivity at 12,500 cm^{-1} (attributed to the aluminum mirror coatings), and between 10,000 and 8,000 cm^{-1} , where the response of the silicon detector rapidly diminishes.

All possible transition wavenumbers between the known energy levels of Cr I satisfying both the parity change and $\Delta J = 0, \pm 1$ selection rules were computed and used during the analysis of the FTS data. Energy Levels from Sugar & Corliss (1985) were used to determine all possible transition wavenumbers. Spectral features at these wavenumbers were numerically integrated to determine apparent line intensities that are subsequently divided by the relative radiometric calibration to yield branching ratios.

The procedure for determining branching fraction uncertainties has been extensively described in Wickliffe et al. (2000). Branching fractions from a given upper level are defined to sum to unity, thus a dominant line from an upper level has small branching fraction uncertainty almost by definition. Branching fractions for weaker lines near the dominant line(s) tend to have uncertainties limited by their signal-to-noise ratios. Systematic uncertainties in the radiometric calibration are typically the most serious source of uncertainty for widely-spaced lines from a common upper level.

Branching fraction measurements were completed on 65 of the 131 levels from the lifetime experiment. Some of the levels for which branching fractions could not be obtained have significant branches which fall outside the spectral coverage region of the FTS configuration. The division of the branching fractions by the radiative lifetimes results in the transition probabilities for chromium lines. Table 3.3 presents oscillator strengths for 263 transitions of Cr I. Note that the table omits transition probability data for a few weak lines from selected upper levels. These omissions are due to excessively large uncertainties from low S/N, blending issues, and some calibration problems for weak lines widely separated from dominant branches connected to the same upper level. Branching fractions of strong lines were

Table 3.3. Atomic Transition Probabilities for Cr I Organized by Increasing Wavelength in λ_{air}

λ_{air} [Å]	E_{upper} [cm ⁻¹]	Term	J_{upper}	E_{lower} [cm ⁻¹]	Term	J_{lower}	A_{LScalc} [10 ⁶ s ⁻¹]	A_{Exp} [10 ⁶ s ⁻¹]	log gf
2726.50	44259.36	w ⁵ P ^o	3	7593.16	a ⁵ S	2	...	58±3	-0.35
2731.90	44186.92	w ⁵ P ^o	2	7593.16	a ⁵ S	2	...	52±3	-0.53
2736.46	44125.90	w ⁵ P ^o	1	7593.16	a ⁵ S	2	...	43±4	-0.83
2748.24	44186.92	w ⁵ P ^o	2	7810.82	a ⁵ D	1	...	12.3±2.0	-1.16
2748.32	44125.90	w ⁵ P ^o	1	7750.78	a ⁵ D	0	...	29±3	-1.01
2751.59	44259.36	w ⁵ P ^o	3	7927.47	a ⁵ D	2	...	4.42±0.26	-1.45
2752.86	44125.90	w ⁵ P ^o	1	7810.82	a ⁵ D	1	...	57±4	-0.71
2757.09	44186.92	w ⁵ P ^o	2	7927.47	a ⁵ D	2	...	44±3	-0.60
2761.73	44125.90	w ⁵ P ^o	1	7927.47	a ⁵ D	2	...	43±4	-0.83
2764.35	44259.36	w ⁵ P ^o	3	8095.21	a ⁵ D	3	...	25.9±2.1	-0.68
2769.90	44186.92	w ⁵ P ^o	2	8095.21	a ⁵ D	3	...	68±4	-0.41
2780.68	44259.36	w ⁵ P ^o	3	8307.57	a ⁵ D	4	...	95±5	-0.11
2871.62	42908.57	x ⁵ D ^o	4	8095.21	a ⁵ D	3	...	6.2±0.4	-1.16
2879.27	42648.26	x ⁵ D ^o	3	7927.47	a ⁵ D	2	...	12.6±0.7	-0.96
2886.99	42438.82	x ⁵ D ^o	2	7810.82	a ⁵ D	1	...	18.0±1.3	-0.95
2889.24	42908.57	x ⁵ D ^o	4	8307.57	a ⁵ D	4	...	49.1±2.5	-0.26
2893.25	42648.26	x ⁵ D ^o	3	8095.21	a ⁵ D	3	...	33.6±1.8	-0.53
2894.16	42292.96	x ⁵ D ^o	1	7750.78	a ⁵ D	0	...	19.6±1.4	-1.13
2896.75	42438.82	x ⁵ D ^o	2	7927.47	a ⁵ D	2	...	22.2±1.3	-0.85
2899.20	42292.96	x ⁵ D ^o	1	7810.82	a ⁵ D	1	...	8.2±1.1	-1.51
2905.49	42218.37	x ⁵ D ^o	0	7810.82	a ⁵ D	1	...	72±5	-1.04
2909.04	42292.96	x ⁵ D ^o	1	7927.47	a ⁵ D	2	...	41.8±2.4	-0.80
2910.90	42438.82	x ⁵ D ^o	2	8095.21	a ⁵ D	3	...	27.5±1.6	-0.76

corrected using our rough measurements on the omitted weak lines. Inaccuracies in the branching fractions of the weak lines have negligible effect on the accuracy of the branching fractions for the strong lines. The branching fraction uncertainty was combined in quadrature with the radiative lifetime uncertainty to yield the transition probability uncertainty shown in Table 3.3.

Table 3.3 (cont'd)

λ_{air} [Å]	E_{upper} [cm ⁻¹]	Term	J_{upper}	E_{lower} [cm ⁻¹]	Term	J_{lower}	A_{LScalc} [10 ⁶ s ⁻¹]	A_{Exp} [10 ⁶ s ⁻¹]	log gf
2911.14	42648.26	x ⁵ D ^o	3	8307.57	a ⁵ D	4	...	14.7±0.9	-0.88
2967.64	41782.19	y ⁵ D ^o	4	8095.21	a ⁵ D	3	...	31.8±1.8	-0.42
2971.11	41575.10	y ⁵ D ^o	3	7927.47	a ⁵ D	2	...	45.9±2.4	-0.37
2975.48	41409.03	y ⁵ D ^o	2	7810.82	a ⁵ D	1	...	53.8±2.9	-0.45
2980.79	41289.17	y ⁵ D ^o	1	7750.78	a ⁵ D	0	...	55±3	-0.66
2985.85	41409.03	y ⁵ D ^o	2	7927.47	a ⁵ D	2	...	45.9±2.6	-0.51
2986.00	41575.10	y ⁵ D ^o	3	8095.21	a ⁵ D	3	...	102±5	-0.02
2986.13	41289.17	y ⁵ D ^o	1	7810.82	a ⁵ D	1	...	14.9±2.1	-1.22
2986.47	41782.19	y ⁵ D ^o	4	8307.57	a ⁵ D	4	...	183±9	0.34
2988.65	41043.35	x ⁵ P ^o	3	7593.16	a ⁵ S	2	...	35.9±2.0	-0.47
2991.89	41224.80	y ⁵ D ^o	0	7810.82	a ⁵ D	1	...	192±10	-0.59
2995.10	40971.29	y ⁵ F ^o	2	7593.16	a ⁵ S	2	...	30.6±2.1	-0.69
2996.58	41289.17	y ⁵ D ^o	1	7927.47	a ⁵ D	2	...	130±7	-0.28
2998.78	40930.31	x ⁵ P ^o	1	7593.16	a ⁵ S	2	...	39.3±2.3	-0.80
3000.88	41409.03	y ⁵ D ^o	2	8095.21	a ⁵ D	3	...	105±5	-0.15
3005.06	41575.10	y ⁵ D ^o	3	8307.57	a ⁵ D	4	...	60±3	-0.25
3013.03	40930.31	x ⁵ P ^o	1	7750.78	a ⁵ D	0	...	20.8±1.4	-1.07
3014.76	40971.29	y ⁵ F ^o	2	7810.82	a ⁵ D	1	...	130±7	-0.05
3014.91	41086.26	y ⁵ F ^o	3	7927.47	a ⁵ D	2	...	188±11	0.25
3015.20	40906.46	y ⁵ F ^o	1	7750.78	a ⁵ D	0	...	155±9	-0.20
3017.57	41224.78	y ⁵ F ^o	4	8095.21	a ⁵ D	3	...	242±14	0.47
3018.49	40930.31	x ⁵ P ^o	1	7810.82	a ⁵ D	1	...	88±5	-0.44
3018.82	41043.35	x ⁵ P ^o	3	7927.47	a ⁵ D	2	...	23.3±1.6	-0.65

Table 3.3 (cont'd)

λ_{air} [Å]	E_{upper} [cm ⁻¹]	Term	J_{upper}	E_{lower} [cm ⁻¹]	Term	J_{lower}	A_{LScalc} [10 ⁶ s ⁻¹]	A_{Exp} [10 ⁶ s ⁻¹]	log gf
3020.67	40906.46	y ⁵ F ^o	1	7810.82	a ⁵ D	1	...	110±7	-0.35
3021.56	41393.47	y ⁵ F ^o	5	8307.57	a ⁵ D	4	...	272±16	0.61
3029.16	40930.31	x ⁵ P ^o	1	7927.47	a ⁵ D	2	...	25.0±1.4	-0.99
3030.24	41086.26	y ⁵ F ^o	3	8095.21	a ⁵ D	3	...	91±6	-0.06
3031.35	40906.46	y ⁵ F ^o	1	7927.47	a ⁵ D	2	...	22.0±1.5	-1.04
3034.19	41043.35	x ⁵ P ^o	3	8095.21	a ⁵ D	3	...	22.7±1.3	-0.66
3037.04	41224.78	y ⁵ F ^o	4	8307.57	a ⁵ D	4	...	38.5±2.4	-0.32
3040.84	40971.29	y ⁵ F ^o	2	8095.21	a ⁵ D	3	...	56±3	-0.41
3053.87	41043.35	x ⁵ P ^o	3	8307.57	a ⁵ D	4	...	73±4	-0.15
3351.96	29824.75	y ⁵ P ^o	3	0.00	a ⁷ S	3	...	0.111±0.015	-2.88
3379.16	29584.62	y ⁵ P ^o	2	0.00	a ⁷ S	3	...	0.111±0.013	-3.02
3578.68	27935.26	y ⁷ P ^o	4	0.00	a ⁷ S	3	...	152±8	0.42
3593.48	27820.23	y ⁷ P ^o	3	0.00	a ⁷ S	3	...	151±8	0.31
3605.32	27728.87	y ⁷ P ^o	2	0.00	a ⁷ S	3	...	151±8	0.17
3730.80	26796.28	z ⁵ P ^o	2	0.00	a ⁷ S	3	...	0.177±0.016	-2.73
3732.02	26787.50	z ⁵ P ^o	3	0.00	a ⁷ S	3	...	0.184±0.024	-2.57
3742.96	47228.80	x ⁵ G ^o	5	20519.60	a ⁵ G	6	...	5.1±0.3	-0.93
3743.54	47228.80	x ⁵ G ^o	5	20523.69	a ⁵ G	4	...	7.5±0.7	-0.76
3743.57	47228.80	x ⁵ G ^o	5	20523.94	a ⁵ G	5	...	50.8±2.6	0.07
3743.88	47222.27	x ⁵ G ^o	6	20519.60	a ⁵ G	6	...	71±4	0.29
3744.49	47222.27	x ⁵ G ^o	6	20523.94	a ⁵ G	5	...	4.97±0.28	-0.87
3748.61	47189.87	x ⁵ G ^o	4	20520.92	a ⁵ G	3	...	7.8±0.5	-0.83
3749.00	47189.87	x ⁵ G ^o	4	20523.69	a ⁵ G	4	...	41.7±2.2	-0.10

Table 3.3 (cont'd)

λ_{air} [Å]	E_{upper} [cm ⁻¹]	Term	J_{upper}	E_{lower} [cm ⁻¹]	Term	J_{lower}	A_{LScalc} [10 ⁶ s ⁻¹]	A_{Exp} [10 ⁶ s ⁻¹]	log gf
3749.04	47189.87	x ⁵ G ^o	4	20523.94	a ⁵ G	5	...	8.8±0.8	-0.78
3757.16	47125.70	x ⁵ G ^o	3	20517.40	a ⁵ G	2	...	6.2±0.5	-1.04
3757.66	47125.70	x ⁵ G ^o	3	20520.92	a ⁵ G	3	...	37.7±2.0	-0.25
3758.05	47125.70	x ⁵ G ^o	3	20523.69	a ⁵ G	4	...	10.6±0.7	-0.81
3768.24	47047.47	x ⁵ G ^o	2	20517.40	a ⁵ G	2	...	48.1±2.5	-0.29
3768.74	47047.47	x ⁵ G ^o	2	20520.92	a ⁵ G	3	...	11.3±0.8	-0.92
3883.29	33671.55	z ⁵ D ^o	3	7927.47	a ⁵ D	2	...	3.46±0.18	-1.26
3885.22	33542.11	z ⁵ D ^o	2	7810.82	a ⁵ D	1	...	3.94±0.20	-1.35
3886.80	33816.06	z ⁵ D ^o	4	8095.21	a ⁵ D	3	...	2.11±0.11	-1.37
3894.04	33423.79	z ⁵ D ^o	1	7750.78	a ⁵ D	0	...	3.28±0.17	-1.65
3902.91	33542.11	z ⁵ D ^o	2	7927.47	a ⁵ D	2	...	2.66±0.13	-1.52
3903.17	33423.79	z ⁵ D ^o	1	7810.82	a ⁵ D	1	...	0.85±0.05	-2.23
3908.76	33671.55	z ⁵ D ^o	3	8095.21	a ⁵ D	3	...	5.55±0.28	-1.05
3916.25	33338.20	z ⁵ D ^o	0	7810.82	a ⁵ D	1	...	7.7±0.4	-1.75
3919.15	33816.06	z ⁵ D ^o	4	8307.57	a ⁵ D	4	...	9.4±0.5	-0.71
3921.02	33423.79	z ⁵ D ^o	1	7927.47	a ⁵ D	2	...	5.37±0.27	-1.43
3928.64	33542.11	z ⁵ D ^o	2	8095.21	a ⁵ D	3	...	4.20±0.21	-1.31
3941.48	33671.55	z ⁵ D ^o	3	8307.57	a ⁵ D	4	...	2.48±0.13	-1.39
3963.69	45741.49	y ⁵ H ^o	7	20519.60	a ⁵ G	6	112	118±6	0.62
3969.06	45707.36	y ⁵ H ^o	6	20519.60	a ⁵ G	6	7.4	6.9±0.4	-0.67
3969.74	45707.36	y ⁵ H ^o	6	20523.94	a ⁵ G	5	104	105±5	0.51
3976.66	45663.28	y ⁵ H ^o	5	20523.69	a ⁵ G	4	98	93±5	0.39
3976.70	45663.28	y ⁵ H ^o	5	20523.94	a ⁵ G	5	12.8	12.7±1.1	-0.48

Table 3.3 (cont'd)

λ_{air} [Å]	E_{upper} [cm ⁻¹]	Term	J_{upper}	E_{lower} [cm ⁻¹]	Term	J_{lower}	A_{LScalc} [10 ⁶ s ⁻¹]	A_{Exp} [10 ⁶ s ⁻¹]	log gf
3983.90	45614.88	y ⁵ H ^o	4	20520.92	a ⁵ G	3	N 94	94±5	0.30
3984.34	45614.88	y ⁵ H ^o	4	20523.69	a ⁵ G	4	15.4	15.8±1.1	-0.47
3991.11	45566.02	y ⁵ H ^o	3	20517.40	a ⁵ G	2	95	100±5	0.22
3991.67	45566.02	y ⁵ H ^o	3	20520.92	a ⁵ G	3	13.4	13.8±0.8	-0.64
4025.00	45358.63	z ³ H ^o	4	20520.92	a ⁵ G	3	...	4.0±0.4	-1.05
4025.45	45358.63	z ³ H ^o	4	20523.69	a ⁵ G	4	...	0.61±0.13	-1.88
4026.21	45354.18	z ³ H ^o	5	20523.94	a ⁵ G	5	...	0.45±0.06	-1.92
4027.09	45348.73	z ³ H ^o	6	20523.94	a ⁵ G	5	...	3.53±0.29	-0.95
4254.33	23498.84	z ⁷ P ^o	4	0.00	a ⁷ S	3	...	33.0±1.7	-0.09
4261.35	46958.98	f ⁷ D	5	23498.84	z ⁷ P ^o	4	...	6.8±0.5	-0.69
4272.90	46783.06	f ⁷ D	4	23386.35	z ⁷ P ^o	3	...	4.2±0.4	-0.98
4274.80	23386.35	z ⁷ P ^o	3	0.00	a ⁷ S	3	...	31.7±1.6	-0.22
4284.72	46637.21	f ⁷ D	3	23305.01	z ⁷ P ^o	2	...	2.6±0.4	-1.30
4289.72	23305.01	z ⁷ P ^o	2	0.00	a ⁷ S	3	...	31.0±1.5	-0.37
4293.55	46783.06	f ⁷ D	4	23498.84	z ⁷ P ^o	4	...	2.53±0.22	-1.20
4299.71	46637.21	f ⁷ D	3	23386.35	z ⁷ P ^o	3	...	4.7±0.4	-1.04
4305.45	46524.84	f ⁷ D	2	23305.01	z ⁷ P ^o	2	...	7.8±1.4	-0.97
4319.64	46448.60	f ⁷ D	1	23305.01	z ⁷ P ^o	2	...	8.6±1.1	-1.14
4320.59	46524.84	f ⁷ D	2	23386.35	z ⁷ P ^o	3	...	2.7±0.3	-1.42
4320.61	46637.21	f ⁷ D	3	23498.84	z ⁷ P ^o	4	...	0.52±0.12	-1.99
4337.55	30858.82	z ⁵ F ^o	2	7810.82	a ⁵ D	1	5.65	5.75±0.29	-1.09
4339.44	30965.46	z ⁵ F ^o	3	7927.47	a ⁵ D	2	N 6.9	6.9±0.3	-0.86
4339.71	30787.30	z ⁵ F ^o	1	7750.78	a ⁵ D	0	4.70	4.66±0.23	-1.40

Table 3.3 (cont'd)

λ_{air} [Å]	E_{upper} [cm ⁻¹]	Term	J_{upper}	E_{lower} [cm ⁻¹]	Term	J_{lower}	A_{LScalc} [10 ⁶ s ⁻¹]	A_{Exp} [10 ⁶ s ⁻¹]	log gf
4344.50	31106.37	z^5F^o	4	8095.21	a^5D	3	8.4	8.7±0.4	-0.65
4351.05	30787.30	z^5F^o	1	7810.82	a^5D	1	4.67	4.40±0.22	-1.43
4351.75	31280.35	z^5F^o	5	8307.57	a^5D	4	10.0	10.6±0.5	-0.48
4356.75	47228.80	x^5G^o	5	24282.34	b^5D	4	...	2.19±0.18	-1.16
4359.62	30858.82	z^5F^o	2	7927.47	a^5D	2	3.98	3.74±0.19	-1.27
4364.15	47189.87	x^5G^o	4	24282.34	b^5D	4	...	0.39±0.07	-1.99
4368.27	47189.87	x^5G^o	4	24303.94	b^5D	3	...	1.96±0.18	-1.30
4371.26	30965.46	z^5F^o	3	8095.21	a^5D	3	2.96	2.70±0.14	-1.27
4373.26	30787.30	z^5F^o	1	7927.47	a^5D	2	0.66	0.58±0.04	-2.30
4384.96	31106.37	z^5F^o	4	8307.57	a^5D	4	1.63	1.51±0.08	-1.41
4391.74	30858.82	z^5F^o	2	8095.21	a^5D	3	0.389	0.326±0.018	-2.33
4412.23	30965.46	z^5F^o	3	8307.57	a^5D	4	0.137	0.105±0.006	-2.67
4496.84	29824.75	y^5P^o	3	7593.16	a^5S	2	...	3.38±0.18	-1.14
4526.44	42605.81	z^5G^o	6	20519.60	a^5G	6	...	17.7±0.9	-0.15
4527.33	42605.81	z^5G^o	6	20523.94	a^5G	5	...	2.12±0.11	-1.07
4529.84	42589.25	z^5G^o	5	20519.60	a^5G	6	...	1.31±0.09	-1.35
4530.68	42589.25	z^5G^o	5	20523.69	a^5G	4	...	3.11±0.27	-0.98
4530.73	42589.25	z^5G^o	5	20523.94	a^5G	5	...	16.0±0.8	-0.27
4535.12	42564.85	z^5G^o	4	20520.92	a^5G	3	...	3.48±0.20	-1.02
4535.69	42564.85	z^5G^o	4	20523.69	a^5G	4	...	13.8±0.7	-0.42
4535.75	42564.85	z^5G^o	4	20523.94	a^5G	5	...	2.33±0.14	-1.19
4539.76	42538.81	z^5G^o	3	20517.40	a^5G	2	...	2.96±0.16	-1.19
4540.49	42538.81	z^5G^o	3	20520.92	a^5G	3	...	14.0±0.7	-0.52

Table 3.3 (cont'd)

λ_{air} [Å]	E_{upper} [cm ⁻¹]	Term	J_{upper}	E_{lower} [cm ⁻¹]	Term	J_{lower}	A_{LScalc} [10 ⁶ s ⁻¹]	A_{Exp} [10 ⁶ s ⁻¹]	log gf
4541.06	42538.81	z^5G^o	3	20523.69	a^5G	4	...	3.25±0.18	-1.15
4544.60	42515.35	z^5G^o	2	20517.40	a^5G	2	...	16.6±0.9	-0.59
4545.33	42515.35	z^5G^o	2	20520.92	a^5G	3	...	3.21±0.18	-1.30
4545.95	29584.62	y^5P^o	2	7593.16	a^5S	2	...	2.75±0.14	-1.37
4565.50	29824.75	y^5P^o	3	7927.47	a^5D	2	0.306	0.432±0.028	-2.02
4580.04	29420.90	y^5P^o	1	7593.16	a^5S	2	...	2.34±0.12	-1.66
4591.39	29584.62	y^5P^o	2	7810.82	a^5D	1	0.95	1.16±0.06	-1.74
4600.74	29824.75	y^5P^o	3	8095.21	a^5D	3	2.10	2.52±0.14	-1.25
4613.36	29420.90	y^5P^o	1	7750.78	a^5D	0	2.08	2.31±0.12	-1.65
4616.12	29584.62	y^5P^o	2	7927.47	a^5D	2	3.63	4.02±0.20	-1.19
4626.17	29420.90	y^5P^o	1	7810.82	a^5D	1	4.64	4.85±0.24	-1.33
4628.47	46958.98	f^7D	5	25359.62	z^7F^o	4	0.80	1.13±0.15	-1.40
4633.26	46783.06	f^7D	4	25206.02	z^7F^o	3	2.44	2.7±0.3	-1.11
4639.50	46637.21	f^7D	3	25089.20	z^7F^o	2	5.0	5.5±0.4	-0.91
4646.15	29824.75	y^5P^o	3	8307.57	a^5D	4	7.9	8.0±0.4	-0.74
4646.79	46524.84	f^7D	2	25010.64	z^7F^o	1	8.7	8.9±0.8	-0.84
4651.28	29420.90	y^5P^o	1	7927.47	a^5D	2	3.55	3.56±0.18	-1.46
4652.15	29584.62	y^5P^o	2	8095.21	a^5D	3	N 5.68	5.68±0.29	-1.04
4654.76	46448.60	f^7D	1	24971.21	z^7F^o	0	14.5	14.7±0.9	-0.84
4663.32	46448.60	f^7D	1	25010.64	z^7F^o	1	28.8	27.9±1.7	-0.56
4663.82	46524.84	f^7D	2	25089.20	z^7F^o	2	25.9	24.7±1.4	-0.39
4664.79	46637.21	f^7D	3	25206.02	z^7F^o	3	21.5	21.8±1.2	-0.30
4666.20	45358.63	z^3H^o	4	23933.90	a^3H	4	...	4.44±0.24	-0.88

Table 3.3 (cont'd)

λ_{air} [Å]	E_{upper} [cm ⁻¹]	Term	J_{upper}	E_{lower} [cm ⁻¹]	Term	J_{lower}	A_{LScalc} [10 ⁶ s ⁻¹]	A_{Exp} [10 ⁶ s ⁻¹]	log gf
4666.48	46783.06	f ⁷ D	4	25359.62	z ⁷ F ^o	4	15.8	15.5±0.9	-0.34
4667.17	45354.18	z ³ H ^o	5	23933.90	a ³ H	4	...	1.55±0.11	-1.25
4669.33	46958.98	f ⁷ D	5	25548.64	z ⁷ F ^o	5	8.6	9.4±0.6	-0.47
4680.47	46448.60	f ⁷ D	1	25089.20	z ⁷ F ^o	2	17.1	17.3±1.1	-0.77
4689.38	46524.84	f ⁷ D	2	25206.02	z ⁷ F ^o	3	25.4	24.0±1.4	-0.40
4692.97	45358.63	z ³ H ^o	4	24056.11	a ³ H	5	...	0.24±0.04	-2.15
4693.95	45354.18	z ³ H ^o	5	24056.11	a ³ H	5	...	4.35±0.24	-0.80
4695.15	45348.73	z ³ H ^o	6	24056.11	a ³ H	5	...	1.78±0.10	-1.12
4698.47	46637.21	f ⁷ D	3	25359.62	z ⁷ F ^o	4	N 33.1	33.1±1.8	-0.11
4708.02	46783.06	f ⁷ D	4	25548.64	z ⁷ F ^o	5	41.0	39.0±2.1	0.07
4718.43	46958.98	f ⁷ D	5	25771.40	z ⁷ F ^o	6	49.2	47.3±2.5	0.24
4727.15	45348.73	z ³ H ^o	6	24200.23	a ³ H	6	...	5.2±0.3	-0.65
4745.27	42908.57	x ⁵ D ^o	4	21840.84	a ⁵ P	3	...	1.39±0.22	-1.38
4789.34	41393.47	y ⁵ F ^o	5	20519.60	a ⁵ G	6	...	12.4±1.6	-0.33
4790.34	41393.47	y ⁵ F ^o	5	20523.94	a ⁵ G	5	...	0.88±0.13	-1.48
4814.28	45663.28	y ⁵ H ^o	5	24897.55	a ³ G	4	...	1.57±0.14	-1.22
4829.31	41224.78	y ⁵ F ^o	4	20523.69	a ⁵ G	4	...	1.22±0.19	-1.42
4829.37	41224.78	y ⁵ F ^o	4	20523.94	a ⁵ G	5	...	9.8±1.4	-0.51
4836.87	45707.36	y ⁵ H ^o	6	25038.61	a ³ G	5	...	1.8±0.3	-1.09
4847.21	45663.28	y ⁵ H ^o	5	25038.61	a ³ G	5	...	0.29±0.05	-1.95
4861.19	41086.26	y ⁵ F ^o	3	20520.92	a ⁵ G	3	...	1.43±0.23	-1.45
4861.85	41086.26	y ⁵ F ^o	3	20523.69	a ⁵ G	4	...	7.7±1.1	-0.72
4870.80	45358.63	z ³ H ^o	4	24833.86	a ³ G	3	...	30.2±1.5	-0.01

Table 3.3 (cont'd)

λ_{air} [Å]	E_{upper} [cm ⁻¹]	Term	J_{upper}	E_{lower} [cm ⁻¹]	Term	J_{lower}	A_{LScalc} [10 ⁶ s ⁻¹]	A_{Exp} [10 ⁶ s ⁻¹]	log gf
4880.05	45663.28	y ⁵ H ^o	5	25177.39	a ³ F	4	...	0.67±0.15	-1.58
4885.96	45358.63	z ³ H ^o	4	24897.55	a ³ G	4	...	2.33±0.14	-1.12
4887.03	45354.18	z ³ H ^o	5	24897.55	a ³ G	4	...	30.6±1.6	0.08
4887.68	40971.29	y ⁵ F ^o	2	20517.40	a ⁵ G	2	...	0.48±0.09	-2.07
4888.52	40971.29	y ⁵ F ^o	2	20520.92	a ⁵ G	3	...	2.4±0.4	-1.36
4903.22	40906.46	y ⁵ F ^o	1	20517.40	a ⁵ G	2	...	7.7±1.3	-1.08
4920.96	45354.18	z ³ H ^o	5	25038.61	a ³ G	5	...	2.98±0.16	-0.92
4922.28	45348.73	z ³ H ^o	6	25038.61	a ³ G	5	...	50.2±2.5	0.38
4936.34	45358.63	z ³ H ^o	4	25106.34	a ³ F	3	...	16.9±0.9	-0.25
4953.71	45358.63	z ³ H ^o	4	25177.39	a ³ F	4	...	0.99±0.07	-1.48
4954.81	45354.18	z ³ H ^o	5	25177.39	a ³ F	4	...	16.6±0.9	-0.17
5013.31	41782.19	y ⁵ D ^o	4	21840.84	a ⁵ P	3	...	5.0±0.8	-0.77
5065.92	41575.10	y ⁵ D ^o	3	21840.84	a ⁵ P	3	...	1.55±0.25	-1.38
5067.72	41575.10	y ⁵ D ^o	3	21847.88	a ⁵ P	2	...	3.2±0.5	-1.07
5110.75	41409.03	y ⁵ D ^o	2	21847.88	a ⁵ P	2	...	2.4±0.4	-1.32
5113.12	41409.03	y ⁵ D ^o	2	21856.94	a ⁵ P	1	...	1.70±0.27	-1.48
5142.26	41289.17	y ⁵ D ^o	1	21847.88	a ⁵ P	2	...	0.96±0.19	-1.94
5144.66	41289.17	y ⁵ D ^o	1	21856.94	a ⁵ P	1	...	3.5±0.6	-1.37
5177.42	46958.98	f ⁷ D	5	27649.71	z ⁷ D ^o	4	6.6	6.7±0.6	-0.53
5184.55	46783.06	f ⁷ D	4	27500.37	z ⁷ D ^o	3	11.4	11.3±0.7	-0.39
5192.00	46637.21	f ⁷ D	3	27382.18	z ⁷ D ^o	2	N 14.0	14.0±0.9	-0.40
5200.21	46524.84	f ⁷ D	2	27300.19	z ⁷ D ^o	1	13.0	13.0±0.9	-0.58
5204.51	26801.93	z ⁵ P ^o	1	7593.16	a ⁵ S	2	...	52.4±2.6	-0.19

Table 3.3 (cont'd)

λ_{air} [Å]	E_{upper} [cm ⁻¹]	Term	J_{upper}	E_{lower} [cm ⁻¹]	Term	J_{lower}	A_{LScalc} [10 ⁶ s ⁻¹]	A_{Exp} [10 ⁶ s ⁻¹]	log gf
5206.04	26796.28	z^5P^o	2	7593.16	a^5S	2	...	51.9±2.6	0.02
5208.42	26787.50	z^5P^o	3	7593.16	a^5S	2	...	52.1±2.6	0.17
5220.91	46448.60	f^7D	1	27300.19	z^7D^o	1	10.7	10.6±0.7	-0.89
5224.07	46637.21	f^7D	3	27500.37	z^7D^o	3	4.0	4.7±0.5	-0.87
5224.97	46958.98	f^7D	5	27825.45	z^7D^o	5	25.6	26.0±1.5	0.07
5225.02	46783.06	f^7D	4	27649.71	z^7D^o	4	13.0	13.6±0.9	-0.30
5225.81	40971.29	y^5F^o	2	21840.84	a^5P	3	...	1.54±0.24	-1.50
5227.74	40971.29	y^5F^o	2	21847.88	a^5P	2	...	0.43±0.07	-2.05
5230.22	40971.29	y^5F^o	2	21856.94	a^5P	1	...	0.92±0.15	-1.73
5238.96	40930.31	x^5P^o	1	21847.88	a^5P	2	...	4.3±0.7	-1.27
5241.45	40930.31	x^5P^o	1	21856.94	a^5P	1	...	0.97±0.22	-1.92
5243.36	46448.60	f^7D	1	27382.18	z^7D^o	2	21.1	21.3±1.3	-0.58
5247.57	26801.93	z^5P^o	1	7750.78	a^5D	0	2.03	2.07±0.11	-1.59
5254.93	46524.84	f^7D	2	27500.37	z^7D^o	3	18.8	19.0±1.2	-0.41
5255.13	46958.98	f^7D	5	27935.26	y^7P^o	4	16.3	17.6±1.2	-0.10
5264.16	26801.93	z^5P^o	1	7810.82	a^5D	1	4.52	4.53±0.23	-1.25
5265.16	46637.21	f^7D	3	27649.71	z^7D^o	4	13.9	15.2±0.9	-0.35
5265.72	26796.28	z^5P^o	2	7810.82	a^5D	1	0.90	0.95±0.05	-1.71
5272.01	46783.06	f^7D	4	27820.23	y^7P^o	3	10.1	10.2±0.8	-0.42
5273.46	46783.06	f^7D	4	27825.45	z^7D^o	5	7.6	8.2±0.6	-0.51
5287.20	46637.21	f^7D	3	27728.87	y^7P^o	2	N 4.6	4.6±0.5	-0.87
5296.69	26801.93	z^5P^o	1	7927.47	a^5D	2	3.45	3.48±0.18	-1.36
5298.28	26796.28	z^5P^o	2	7927.47	a^5D	2	N 3.45	3.45±0.18	-1.14

Table 3.3 (cont'd)

λ_{air} [Å]	E_{upper} [cm ⁻¹]	Term	J_{upper}	E_{lower} [cm ⁻¹]	Term	J_{lower}	A_{LScalc} [10 ⁶ s ⁻¹]	A_{Exp} [10 ⁶ s ⁻¹]	log gf
5300.74	26787.50	z^5P^o	3	7927.47	a^5D	2	0.281	0.342±0.024	-2.00
5304.18	46783.06	f^7D	4	27935.26	y^7P^o	4	5.9	5.7±0.5	-0.67
5312.87	46637.21	f^7D	3	27820.23	y^7P^o	3	9.9	9.5±0.6	-0.55
5318.81	46524.84	f^7D	2	27728.87	y^7P^o	2	10.5	10.0±0.7	-0.67
5340.47	46448.60	f^7D	1	27728.87	y^7P^o	2	15.5	14.5±1.1	-0.73
5344.79	46524.84	f^7D	2	27820.23	y^7P^o	3	5.2	4.8±0.3	-0.99
5345.80	26796.28	z^5P^o	2	8095.21	a^5D	3	5.37	5.23±0.27	-0.95
5348.31	26787.50	z^5P^o	3	8095.21	a^5D	3	1.92	2.05±0.11	-1.21
5409.77	26787.50	z^5P^o	3	8307.57	a^5D	4	7.1	7.0±0.4	-0.67
5628.62	45358.63	z^3H^o	4	27597.22	b^3G	3	...	4.2±0.4	-0.74
5664.04	45354.18	z^3H^o	5	27703.84	b^3G	4	...	3.68±0.26	-0.71
5702.32	45348.73	z^3H^o	6	27816.88	b^3G	5	...	3.41±0.24	-0.67
5712.75	41782.19	y^5D^o	4	24282.34	b^5D	4	...	2.1±0.4	-1.03
5719.81	41782.19	y^5D^o	4	24303.94	b^5D	3	...	0.59±0.12	-1.58
5781.16	41575.10	y^5D^o	3	24282.34	b^5D	4	...	2.8±0.5	-1.00
5787.04	41575.10	y^5D^o	3	24299.89	b^5D	2	...	0.81±0.22	-1.55
5788.39	41575.10	y^5D^o	3	24303.94	b^5D	3	...	0.91±0.17	-1.49
5838.65	41409.03	y^5D^o	2	24286.54	b^5D	1	...	0.59±0.11	-1.82
5844.59	41409.03	y^5D^o	2	24303.94	b^5D	3	...	0.67±0.15	-1.77
5876.54	41289.17	y^5D^o	1	24277.06	b^5D	0	...	0.58±0.14	-2.05
5884.43	41289.17	y^5D^o	1	24299.89	b^5D	2	...	0.88±0.21	-1.86
6313.22	47228.80	x^5G^o	5	31393.40	a^5F	5	...	0.25±0.05	-1.78
6322.60	47189.87	x^5G^o	4	31377.96	a^5F	4	...	0.30±0.06	-1.80

Table 3.3 (cont'd)

λ_{air} [Å]	E_{upper} [cm ⁻¹]	Term	J_{upper}	E_{lower} [cm ⁻¹]	Term	J_{lower}	A_{LScalc} [10 ⁶ s ⁻¹]	A_{Exp} [10 ⁶ s ⁻¹]	log gf
8917.13	42589.25	z^5G^o	5	31377.96	a^5F	4	...	0.106±0.017	-1.86
9290.48	31280.35	z^5F^o	5	20519.60	a^5G	6	...	0.29±0.04	-1.38
9294.23	31280.35	z^5F^o	5	20523.94	a^5G	5	...	0.025±0.003	-2.45
9446.81	31106.37	z^5F^o	4	20523.69	a^5G	4	...	0.051±0.008	-2.21
9447.03	31106.37	z^5F^o	4	20523.94	a^5G	5	...	0.29±0.04	-1.46
9571.75	30965.46	z^5F^o	3	20520.92	a^5G	3	...	0.052±0.007	-2.30
9574.29	30965.46	z^5F^o	3	20523.69	a^5G	4	...	0.24±0.03	-1.63
9667.20	30858.82	z^5F^o	2	20517.40	a^5G	2	...	0.045±0.006	-2.51
9670.49	30858.82	z^5F^o	2	20520.92	a^5G	3	...	0.23±0.03	-1.79
9734.52	30787.30	z^5F^o	1	20517.40	a^5G	2	...	0.27±0.04	-1.95

3.2.1 Grating Spectrometer Measurements

Supplemental measurements were made using a 0.5m focal length grating spectrometer equipped with a set of dye and interference filters and a diode detector array. The purpose of these supplemental measurements was to verify and improve the IR radiometric calibration of the primary FTS data as well as further investigate the optical depth problems in a small portion of this data. Small, sealed Cr-Ne and Cr-Ar hollow cathode lamps were used, which are standardly found in atomic absorption spectrophotometers. To eliminate optical depth concerns during these measurements, the operational discharge current was limited to a range of 1.0-4.0 mA. Two diffraction gratings were used: a first-order 1200 groove/mm grating for broad coverage in a single exposure and an echelle grating with 316 groove/mm and a 63 degree blaze for high spectral resolution. A tungsten-quartz-halogen lamp was employed to calibrate the radiometric response of the spectrometer system (which included filters used to suppress scattered radiation). Special attention was devoted to optical depth effects in the z^5P to a^5S and z^5P to a^5D multiplets. In the so-

lar Cr abundance determination of Blackwell et al. (1987), these multiplets were specifically mentioned and will be discussed in further detail in §3.4.4.

Spot checks with the grating spectrometer were performed on the the longest wavelength z^5F to a^5G multiplets. These re-measurements indicated that in the IR, FTS data calibrated with the Optronic 15 A tungsten strip lamp were more accurate than those calibrated with the Ar I/II line method. This is in part due to the weakness of the Ar I lines at high discharge currents. However, the overwhelming majority of final transition probabilities listed in Table 3 are derived from FTS spectra.

3.2.2 Theoretical Transition Probabilities

Some of the high spin levels of transition metals such as Cr display relatively pure LS or Russell-Saunders coupling. We have used the standard LS formulae from Condon & Shortley (1935) with a frequency cubed correction to compute transition probabilities for selected multiplets in Table 3.3. The absolute scale of the transition probabilities of each multiplet was normalized to match one line in the multiplet. The lines used for these normalizations are labeled with a "N" in Table 3.3. As shown, the A-values from LS-coupling computations agree well with those from experiment (where the average and rms values of $(A_{Exp} - A_{LScalc})/A_{Exp}$ are found to be 0.011 and 0.084 respectively).

3.2.3 Comparison to Previous Studies

Numerous investigations of oscillator strengths for neutral chromium have been made with a variety of techniques. Significant experimental initiatives in this vein include the pioneering work of Corliss & Bozmann (1962), the shock tube approach

of Wolnik et al. (1968, 1969), and the arc emission method of Wujec & Weniger (1981). Theoretical determinations of Cr I transition probabilities have been done by Biémont (1974) and Kurucz & Peytremann (1975). Here, we focus on comparisons with two more recent sets of measurements: the hook and emission method of Tozzi et al. (1985) and the furnace absorption technique of Blackwell et al. (1984a, 1986). We also comment on the relationship of our gf data to those of the NIST critical compilation.

Oscillator strengths for 60 Cr I lines (which originate from 14 different upper levels) were reported by Tozzi et al. (1985). Measurements of branching fractions were done with the hook and emission method. The Tozzi et al. branching fractions were combined with the radiative lifetimes from Kwiatkowski et al. (1981) to yield the gf values with an internal accuracy of 7%. Figure 3.1 shows the differences between the log gf values from Tozzi et al. (1985) and those from this work, as a function of wavelength, transition probability, and upper level transition energy. Overall, the agreement is good between their values and those from this work. A minor trend in wavelength is seen in the upper panel of Figure 3.1: the agreement between the two data sets worsens as wavelength increases. The lower panel of Figure 3.1 displays a similar trend with E_{upper} . There are 41 transitions in common with Tozzi et al. with the average and rms values of $\log(gf)_{Tozzi} - \log(gf)_{Sobeck}$ calculated to be -0.01 and 0.04 respectively.

With the use of the furnace absorption technique, the Blackwell group published two papers (1984a, 1986) on Cr I oscillator strengths. The yield of the two efforts was 102 Cr I oscillator strengths from 38 different upper levels with an internal accuracy claim of better than 1%. Figure 3.2 displays a comparison of the Sobeck et al. gf data to that of Blackwell et al. There is excellent agree-

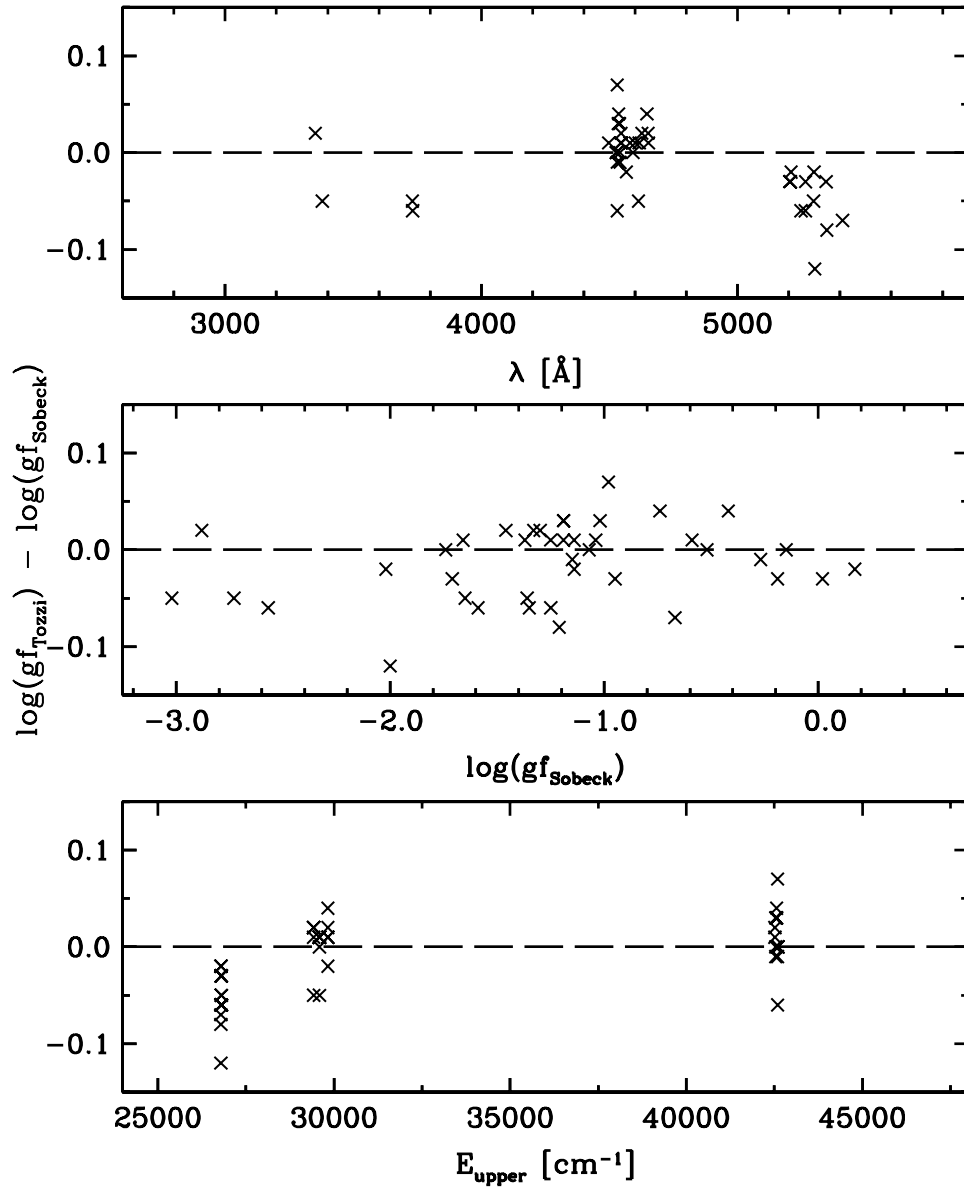


Figure 3.1 Comparison of the oscillator strength values from the current work to those of Tozzi et al. (1985). The upper panel shows the difference between the $\log(gf_{Tozzi})$ and $\log(gf_{Sobeck})$ as a function of wavelength. The middle panel displays the difference versus the $\log(gf_{Sobeck})$ values. The bottom panel illustrates the difference as a function of upper energy level (E_{upper}).

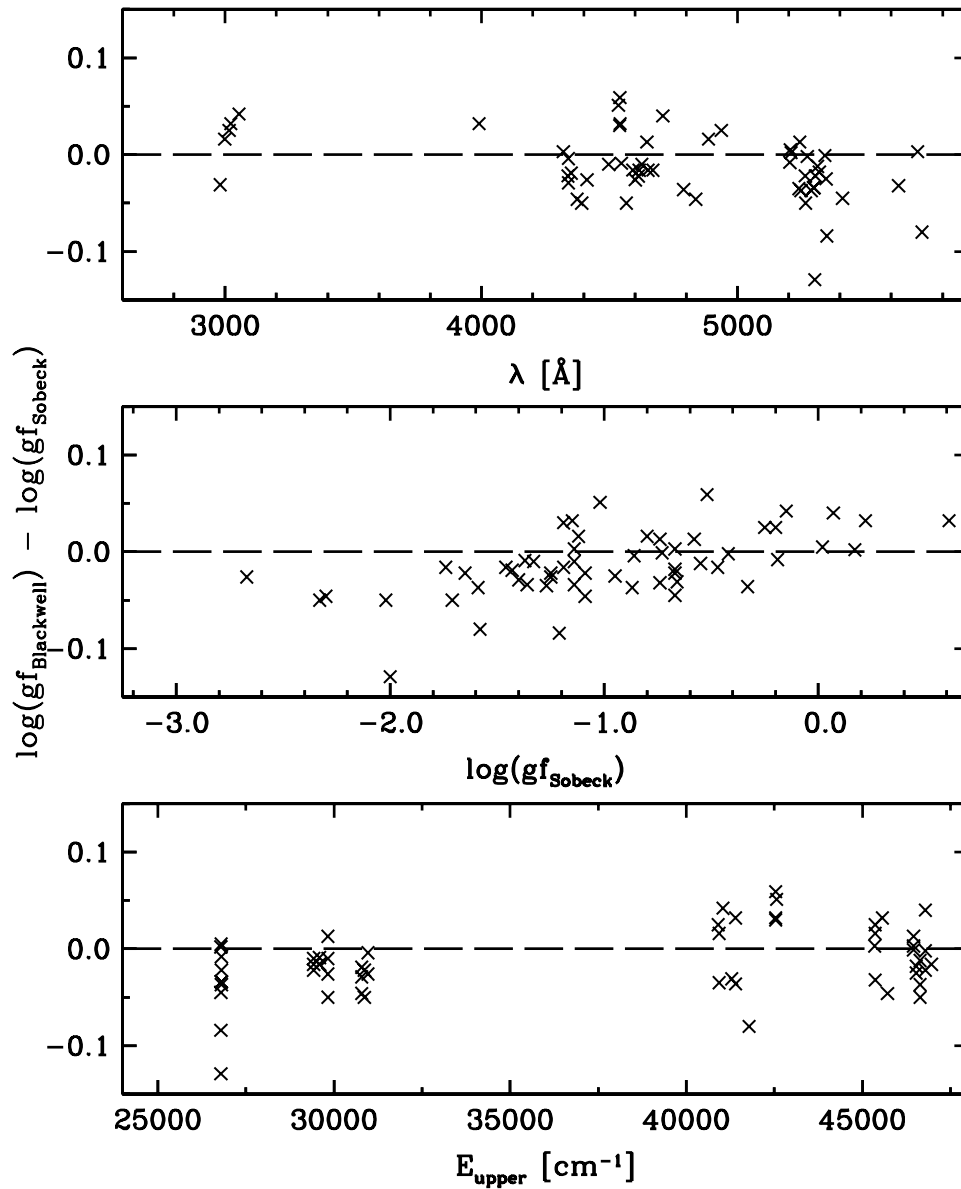


Figure 3.2 Comparison of the oscillator strength values from this study to those of Blackwell et al. (1984, 1986). The upper panel shows the difference between the $\log(gf_{Blackwell})$ and $\log(gf_{Sobeck})$ as a function of wavelength. The middle panel displays the difference versus the $\log(gf_{Sobeck})$ values. The bottom panel illustrates the difference as a function of upper energy level (E_{upper}).

ment between the 57 lines that are in common. The average and rms values of $\log(gf)_{Blackwell} - \log(gf)_{Sobeck}$ are found to be -0.01 and 0.04 respectively.

NIST has assembled a collection of Cr I transition probability data from 11 different sources (Martin et al. 1988). Classification of oscillator strengths in terms of accuracy is done by NIST as follows: $A \leq 3\%$, $B \leq 10\%$, $C \leq 25\%$, $D \leq 50\%$, and $E > 50\%$. Figure 3.3 presents the data of the current work in comparison to the NIST compilation. There are 155 transitions shared with the NIST compilation and the average and rms values of $\log(gf)_{NIST} - \log(gf)_{Sobeck}$ tabulated to be $+0.05$ and 0.12 respectively. A specific breakdown of the average and rms differences of $\log(gf)_{NIST} - \log(gf)_{Sobeck}$ with respect to the NIST oscillator strength categorization is as follows: B-level, -0.01 and 0.033 respectively; C-level: 0.10 and 0.13 respectively; D-level, 0.08 and 0.17 respectively; and E-level 0.17 and 0.17 respectively. The upper panel of Figure 3.3 shows a systematic trend with wavelength (as the wavelength decreases, the mean agreement between the two data sets diminishes and the line-to-line scatter increases). The current work presents gf data for 2 E-level and 49 D-level accuracy transitions which should be taken as an improvement and given preference over the NIST values.

3.3 Solar and Stellar Chromium Abundances

The new Cr I oscillator strength data are now applied to the solar spectrum and a few other stars. Stars chosen are of varying metallicity and evolutionary state: HD 75732 ($[\text{Fe}/\text{H}] = +0.35$; an extremely metal-rich dwarf); HD 140283 ($[\text{Fe}/\text{H}] = -2.50$; a very metal-poor subgiant); and CS 22892-052 ($[\text{Fe}/\text{H}] = -3.10$; a well-characterized, low metallicity, r-process rich giant). The Cr abundance analysis was facilitated by the existence of numerous transitions in the visible wavelength range

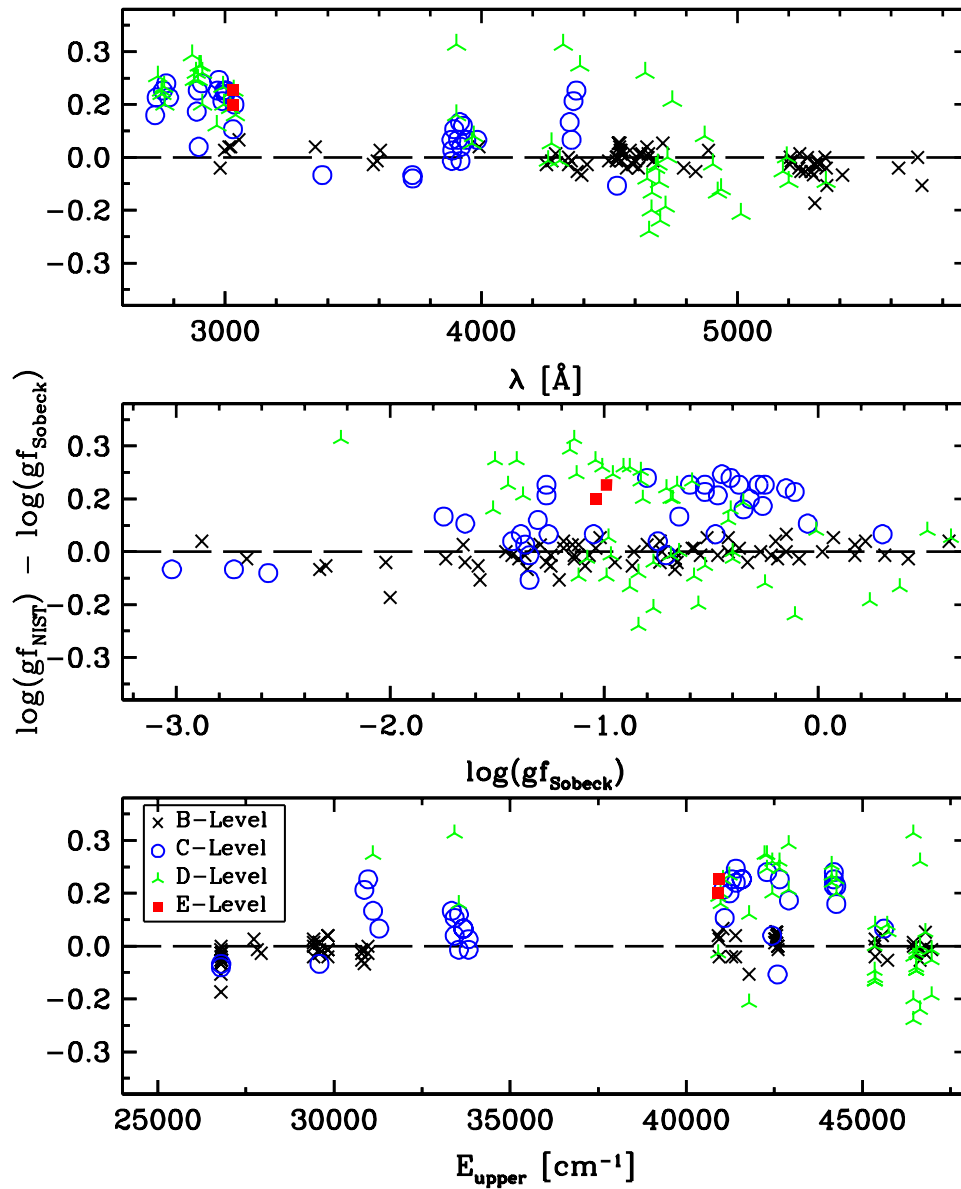


Figure 3.3 Comparison of the oscillator strength values from the present study to those of the NIST compilation. The upper panel shows the difference between the $\log(gf_{NIST})$ and $\log(gf_{Sobeck})$ as a function of wavelength. The middle panel displays the difference versus the $\log(gf_{Sobeck})$ values. The bottom panel illustrates the difference as a function of upper energy level (E_{upper}).

and the presence of both the neutral and first-ionized species.

3.3.1 Inclusion of Oscillator Strengths for Singly-Ionized Chromium from the FERRUM Project

The availability of new Cr II transition probabilities (Nilsson et al. 2006) enables the comparison of the solar abundance value from the Cr I lines to that from the Cr II lines. Nilsson et al. (2006) and the current work both employ the same technique which is the most-advanced and broadly applicable for determining transition probabilities in complex spectra. With the combination of LIF radiative lifetime determinations and FTS branching fraction measurements, they have generated a complete set of gf values for the 25 lowest odd-parity energy levels of Cr II. Nilsson et al. give oscillator strengths for 119 Cr II transitions in the wavelength range 2050-4850 Å with an uncertainty of $\sim 10 - 15\%$.

3.3.2 Line Selection and Analysis

Development of a line list suitable for stellar abundance analysis involved two selection criteria: detection of blends and determination of relative line strength. To review the numerous available chromium transitions, we employed the solar spectral identification atlas of Moore et al. (1966) and the atomic line and parameter compendium VALD (Vienna Atomic Line Database, Kupka et al. 1999). We eliminated all lines with strong core blends and those with significant wing contaminants (within 0.1 Å of the transition center). As a result, a significant number of lines (slightly less than 40% of the initial list) still remain at hand for abundance determinations.

Equivalent width analyses were sufficient to determine the elemental abundance of chromium as effects due to hyperfine and isotopic splitting were negli-

ble. Chromium has three stable isotopes: ^{52}Cr (83.79%), ^{53}Cr (9.50%), and ^{54}Cr (2.37%). A fourth isotope, ^{50}Cr (4.36%), is metastable with an extremely long half-life ($\tau > 1.8E17$ years). The odd isotope ^{53}Cr does not possess significant hyperfine structure as its nuclear g-factor is small (the dipole moment is -0.47 nuclear magnetons with $I = 3/2$). The isotopic splitting of Cr lines is imperceptible (shifts are less than 0.007 \AA , Heilig & Wendlandt 1967) and consequently, do not contribute to changes in abundance.

To measure the equivalent widths (EWs), the interactive software package SPECTRE of Fitzpatrick & Sneden (1987) was used. For a particular transition, the numerical evaluation of the equivalent width was done via the fit of a Gaussian to the line profile. No evidence of excessive damping in the wings of strong lines was detected. A few synthetic spectrum computations were done as spot-checks and no appreciable gain in accuracy was found. Table 3.4 lists the EW values for all target stars.

Table 3.4. EW Measurements for the Survey Stars

λ [Å]	χ [eV]	$\log(gf)$	$\langle EW_{Sun} \rangle$ [mÅ]	$\langle EW_{HD75732} \rangle$ [mÅ]	$\langle EW_{HD140283} \rangle$ [mÅ]	$\langle EW_{CS22892} \rangle$ [mÅ]
Cr I :						
3018.49	0.97	-0.44	101.6
3578.68	0.00	0.42	70.5	89.9
3593.48	0.00	0.31	68.5	86.5
3732.02	0.00	-2.57	55.5
3916.25	0.97	-1.75	54.0
3984.34	2.54	-0.47	52.5
4025.00	2.54	-1.05	22.8
4254.33	0.00	-0.09	65.2	...
4274.80	0.00	-0.22	61.0	...
4289.72	0.00	-0.37	55.2	90.5
4293.55	2.91	-1.20	13.2
4319.64	2.89	-1.14	15.1	44.1
4373.26	0.98	-2.30	35.6	83.9
4496.84	0.94	-1.14	82.7	...	3.9	...
4529.84	2.54	-1.35	17.1
4535.12	2.54	-1.02	29.5	68.0
4541.06	2.54	-1.15	24.3
4545.95	0.94	-1.37	78.2	131.9	2.8	...
4591.39	0.97	-1.74	61.9
4600.74	1.00	-1.25	77.8	...	2.7	...
4613.36	0.96	-1.65	66.2
4616.12	0.98	-1.19	81.0	136.8

Table 3.4 (cont'd)

λ [Å]	χ [eV]	$\log(gf)$	$\langle EW_{Sun} \rangle$ [mÅ]	$\langle EW_{HD75732} \rangle$ [mÅ]	$\langle EW_{HD140283} \rangle$ [mÅ]	$\langle EW_{CS22892} \rangle$ [mÅ]
4626.17	0.97	-1.33	76.1	...	2.6	...
4628.47	3.14	-1.40	6.1	34.7
4633.26	3.13	-1.11	9.0	38.2
4639.50	3.11	-0.91	15.1
4646.15	1.03	-0.74	92.0	16.9
4651.28	0.98	-1.46	73.7	132.1
4652.15	1.00	-1.04	92.0	...	5.4	9.7
4689.38	3.13	-0.40	36.0
4695.15	2.98	-1.12	15.3
4708.02	3.17	0.07	53.8	92.8
4718.43	3.20	0.24	62.5	105.7
4745.27	2.71	-1.38	11.7
4789.34	2.54	-0.33	59.2	99.9
4790.34	2.54	-1.48	12.5	48.9
4885.96	3.09	-1.12	12.8
4936.34	3.11	-0.25	42.4	75.4
4953.71	3.12	-1.48	4.2	22.6
5177.42	3.43	-0.53	18.1
5200.21	3.38	-0.58	20.8	56.6
5220.91	3.38	-0.89	9.8
5225.81	2.71	-1.50	12.8
5238.96	2.71	-1.27	14.9	47.9
5241.45	2.71	-1.92	3.4	19.5

Table 3.4 (cont'd)

λ [Å]	χ [eV]	$\log(gf)$	$\langle EW_{Sun} \rangle$ [mÅ]	$\langle EW_{HD75732} \rangle$ [mÅ]	$\langle EW_{HD140283} \rangle$ [mÅ]	$\langle EW_{CS22892} \rangle$ [mÅ]
5243.36	3.39	-0.58	18.6	58.9
5247.57	0.96	-1.59	77.6	125.2
5255.13	3.46	-0.10	34.3
5265.16	3.43	-0.35	24.5
5287.20	3.44	-0.87	9.8	33.5
5296.69	0.98	-1.36	87.6	144.9	...	8.0
5300.74	0.98	-2.00	54.2	103.3
5304.18	3.46	-0.67	14.4	42.9
5318.81	3.44	-0.67	13.7	45.5
5340.47	3.44	-0.73	12.9
5345.80	1.00	-0.95	107.2	187.7	5.4	13.1
5348.31	1.00	-1.21	93.4	161.3	3.2	85.0
5409.77	1.03	-0.67	125.7	...	10.0	20.5
5628.62	3.42	-0.74	14.0	44.2
5712.75	3.01	-1.03	14.7	51.1
5719.81	3.01	-1.58	4.2	20.8
5781.16	3.01	-1.00	14.1	46.7
5844.59	3.01	-1.77	3.8	21.5
Cr II :						
3382.69	2.45	-0.98	100.3	...	39.6	55.1
3391.44	2.45	-1.40	83.9	...	22.4	31.9
3393.85	3.10	-0.99	82.6	...	16.7	...
3408.81	2.48	-0.42	54.0	67.0

Table 3.4 (cont'd)

λ [Å]	χ [eV]	$\log(gf)$	$\langle EW_{Sun} \rangle$ [mÅ]	$\langle EW_{HD75732} \rangle$ [mÅ]	$\langle EW_{HD140283} \rangle$ [mÅ]	$\langle EW_{CS22892} \rangle$ [mÅ]
3511.84	2.48	-1.46	73.3	...	13.7	29.4
3585.52	2.71	-1.39	83.2
3715.18	3.10	-1.37	6.5	11.1
4558.65	4.07	-0.66	76.8	81.8	6.8	...
4588.20	4.07	-0.83	70.4	75.5	5.1	...
4592.05	4.07	-1.42	47.4	...	0.9	...
4634.08	4.07	-0.98	59.4	...	1.7	1.9
4848.25	3.86	-1.00	60.7	70.4	2.3	3.7

To gauge line strengths, reduced widths were employed, defined as $RW = EW/\lambda$. The evaluation of $\log(RW)$ for an individual line determines its position on the curve of growth (COG). Line saturation of (some) Cr I and Cr II transitions is an issue and must be dealt with accordingly. In the case of the Sun, transitions with a $\log(RW) > -4.3$ were found to lie on the exponential portion of the COG (consequently, insensitive to changes in abundance) and were immediately discarded.

For an individual specie, the determination of stellar abundances under the stipulation of LTE allows for the relation of line strengths to both transition probabilities and Boltzmann-Saha factors. A relative strength factor (RSF) may be defined as $\log gf - \theta\chi$ where χ is the excitation energy in units of eV and θ is the standard inverse temperature relation, $\theta = 5040/T$. Consequently for weak lines, $\log(RW)$ is directly proportional to the RSF. Figure 3.4 shows the computation of the RSF for neutral chromium lines in the Sun (in which case θ becomes 0.87). Notice that the 5844.59 Å line with an extremely low RSF of -6.19 is still detectable in the Sun and that the strongest transitions are located in the ultraviolet and blue visible portions of the spectrum.

With the aid of energy level information from the NIST database, the re-

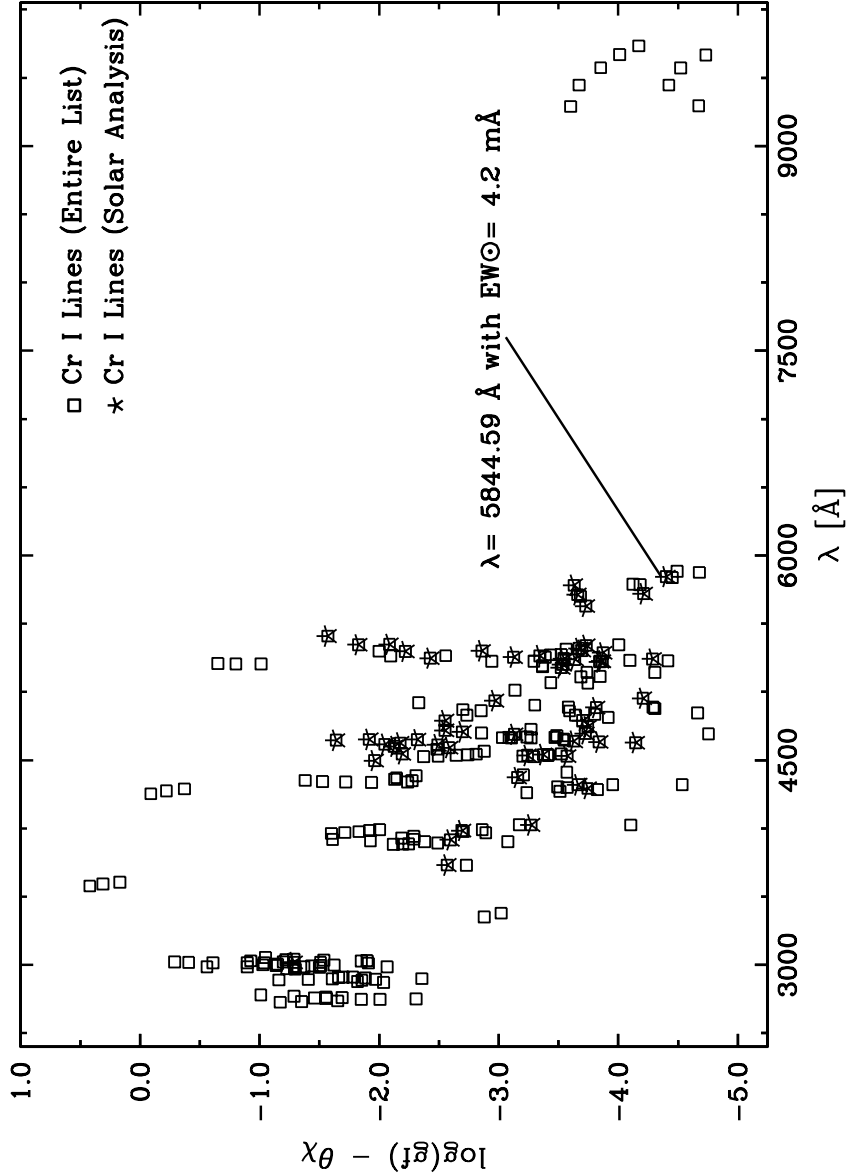


Figure 3.4 Relative strength factors (RSF) as defined by $\log(gf) - \theta\chi$ for the Cr I transitions. Reduced widths of weak lines should be proportional to these factors. For these computations, $\theta = 0.87$, the inverse of the effective temperature of the Sun. The squares indicate the RSF for all 263 Cr I lines and the stars designate those Cr I lines actually used in the derivation of the solar abundance. The 5844.59 Å line is specially noted in the plot as it is has a small RSF yet is still detectable in the solar spectrum.

computation of the partition functions for both Cr I and Cr II was done.² These data were then compared to the partition functions from Irwin (1981) and to those from Halenka & Grabowski (1986). Good agreement among the data sets was established and the newly computed partition functions for Cr II were used in the abundance determination.

3.3.3 The Solar Photospheric Chromium Abundance

For cooler stars, main sequence stars (of high surface gravity) such as the Sun, collisional line broadening must be taken into account. In these types of stellar atmospheres, the broadening of strong spectral features is predominantly due to collisions with neutral hydrogen atoms. The classical treatment of collisional broadening involves van der Waals theory and the determination of the interaction energy parameter. In the Unsold approximation (1927, 1955), the interaction energy is related to the fixed energy debt, E_p , which is set to $E_p = 4/9$ AU for all atoms regardless of species (note that from this E_p , the familiar van der Waals damping coefficient, C_6 is obtained). An improved approach (applicable to both neutral and ionized species) was developed by Anstee, Barklem, & O'Mara (hereafter labeled ABO theory; Barklem & Aspelund-Johansson 2005; Barklem et al. 1998 and references therein). Essentially, it derives the interaction energy via the analytical determination to within a single numerical integration over the radial wavefunction of the perturbed atom (O'Mara & Barklem 2003). ABO theory calculations have been done for tens of thousands of lines in the wavelength range 2300-13000 Å of elements Li to Ni with a maximum error of about 20% (Barklem & Aspelund-Johansson 2005; Barklem et al. 2000). Published collision damping constants were used (publicly available from the VALD catalog) and new calculations were requested for those Cr

²The relevant NIST website is: http://physics.nist.gov/PhysRefData/ASD/levels_form.html.

Table 3.5. Solar Photospheric Cr I and Cr II Abundances for Different Models^a

Model	$\log\epsilon(CrI)_{\odot}$	σ	$\log\epsilon(CrII)_{\odot}$	σ
Holweger-Müller (1974)	5.64 ± 0.01	0.07	5.77 ± 0.03	0.13
ATLAS (Kurucz 1993)	5.52 ± 0.01	0.08	5.69 ± 0.03	0.13
Asplund et al. (2004)	5.49 ± 0.01	0.08	5.70 ± 0.03	0.13
Grevesse & Sauval (1999)	5.58 ± 0.01	0.09	5.74 ± 0.03	0.13
NEW MARCS (1999)	5.53 ± 0.01	0.08	5.67 ± 0.03	0.13
MARCS (1975)	5.52 ± 0.01	0.07	5.68 ± 0.03	0.13

^aBarklem damping constants and a v_t of 0.80 km s^{-1} are used in all of the models.

I and Cr II transitions without published values (P. Barklem, priv. comm.).

The current version of the LTE line analysis code MOOG (Snedden 1973) was employed to calculate the abundances. The source of observed solar photospheric spectra was the center-of-disk spectral atlas of Delbouille et al. (1973). Initially, a Holweger & Müller (1974) model was selected with a microturbulent velocity of $v_t = 0.80 \text{ km s}^{-1}$. Other model types were used including: MARCS (Gustaffson et al. 1975), ATLAS (Kurucz 1993), Grevesse & Sauval (1999), newMARCS (Gustaffson et al. 2002), and Asplund et al. (2004). Table 3.5 lists the abundance data from the various models. The Holweger-Müller model was adopted as it resulted in the smallest Cr I/II abundance difference as well as the lowest internal line scatter. The mean solar photospheric abundance for 58 lines of Cr I is $\log\epsilon(Cr) = 5.64 \pm 0.01$ ($\sigma = 0.07$) and 10 lines of Cr II is $\log\epsilon(Cr) = 5.77 \pm 0.03$ ($\sigma = 0.13$).

Figure 3.5 demonstrates that Cr I abundances do not exhibit any trends with equivalent width, excitation potential, or wavelength. In this figure, the two most anomalous data points at 3018.49 \AA and 4646.15 \AA are encircled. Spectral line synthesis of these two transitions did not significantly change their respective abun-

dance values. The presence of unknown blends and the continuum determination are most certainly issues for the 3018.49 Å line. As for the feature at 4646.15 Å a slight line asymmetry is detected, however it is not possible to identify the exact cause for its aberrant abundance (as the line originates from a dominant branch, has a highly accurate transition probability, and possesses no strong contaminants). The result of the exclusion of these two transitions from the abundance determination is $\log\epsilon(\text{Cr}) = 5.64 \pm 0.01$ with $\sigma = 0.05$ (a slight decrease in the standard deviation).

For error estimation, the dependence of the chromium abundances on stellar atmospheric parameters and damping constants was considered. If the v_t is varied by $+0.2/-0.2$ km s⁻¹, then Cr I abundance changes by $-0.04/+0.03$ dex and the Cr II abundance by $-0.07/+0.06$ dex. An alteration in T_{eff} of $+100/-100$ K results in abundance changes in Cr I and Cr II of $+0.08/-0.07$ dex and $+0.00/-0.00$ dex respectively. A surface gravity variation of $\Delta\log g = +0.20/-0.20$ yields a $-0.02/0.0$ dex Cr I abundance change and a $+0.03/-0.04$ dex Cr II abundance change. If a damping constant formulation as suggested by Blackwell et al. is employed (1984b; also mentioned in Simmons & Blackwell 1982) as opposed to the Barklem values, the Cr I abundance decreases just slightly by 0.02 dex to 5.62 ± 0.01 and the Cr II abundance becomes 5.74 ± 0.03 (0.03 dex decrease). It is apparent that the singly-ionized chromium abundance is more sensitive to these parameter adjustments (in the solar photosphere, Cr II is the dominant species as chromium has a relatively small first-ionization potential, 6.766 eV Grigoriev & Meilikhov 1997). For stars with atmospheric parameters similar to the Sun, the total systematic error of the abundance values is estimated to be 0.09 dex for both Cr I (largely attributed to uncertainty in T_{eff}) and Cr II (mostly due to uncertainty in v_t).

One of the first studies to have had the benefit of both high quality spectra

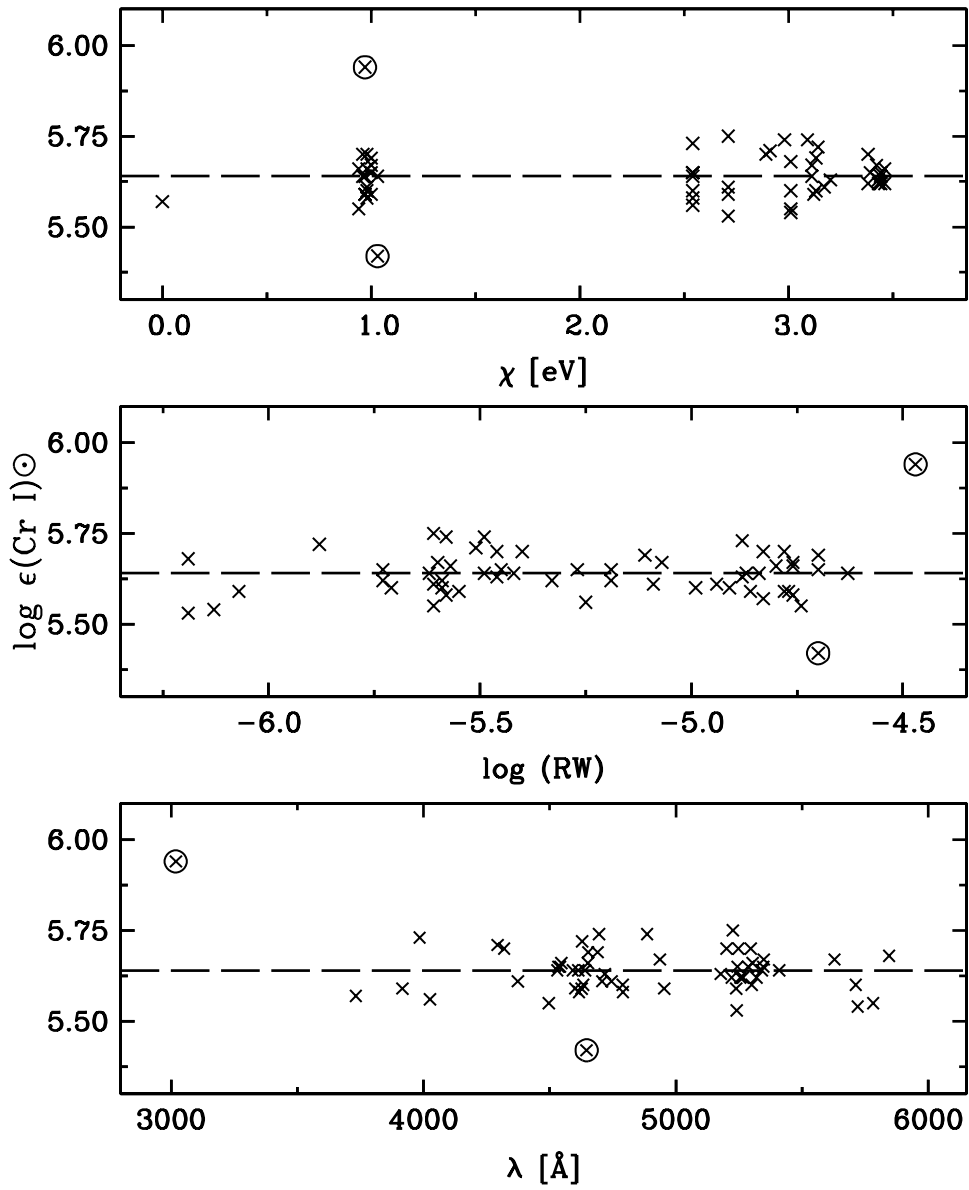


Figure 3.5 Plot of solar Cr I abundances as a function of excitation potential (χ), reduced width ($\log(\text{RW})$), and wavelength (λ). Encircled in each of the three panels are the two most erroneous abundance values. Note that these two abundance data points correspond to lines that originate from major branches. Consequently, the error in these two points cannot be attributed to oscillator strength uncertainties.

and transition probability data, Biémont et al. (1978) derived 5.64 ± 0.10 for the solar photospheric chromium abundance. The critical compilation of solar system abundances by Anders & Grevesse (1989) recommends $\log\epsilon(CrI)_{\odot} = 5.67 \pm 0.03$ (subsequent publications, Grevesse et al. 1996 and Grevesse & Sauval 1998, restate this value). Asplund et al. (2005a) find $\log\epsilon(CrI)_{\odot} = 5.64 \pm 0.10$. All of these numbers are in excellent agreement with the current meteoritic value of 5.63 ± 0.05 (Lodders 2003). None of the solar abundance determinations use lines from singly-ionized chromium. With 58 transitions, a value for the solar abundance of neutral chromium, 5.64 ± 0.01 , has been derived which is in good agreement with these values from literature.

3.3.4 No Detection of non-LTE Effects in Excitation for Neutral Chromium

Blackwell et al. (1987) reported indications of non-LTE effects in excitation for lines of neutral chromium. The abundance derivation procedure of the Blackwell group is summarized as follows: use of the solar photospheric spectral atlas by Delbouille et al. (1973); determination of collisional damping constants; employment of both the Holweger-Müller (1974) and MARCS (Gustaffson et al. 1975) model atmospheres; and EW measurement via a synthetic line profile fit to an observed transition. In contrast to the Cr I lines of higher excitation potential, they found a noticeably larger spread in the abundances from the 1 eV lines. Particularly for three transitions of the z^5P multiplet (5247.57 Å, 5300.75 Å, and 5345.80 Å), Blackwell et al. reported a markedly higher abundance ($\langle \log\epsilon_{CrI-z^5P} \rangle = 5.81$ as opposed to $\langle \log\epsilon_{CrI} \rangle = 5.69$). They did not consider that the oscillator strengths of these 1 eV lines as sources of major error since they agreed well with those gf values given by Tozzi et

al. (1985). Nor did they believe the equivalent widths were at fault (in the case of the z^5P multiplet) as Blackwell et al. were not able to detect any blends. On the basis of these two pieces of evidence, the Blackwell group concluded that non-LTE did indeed affect these Cr I lines.

In the present study, a re-examination of these low excitation chromium transitions occurs. An abnormally large scatter in the abundances of the 1 eV lines was not seen (in fact, the standard deviation for these lines was $\sigma = 0.06$; exactly the same as that for the entire line list). Also, the three transitions of the z^5P multiplet do not appear to give an anomalously high abundance ($\log\epsilon_{CrI-z^5P} = 5.65$ as compared to $\langle \log\epsilon_{CrI} \rangle = 5.64$). In addition to these three lines, the abundances for 3 more transitions of the z^5P multiplet are derived with the average for all lines equal to 5.70. Table 3.6 displays all of the results and shows that the transition probabilities from the current study for these lines agree very well with those of Blackwell et al. This table also shows a comparison of three sets of EW measurements. The values from this work agree very well with those of Moore et al. (1966). On the other hand, the Blackwell EWs are consistently higher than those of the current study. For these z^5P transitions, the exact cause of the discrepant results from the Blackwell et al. data cannot be established. In summary, there is no compelling evidence for departures from LTE in the transitions of Cr I.

Table 3.6. Comparison to the Blackwell et al. 1989 Solar Abundances^a

λ [Å]	χ [eV]	Upper Term	Upper J	Lower Term	Lower J	$\log(gf)_{Blackwell}$	$\log(gf)_{Sobeck}$	EW_{Moore} [mÅ]	$EW_{Blackwell}$ [mÅ]	EW_{Sobeck} [mÅ]	$\log\epsilon_{Blackwell}$	$\log\epsilon_{Sobeck}$
5247.57	0.96	z^5P^o	1	a^5D	0	-1.59	-1.63	76	80.1	77.6	5.81	5.71
5264.16	0.97	z^5P^o	1	a^5D	1	...	-1.25
5265.72	0.97	z^5P^o	2	a^5D	1	...	-1.71
5296.69	0.98	z^5P^o	1	a^5D	2	-1.36	-1.39	87.6	...	5.70
5298.28	0.98	z^5P^o	2	a^5D	2	-1.14	-1.17
5300.74	0.98	z^5P^o	3	a^5D	2	-2.00	-2.13	56	56.3	54.2	5.78	5.60
5345.80	1.00	z^5P^o	2	a^5D	3	-0.95	-0.98	107	116.9	107.2	5.85	5.66
5348.31	1.00	z^5P^o	3	a^5D	3	-1.21	-1.29	92	...	93.4	...	5.67
5409.77	1.03	z^5P^o	3	a^5D	4	-0.67	-0.72	125.7	...	5.64

^aFor abundance derivation, both studies employed the Holweger-Müller model. Note that Blackwell et al. used a slightly higher v_t of 0.85 km s⁻¹.

3.3.5 Chromium Abundances in Other Stars

The new Cr I and Cr II transition probability data is used to determine the [Cr/Fe] ratios in other stars. In a preliminary investigation, new values have been measured in three stars with previously established chromium abundances. These stars represent extremes in metallicity and exhibit different evolutionary states. The initial line was modified to account for the unique blending and detectability concerns of each star and performed EW measurements. Table 3.4 gives the EW data for all of the stars. An interpolation software program (kindly provided by I. Ivans and A. McWilliam) was used to generate model atmospheres from the ATLAS grid (Kurucz 1993). Abundance determinations were then undertaken (in the manner described above).

HD 75732 (ρ^1 Cnc) is a metal-rich disk main sequence star which is host to a planetary system that was first detected by Butler et al. (1997). The most recent publication of chromium abundances for this star is from the large survey by Luck & Heiter (2005). The model atmosphere parameters for HD 75732 were adopted as reported by Valenti & Fischer (2005): $(T_{eff}/\log g/[Fe/H]) = (5235/4.45/+0.25)$ which differ from those listed by Luck & Heiter: $(T_{eff}/\log g/[Fe/H]/v_t) = (5375/4.35/+0.50/0.45)$. The abundances of $\log\epsilon(\text{Cr I}) = 5.98$ ($\sigma = 0.12$, 31 lines) and $\log\epsilon(\text{Cr II}) = 6.22$ ($\sigma = 0.05$, 3 lines) were derived. The Luck & Heiter (2005) values for this star $\log\epsilon(\text{Cr I}) = 6.15$ ($\sigma = 0.14$) and $\log\epsilon(\text{Cr II}) = 6.25$ ($\sigma = 0.12$) are comparable to those of the current study (the difference between the values falls within the stated uncertainties). The discordance between the abundances from Cr I and Cr II lines for HD 75732 is 0.24 dex. With the use of the §3.4.3 solar abundances, $[\text{Cr}/\text{H}]_{\text{I}} = +0.34$ and $[\text{Cr}/\text{H}]_{\text{II}} = +0.45$ is found (which further confirms the super-metal-rich status of this star).

The subgiant HD 140283 was one of the first very metal-poor stars to be discovered (Chamberlain & Aller 1951) and has been well-studied over the past several decades. The Cr I abundance for this star was reported by King et al. (1998): $\log \epsilon(\text{Cr I}) = 2.85$ ($\sigma = 0.10$). With the model atmospheric parameters suggested by I. Ivans (5725/3.65/-2.20/1.10; priv.comm.), $\log \epsilon(\text{Cr I}) = 2.86$ ($\sigma = 0.04$, 13 lines) and $\log \epsilon(\text{Cr II}) = 3.16$ ($\sigma = 0.14$, 11 lines) was obtained. The King et al. value agrees well with those of this work though it is based on a single line. For HD 140283, the differential abundances $[\text{Cr}/\text{H}]_{\text{I}} = -2.83$ and $[\text{Cr}/\text{H}]_{\text{II}} = -2.65$ were also determined.

Sneden et al. (1994, 2003) detected a significant enhancement of *r*-process neutron-capture elements in the very metal-poor giant CS 22892-052. They were also able to determine the chromium abundances for this star: $\log \epsilon(\text{Cr I}) = 2.33$ ($\sigma = 0.11$, 6 lines) and $\log \epsilon(\text{Cr II}) = 2.42$ ($\sigma = 0.14$, 2 lines). The model atmospheric parameters (4800/1.50/-3.12/1.95) from Sneden et al. 2003 were used to derive: $\log \epsilon(\text{Cr I}) = 2.31$ ($\sigma = 0.13$, 9 lines) and $\log \epsilon(\text{Cr II}) = 2.54$ ($\sigma = 0.13$, 7 lines). The values of the present study agree reasonably well with those reported by Sneden et al (and most likely supersede them). In addition, for CS 22892-052 the differential abundances are found: $[\text{Cr}/\text{H}]_{\text{I}} = -3.33$ and $[\text{Cr}/\text{H}]_{\text{II}} = -3.23$.

These data offer a brief snapshot of the chromium abundance trend with metallicity in the Galaxy. They suggest that the disagreement in abundance values from Cr I and Cr II widens as the metallicity decreases (the derivation of Fe abundances and subsequent $[\text{Cr}/\text{Fe}]$ determination awaits an investigation with a larger available data pool analyzed in a consistent manner). The difference appears to grow from $\simeq -0.1$ at $[\text{Fe}/\text{H}] > 0$ to perhaps as much as $\simeq -0.3$ at $[\text{Fe}/\text{H}] < -2.5$ (though the effect is substantially lessened if the solar abundance discrepancy be-

tween the two species is acknowledged). Finally, it is emphasized that the chosen model parameters are taken from the literature, and these choices impact the derived abundances.

3.3.6 Chromium Ionization Imbalance Result of Departures from LTE?

It has been shown that factors such as model grid selection, stellar atmospheric parameter choice, and equivalent width measurement technique cannot fully account for the sizable abundance discrepancy between the Cr I and Cr II lines (which was detected in all stars). In the case of the Sun, the difference between $\log\epsilon_{CrI} = 5.64$ ($\sigma = 0.07$) and $\log\epsilon_{CrII} = 5.77$ ($\sigma = 0.13$) is $\Delta = 0.13$. Note though that this difference does fall within the error of $\sigma = 0.15$ (by the quadrature addition of sigmas).

The inability to reconcile the abundances from the neutral and first-ionized states of a particular species is not unique. Even with the reference element Fe there are difficulties: the solar abundances from Fe I and Fe II transitions are likewise discordant. In the 1990's, multiple papers quoted different values for the photospheric abundance of Fe I and Fe II (e.g. Milford et al. 1994; Blackwell et al. 1995; Holweger et al. 1995; Anstee et al. 1997; and Schnabel et al. 1999). We are not aware of a study that simultaneously examines both Fe I and Fe II with atomic data obtained from one, sole laboratory technique and with abundances derived from a single, consistent methodology.

For every element, accurate determinations of the oscillator strengths for the majority ionic species is critical. Numerous challenges face laboratory spectroscopists. Large wavelength separations between dominant UV branches (2000 Å to

3000 Å) and minor IR branches (7000 Å to 10000 Å) from the same upper level hinder the radiometric calibration process (the frequency cubed scaling of the A values means for instance that a 2500 Å branch is $27\times$ stronger than 7500 Å branch with a similar dipole matrix element from the same upper level). For the dominant UV branches, the uncertainty depends upon the lifetime measurement. However, it is rarely useful to obtain abundances from these branches as they generally correspond to highly-saturated transitions. On the other hand for the weak IR branches, the uncertainty limitation is the branching fractions (as by definition they must sum to 1.0). Errors may also result from optical depth effects. The possibility exists for the weaker branches to drop into the noise before the discharge current is low enough to ensure that the dominant UV branches are optically thin.

In spite of these cautions, the transition probabilities are not believed to be a significant error source. All possible steps were taken to ensure the rigorous determination of the Cr I gf-values. The Cr II oscillator strengths from the FERRUM Project (Nilsson et al. 2006) are of the highest quality (“state-of-the-art” techniques were employed). They took steps to avoid optical depth effects. Furthermore, the Cr I/Cr II abundance disagreement is not consistent with optical depth problems in the Cr II branching fraction study. Note that the Nilsson et al. branching fractions compare well with those generated by the Cowan code (1981). Figure 3.6 displays the branching fractions associated with the Cr I and Cr II transitions used in the solar abundance analysis. As shown, only the weak branches of Cr II (with inherent errors in their associated A values of 9-37%) were employed.

Given that the average abundance from Cr I lines is markedly lower than that from Cr II lines and the ostensible reliability of the oscillator strengths, other possible causes should now be considered with special focus on departures from

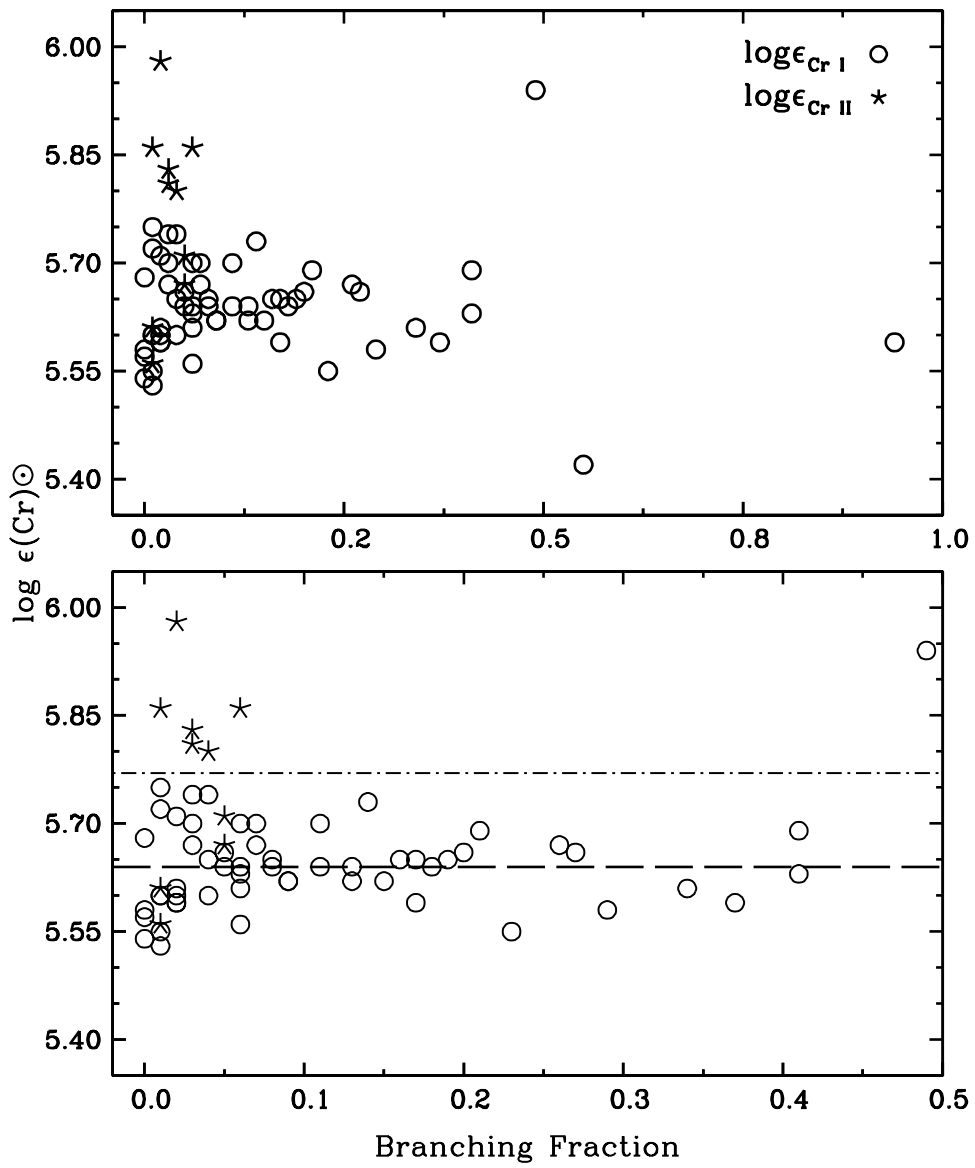


Figure 3.6 Branching Fractions for the Cr I and Cr II lines used in the solar abundance analysis. The lower panel (which is an enlarged view of the upper) shows the average abundance from the Cr I transitions (dashed line) as well as that from the Cr II transitions (dash-dotted line).

LTE. Unfortunately, a published set of non-LTE calculations for Cr has not been located. Eventually, non-LTE effects will be quantified for a variety of elements (Asplund et al. 2005b and references therein). It is reasonable to expect that the non-LTE effects on the ionization balance will be larger than non-LTE effects on level populations in a single ionization stage. Estimations of the non-LTE influence on the solar photospheric abundances of some elements have been done by several groups. For example, Shchukina & Trujillo (2001) suggest that non-LTE effects for Fe I lines might be as large as 0.1 dex. Future work on chromium should include (for instance) the precise re-measurement of the minor Cr II branches and the commencement of statistical equilibrium calculations.

3.4 Conclusion

Published lifetimes combined with branching fractions measured with Fourier transform spectrometry to determine transition probabilities for 263 lines of Cr I. This improved set of oscillator strengths has been used to determine the solar photospheric abundance of Cr I, $\log\epsilon = 5.64 \pm 0.01$ ($\sigma = 0.07$), from 58 lines. The spectra of three other stars (HD 140283, CS 22892-052, and HD 75732) was analyzed, employing 9 to 31 Cr I lines per star.

Ionization equilibrium in chromium was not achieved with the employment of plane-parallel models and LTE line formation codes. Abundances from Cr I transitions were found to be consistently lower than those from Cr II lines. Speculations as to the possible causes of the discrepancy are mentioned above. Contributions from internal and external error sources cannot account for the difference. Note that the suppression of the Cr I abundance relative to that of Cr II is commensurate with the idea of Cr I overionization. Therefore, it is believed that the discrepancy may

possibly be due to non-LTE effects. This contention is not novel in that several other groups have suggested that departures from LTE effect element abundances in the Sun (e.g. Shchukina & Trujillo Beno 2001, Takeda et al. 2005).

Steps toward the resolution of the chromium ionization imbalance problem include the re-measurement of the Cr II branching fractions and the reanalysis of the Cr abundance with a 3-dimensional hydrodynamical model.

Chapter 4

Semi-Empirical Derivations of Infrared Wavelength Transition Probabilities

4.1 Introduction

In the previous chapter, abundance determinations relied exclusively on gf-values taken from laboratory measurements. Note also that only lines in the wavelength range 3000-5900 Å were employed. Extension of abundance analyses into the red visible and infrared wavelength regime is paramount. However for both the neutral and first-ionized species of chromium, there are inherent obstacles to the accurate determination of oscillator strengths for red transitions.¹ Several of the red Cr I lines are even to odd parity decays and the measurement of radiative lifetimes (associated with these transitions) requires a (more) complex experimental set-up.

¹This also applies to most elements of the iron peak group.

Generally, red Cr II lines originate from weak branches that correspond to short-lived odd parity levels and the precise determination of gf-values for such transitions is problematic. As a consequence, the transition probability data for some red lines are either unreliable or unavailable. Alternatively, a semi-empirical approach may be employed to calculate gf-values. §2 defines the relevant quantities and gives the key relations for transition probability determinations. §3 discusses the essential tenets of LS Coupling theory. Then, §4 describes the initial efforts to derive transition probabilities with the use of radiative lifetimes obtained from laboratory measurements in conjunction with line strengths computed via Russell-Saunders coupling.

4.2 Key Relations in Oscillator Strength Determinations

The ensuing discussion follows from Cowley et al. (2000). The transition probability (A_{ik}) for a (electronic) decay from an upper state i to a lower state k is related to the measurable parameters, branching fraction (BF_{ik}) and radiative lifetime (τ_i) by

$$A_{ik} = \frac{BF_{ik}}{\tau_i} \quad (4.1)$$

where

$$BF_{ik} = \frac{A_{ik}}{\sum_k A_{ik}} = \frac{I_{ik}}{\sum_k I_{ik}} \quad (4.2)$$

and

$$\tau_i = \left(\sum_k A_{ik} \right)^{-1} \quad (4.3)$$

In essence, a (BF_{ik}) is found via the measurement of the intensity of the decay line (λ_{ik}) relative to the total intensity of all decay transitions from the upper level i . It is also convenient to define a branching ratio (BR) between two decay channels as

$$BR = \frac{A_{ik}}{A_{ij}} \quad (4.4)$$

Another relevant quantity for transitions (especially from a theoretical perspective) is the line strength

$$S = S(i, k) = S(k, i) = |R_{ik}|^2 \quad (4.5)$$

where R_{ik} is the radial matrix element (of the corresponding multipole operator, P).

The current work considers only electric dipole (E1, allowed) transitions and accordingly, the relationships between A_{ik} , the oscillator strength f_{ik} , and S are given by

$$A_{ki} = \frac{2\pi e^2}{m_e c \epsilon_o \lambda^2} \frac{g_i}{g_k} f_{ik} = \frac{16\pi^3}{3h\epsilon_o \lambda^3 g_k} S \quad (4.6)$$

Rearrangement as well as a slight simplification of Eq. 4.6 yields

$$g_i f_{ik} = 1.499 \times 10^{-8} A_{ki} \lambda^2 g_k = 303.8 \lambda^{-1} S \quad (4.7)$$

where g_i and g_k represent the statistical weights of the upper and lower levels respectively. Hence, any of the three main quantities A_{ik} , f_{ik} , and S may be found if

the radiative lifetimes (and the branching fractions) are known.

4.3 Derivation of Transition Probabilities for Pure LS Multiplets

Standard definitions and terminology are employed here wherein a set of $(2S + 1)(2L + 1)$ states associated with a particular configuration constitute a term and the ensemble of all transitions which connect one term (L, S) to another term (L', S') are called a multiplet. In Russell-Saunders or LS Coupling, J is defined as the vector sum of L and S ($J = L + S$). Selection rules for LS multiplet transitions are as follows: $\Delta S = 0$ and $\Delta J = 0, \pm 1$ (an inherent implication of these rules is the prohibition of *intersystem*, e.g. singlet-quintet, transitions). It is noteworthy to mention supermultiplet transitions which are concerned with a single electron loosely coupled to a parent core with angular moment L_p (other valence electrons are mere spectators). For a supermultiplet, the quantum numbers become $J \rightarrow L$, $L \rightarrow l$, and $S \rightarrow L_p$. The current work performed supermultiplet calculations for a few levels of Chromium (and these data were found to be in good agreement with those from LS calculations; see Table 3.3).² Note that LS multiplets are the more general and applicable case as true supermultiplets are rare occurrences.

For many energy levels, configuration mixing takes place. However if the term interaction is minimal, then relative strengths of the multiplet may be found from the Condon & Shortley (1959) formulae. Accordingly for $\Delta L = 0$, these relations are

²The Condon & Shortley formulae for individual line strength determinations within a multiplet may be used also for supermultiplet strengths with the appropriate quantum number substitutions.

$$S(\gamma SLJ, \gamma' SLJ + 1) = (-1)^2 \frac{(J-S+L+1)(J+S-L+1)(S+L+J+2)(S+L-J)}{4(J+1)} |\langle \gamma L | P | \gamma' L' \rangle|^2$$

$$S(\gamma SLJ, \gamma' SLJ + 1) = (2J + 1) \frac{[J(J+1) - S(S+1) + L(L+1)]^2}{4J(J+1)} |\langle \gamma L | P | \gamma' L' \rangle|^2$$

$$S(\gamma SLJ, \gamma' SLJ - 1) = (-1)^2 \frac{(J-S+L)(J+S-L)(S+L+J+1)(S+L+1-J)}{4J} |\langle \gamma L | P | \gamma' L' \rangle|^2$$

where the quantum number γ signifies the configuration and P is the dipole moment (operator). Then, the total multiplet line strength is given by

$$\sum_{j'} S(\gamma SLJ, \gamma' SLJ + 1) = (2J + 1)(L + 1)(2L + 3) |\langle \gamma L | P | \gamma' L' \rangle|^2 \quad (4.8)$$

Similarly for $\Delta L = -1$, the Condon & Shortley formulae are

$$S(\gamma SLJ, \gamma' SL - 1J + 1) = (-1)^2 \frac{(J+S-L+1)(L+S-J)(J+S-L+2)(S+L-J-1)}{4(J+1)} |\langle \gamma L | P | \gamma' L' \rangle|^2$$

$$S(\gamma SLJ, \gamma' SL - 1J) = (2J + 1) \frac{(J+L-S)(J+S-L+1)(S+L+1+J)(S+L-J)}{4J(J+1)} |\langle \gamma L | P | \gamma' L' \rangle|^2$$

$$S(\gamma SLJ, \gamma' SL - 1J - 1) = \frac{(J+L-S-1)(J+L-S)(S+L+J+1)(S+L+J)}{4J} |\langle \gamma L | P | \gamma' L' \rangle|^2$$

and total multiplet line strength is

$$\sum_{j'} S(\gamma SLJ, \gamma' SL - 1J') = (2J + 1)L(2L + 1) |\langle \gamma L | P | \gamma' L - 1 \rangle|^2 \quad (4.9)$$

Though not done here, a parallel set of equations may also be written for $\Delta L = +1$. Accordingly for any LS multiplet, the general corollary known as the sum rule holds in that the sum of the line strengths of lines from a given initial level is proportional to the statistical weight $(2J + 1)$ of that initial level; and likewise, the sum of the line strengths of lines from a given final level is proportional to the statistical weight $(2J + 1)$ of that final level.

In consideration of the sum rule, a more modern formulation of the relative line strength in LS-coupling multiplets may be written as

$$S \propto (2J' + 1)(2J + 1)W^2(LL'JJ'; 1S) \quad (4.10)$$

where W is a Racah coefficient (Cowley et al. 2000; the relevant group theory is not discussed here). With these relative strength calculations and a reference gf or τ value, determinations of remaining oscillator strengths from the multiplet can be done.

4.4 Accuracy Determination and Potential Applications

A simple Fortran code has been assembled to calculate the relative strength data. The first element chosen for gf determination is Cr I as its radiative lifetimes are readily accessible. Table 4.1 lists some of the preliminary results.

For the multiplet above (which has little configuration or term mixing), the comparison to experimental values is very good. As shown in Table 4.2, further

Table 4.1. Comparison of Semi-Empirically and Laboratory-Derived Transition Probabilities for Cr I Multiplets

λ_{air} [Å]	E_{upper} [cm ⁻¹]	Term	J_{upper}	E_{lower} [cm ⁻¹]	Term	J_{lower}	A_{Exp} [10 ⁶ s ⁻¹]	A_{LScalc} [10 ⁶ s ⁻¹]
5204.51	26801.93	z^5P^o	1	7593.16	a^5S	2	52.4	52.5
5206.04	26796.28	z^5P^o	2	7593.16	a^5S	2	51.9	51.7
5208.42	26787.50	z^5P^o	3	7593.16	a^5S	2	52.1	52.1

calculations will be done for other Cr I multiplets. Since the multiplets are of varying leading percentage (which indicates level of term mixing), the relationship between multiplet purity and accuracy of semi-empirical oscillator strengths will be established. With the aid of additional radiative lifetimes (from experiment), the transition probabilities for the even parity levels of Cr I will be found. The elements Ti and Ni are prime targets as the radiative lifetime measurements are also readily available. Note that computations of the radial matrix elements do not occur here (those are beyond the scope of the current work and require Hartree-Fock, Dirac-Fock, and other similar quantum methods).

Table 4.2. Prospective Cr I Multiplets for Transition Probability Calculation

λ_{air} [Å]	E_{upper} [cm ⁻¹]	Term	J_{upper}	Leading Percentage ^a	E_{lower} [cm ⁻¹]	Term	J_{lower}	A_{Exp} [10 ⁶ s ⁻¹]
3014.76	40971.29	y ⁵ F ^o	2	83	7810.82	a ⁵ D	1	130
3014.91	41086.26	y ⁵ F ^o	3	83	7927.47	a ⁵ D	2	188
3015.20	40906.46	y ⁵ F ^o	1	84	7750.78	a ⁵ D	0	155
3017.57	41224.78	y ⁵ F ^o	4	82	8095.21	a ⁵ D	3	242
3020.67	40906.46	y ⁵ F ^o	1	84	7810.82	a ⁵ D	1	110
3021.56	41393.47	y ⁵ F ^o	5	82	8307.57	a ⁵ D	4	272
3030.24	41086.26	y ⁵ F ^o	3	83	8095.21	a ⁵ D	3	91
3031.35	40906.46	y ⁵ F ^o	1	84	7927.47	a ⁵ D	2	22
3037.04	41224.78	y ⁵ F ^o	4	82	8307.57	a ⁵ D	4	38.5
3040.84	40971.29	y ⁵ F ^o	2	83	8095.21	a ⁵ D	3	56
4789.34	41393.47	y ⁵ F ^o	5	82	20519.60	a ⁵ G	6	12.4
4790.34	41393.47	y ⁵ F ^o	5	82	20523.94	a ⁵ G	5	0.88
4829.31	41224.78	y ⁵ F ^o	4	82	20523.69	a ⁵ G	4	1.22
4829.37	41224.78	y ⁵ F ^o	4	82	20523.94	a ⁵ G	5	9.8
4861.19	41086.26	y ⁵ F ^o	3	83	20520.92	a ⁵ G	3	1.43
4861.85	41086.26	y ⁵ F ^o	3	83	20523.69	a ⁵ G	4	7.7
4887.68	40971.29	y ⁵ F ^o	2	83	20517.40	a ⁵ G	2	0.48
4888.52	40971.29	y ⁵ F ^o	2	83	20520.92	a ⁵ G	3	2.4
4903.22	40906.46	y ⁵ F ^o	1	84	20517.40	a ⁵ G	2	7.7
5225.81	40971.29	y ⁵ F ^o	2	83	21840.84	a ⁵ P	3	1.54
5227.74	40971.29	y ⁵ F ^o	2	83	21847.88	a ⁵ P	2	0.43
5230.22	40971.29	y ⁵ F ^o	2	83	21856.94	a ⁵ P	1	0.92
6313.22	47228.80	x ⁵ G ^o	5	63	31393.40	a ⁵ F	5	0.25

Table 4.2 (cont'd)

λ_{air} [Å]	E_{upper} [cm ⁻¹]	Term	J_{upper}	Leading Percentage ^a	E_{lower} [cm ⁻¹]	Term	J_{lower}	A_{Exp} [10 ⁶ s ⁻¹]
6322.60	47189.87	x ⁵ G ^o	4	60	31377.96	a ⁵ F	4	0.3
9290.48	31280.35	z ⁵ F ^o	5	96	20519.60	a ⁵ G	6	0.29
9294.23	31280.35	z ⁵ F ^o	5	96	20523.94	a ⁵ G	5	0.03
9446.81	31106.37	z ⁵ F ^o	4	95	20523.69	a ⁵ G	4	0.05
9447.03	31106.37	z ⁵ F ^o	4	95	20523.94	a ⁵ G	5	0.29
9571.75	30965.46	z ⁵ F ^o	3	96	20520.92	a ⁵ G	3	0.05
9574.29	30965.46	z ⁵ F ^o	3	96	20523.69	a ⁵ G	4	0.24
9667.20	30858.82	z ⁵ F ^o	2	96	20517.40	a ⁵ G	2	0.05
9670.49	30858.82	z ⁵ F ^o	2	96	20520.92	a ⁵ G	3	0.23
9734.52	30787.30	z ⁵ F ^o	1	96	20517.40	a ⁵ G	2	0.27

^aThese leading percentage values are taken from the NIST web-site:http://physics.nist.gov/PhysRefData/ASD/levels_form.html

Chapter 5

Abundance Investigation of M15 Red Giant Branch and Horizontal Branch Stars

5.1 Introduction

The current work presents a new comparative abundance derivation for three RGB and six RHB stars of the globular cluster M15. Special effort is made to understand the apparent discrepancy in the metallicity of RGB and RHB stars. A detailed examination of the n-capture elements then ensues. Section 2 briefly details the spectroscopic observations, data reduction methods, and abundance analysis techniques. §3 introduces the issues that arise in the solution of the line transfer equation for metal-poor, low-temperature, evolved stars. §4 and §5 describe the alteration of the source function to include scattering and the corresponding solution of radiative transfer equation with the use of the Short Characteristics methodology. §6 shows

Table 5.1. M15 Stellar Model Atmospheric Parameters

Star	Evolutionary State	T_{eff} [K]	$\log g$	[M/H] [km/s]	v_t
K341	RGB	4320	0.25	-2.20	2.20
K462	RGB	4320	0.25	-2.20	2.15
K583	RGB	4310	0.20	-2.20	2.30
B009	RHB	5300	1.65	-2.50	2.60
B028	RHB	5750	2.40	-2.50	2.85
B224	RHB	5600	2.10	-2.50	2.70
B262	RHB	4950	1.30	-2.50	1.90
B412	RHB	6200	2.70	-2.50	3.30
B584	RHB	6000	2.70	-2.50	2.90

the outcome of these alterations. Abundance results are found in §7 together with a discussion of the chemical inhomogeneity of M15.

5.2 Observations and Abundance Analysis

The original acquisition of the M15 RGB spectra was done in 1997 (Snedden et al. 2000) with the High-Resolution Echelle Spectrograph at the Keck I telescope (Vogt et al. 1994). Also, the original observations of the M15 RHB stars (Preston et al. 2006) were obtained with the Magellan Iannori Kyocera Echelle spectrograph at the Clay 6.5 m telescope at Las Campanas Observatory (Bernstein et al. 2003). Resolution of the two data sets were comparable: $R_{RGB} \simeq 45,000$ and $R_{RHB} \simeq 40,000$. For all spectroscopic observations, the S/N range was $30 < S/N < 260$.

Photometry from both Buonanno et al. (1985) and the Two Micron All Sky Survey (2MASS) was used for the stars of M15. To determine initial T_{eff} and $\log g$ values (with the assumption of a stellar mass of $M = 0.8M_{\text{sun}}$), the color calibration

system of Ramirez & Melendez (2005) was employed. Fine adjustments of the model parameters (as well as the determination of v_t) were done to fulfill the condition that no derived abundance should demonstrate a trend with excitation potential, equivalent width, ionization stage, and wavelength. Models for the M15 RHB stars are based on the stellar parameters listed in the Preston et al. paper (2006). Fresh, independent determinations of model parameters were done for the M15 RGB stars facilitated by the use of a newly-modified MOOG line transfer code (the nature of the RGB stars, cool and metal-poor, necessitates these additional efforts; see §5.5 and §5.6). All of the stellar atmospheric models are generated from the Kurucz ATLAS grid and are 1-d plane-parallel in nature. Table 4.1 lists the adopted model atmospheric parameters for the stars of M15.

Efforts were made to employ the most up-to-date laboratory transition probability data. For equivalent width measurements, the SPECTRE code (Fitzpatrick & Sneden 1987) was used and for spectral synthesis determinations the MOOG program (Sneden 1973) was employed. For further details consult Preston et al. (2006).

5.3 Line Formation in Low Metallicity, Cool Giants

In the visible spectral range, the principal sources of opacity in stellar atmospheres include the bound-free absorption from the negative hydrogen ion (H^-) and Rayleigh scattering from neutral atomic hydrogen. A standard expression (e.g. Gray 1976) for the H^-_{BF} absorption coefficient is

$$\kappa \simeq 4.1458 \times 10^{-10} \alpha_{BF} P_e \Theta^{5/2} 10^{0.754\Theta} \quad (5.1)$$

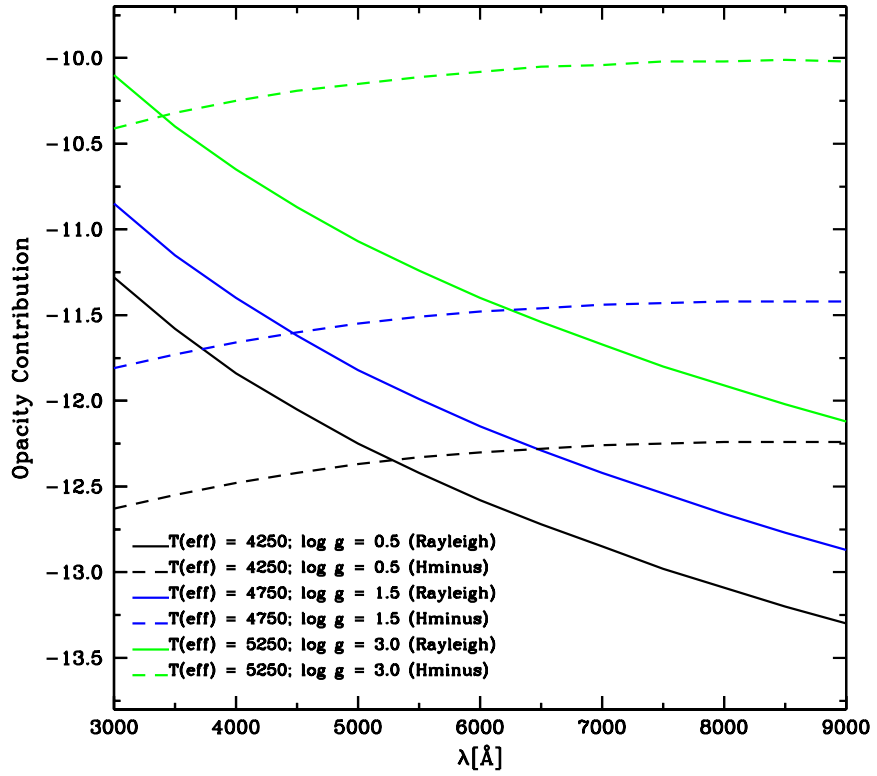


Figure 5.1 Opacity contribution as a function of wavelength for three different models. A typical layer of the atmosphere is chosen for this comparison and all stars have a metallicity of $[M/H] = -1.0$.

where α_{BF} is the bound-free atomic absorption coefficient (which has frequency dependence), P_e is the electron pressure, and $\Theta = 5040/T$ (note that Eq. 5.1 is per neutral hydrogen atom).

The scattering cross-section of radiation with angular frequency ω incident upon a neutral H atom is given by the Kramers-Heisenberg formula in terms of atomic units as

$$\frac{\sigma(\omega)}{\sigma_T} = \left(\frac{\omega}{\omega_1}\right)^4 \left| A_0 + A_2 \left(\frac{\omega}{\omega_1}\right)^2 + A_4 \left(\frac{\omega}{\omega_1}\right)^4 + \dots \right|^2 \quad (5.2)$$

where σ_T is the Thompson scattering cross-section, ω_1 is the angular frequency corresponding to the Lyman limit, and A_i are coefficients obtained via the Dalgarno-Lewis method (Lee 2005 and references therein). Numerical calculations of the A_i coefficients and the generation of an exact expression for Eq. 5.1 have been done by Dalgarno & Williams (1962) and more recently by Lee & Kim (2004).

The H^-_{BF} and Rayleigh scattering opacity contributions depend on temperature and metallicity (as well as on surface gravity). In addition due to its λ^{-4} dependence, Rayleigh scattering will mostly effect transitions in the ultraviolet and blue wavelength ranges. Consequently for the vast majority of stars (such as dwarfs and sub-giants), H^-_{BF} is the predominant opacity source (in the visible spectral region). Hence, many spectral line formation codes combine the contributions from Rayleigh scattering and H^-_{BF} , treat these contributions as pure absorption, and set the source function (essentially) equal to the Planck function.

However, Figure 5.1 shows for short wavelengths that the Rayleigh scattering contribution become comparable to (and even exceeds) that from H^-_{BF} for low temperature, low metallicity giants. In fact for the star of $T_{\text{eff}} = 4250$ and $\log g = 0.50$, this figure demonstrates that the opacity contribution from Rayleigh scattering

outstrips that from H^-_{BF} at wavelengths as red as $\lambda \approx 5000\text{\AA}$ (note that this star is similar in temperature and surface gravity to the RGB tip stars of M15).

Below a wavelength threshold of $\lambda \approx 4500\text{ \AA}$ Rayleigh scattering greatly affects the spectral transitions in these types of stellar environments. Consequently, abundances from bluer wavelength lines generally report higher than those from redder ones (e.g. Cayrel et al. 2004 and Johnson 2002). To accurately determine the line intensity with the correct amount of flux and opacity contribution, isotropic, coherent scattering must be taken into account (the Milne-Eddington Problem). Therefore, it was necessary to alter the MOOG code as it uses pure a absorption source function ($S = \epsilon B$) to incorporate a mean intensity (J) and a source function which sums both the absorption and scattering components ($S = \epsilon B + (1 - \epsilon)J$).¹ The nature and the extent of the alterations are conveyed in the next two sections.

5.4 The Difference Equation Approach to the Milne-Eddington Problem

The most basic geometric view of a stellar atmosphere is a planar slab divided into horizontally homogeneous layers. To describe radiative transport through such a medium, the radiative transfer equation (RTE) assumes the form

$$\mu \frac{dI}{d\tau} = I - S \tag{5.3}$$

where μ is the directional cosine, I is the specific intensity of radiation, τ is the optical depth and S is the source function. To commence with the formal solution

¹Changes were made to the publicly-available MOOG code (website: <http://verdi.as.utexas.edu/moog.html>). The next release of MOOG will contain all of the new modifications.

of the RTE, consider a ray which propagates through the planar slab. Then, the equations of transfer along the two directions of the ray are

$$\mu \frac{dI_-}{d\tau_-} = -I_- + S_- \quad (5.4)$$

$$\mu \frac{dI_+}{d\tau_+} = I_+ - S_+ \quad (5.5)$$

In order to derive the second-order form of the transfer equation, the Feautrier algorithm (1964) is used to introduce the variables

$$j = \frac{1}{2}(I_+ + I_-)$$

$$h = \frac{1}{2}(I_+ - I_-)$$

Since both the source function and the optical depth are even functions (with respect to angle), the two equations above may be then manipulated to obtain

$$\mu \frac{dj}{d\tau} = h \quad (5.6)$$

$$\mu \frac{dh}{d\tau} = j - S \quad (5.7)$$

Then, Eq. 5.6 may be used to eliminate h from Eq. 5.7 to arrive at the desired second-order form

$$\mu^2 \frac{d^2 j}{d\tau^2} = j - S \quad (5.8)$$

with boundary conditions $I_- = 0$ for the incoming intensity and via the diffusion approximation, $I_+ = B(\tau_{max}) + \mu(\partial B/\partial\tau)_{\tau_{max}}$ for the outgoing intensity.

Eq. 5.8 is an integro-differential equation. To obtain the numerical solution of Eq. 5.8, a discretization in angle and optical depth is necessary. As a consequence, the solution is simplified and a quadrature summation is done instead of an integration.

The fundamental assumption of the formal solution is that the source function is specified completely in terms optical depth. For the Milne-Eddington problem, the source function is written as

$$S = (1 - \epsilon)J + \epsilon B \quad (5.9)$$

where J is the mean intensity (specifically, it is equal to the average of I over the solid angle) and B is the Planck function. In essence, the solution of the RTE involves the approximation of J as follows:

$$J = \int_0^1 j(\mu)d\mu \simeq \sum w_k j_k \quad (5.10)$$

where w_k are the quadrature weights of the angle integration. To achieve sufficient angular accuracy, at least three Gaussian quadrature points are required on the interval $(0, 1)$. Though it is possible to evaluate Eq. 5.9 (and accordingly, Eq. 5.10) in a single step, the use of an iterative technique to arrive at a solution is preferred as it is computationally faster (than a straightforward approach). Example of efficient iterative methods include the Accelerated Lambda Iteration (ALI) techniques (employed here, see Appendix A).

5.5 Short Characteristic Solution of Line Transfer

Radiative transfer may be thought of as the propagation of photons downstream along a ray on a two-dimensional Cartesian grid (the number of rays corresponds to the number of quadrature angles). Determination of radiation along a ray is done periodically at ray segments, or short characteristics. Original development of the short characteristics (SC) methodology (in the context of radiative transfer) was done by Mihalas, Auer, & Mihalas (1978). Improvement of the SC approach in the explicit specification of the source function (at all grid points) was made by Kunasz & Auer (1988). The treatment of Auer & Paletou (1994) is followed here.

Essentially, SC start at a grid point and proceed in the upwind direction until a cell boundary is met. Then, at these cell boundaries (the upstream points) the intensity must be known. As shown in Figure 5.2², the ray moves downward from the upper to lower right direction. With the knowledge of the cell boundary intensities, the intensity at points further downstream can be calculated. At the grid point 0 of Figure 5.2, the intensity is determined by integrating from 1 to 0 across the cell. The intensity at point 0 is expressed as

$$I_0 = I_1 e^{-\Delta\tau_1} + \int_0^{\delta\tau_1} S(\tau) e^{-\tau} d\tau \quad (5.11)$$

The optical depth step $\Delta\tau_1$ can be thought of as the path integral of the opacity, k , along 1 to 0 (remember that at all grid points, k and S are known). The evaluation of Eq. 5.11 requires the interpolation of the source function at points 1 and 2 (as they do not lie at grid points). To satisfy the diffusion approximation, a quadratic interpolation must be used in the integration of Eq. 5.11. Interpolation

²This figure depicts a two-dimensional scenario. Note that a simpler, one-dimensional methodology may also be employed as done in the subroutine of Appendix A.

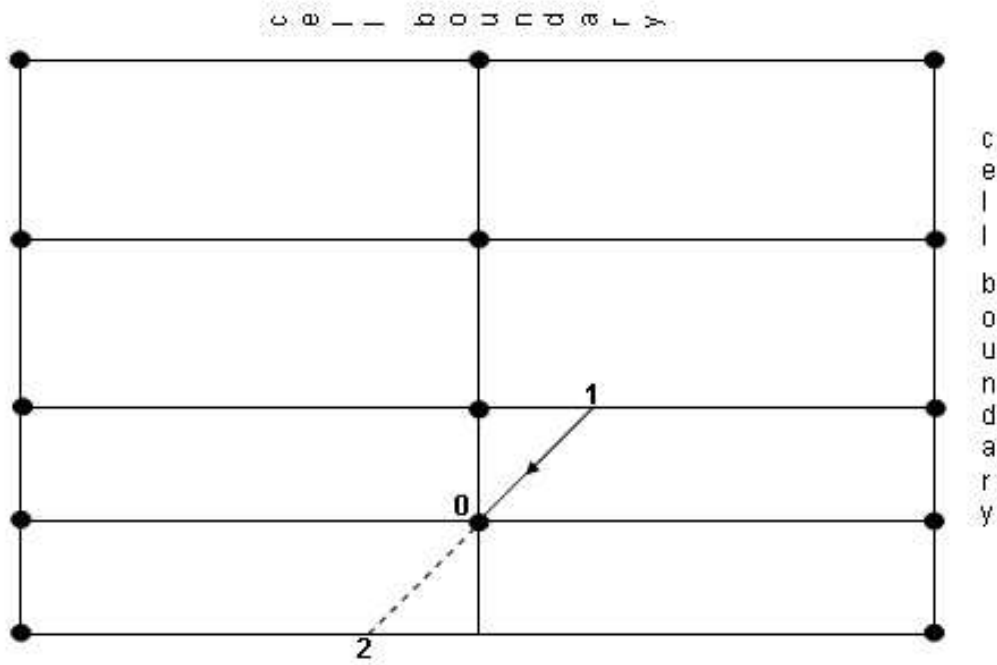


Figure 5.2 Ray propagating on a two-dimensional Cartesian grid.

over (S_2, S_1, S_0) with $S(\tau) = S_0 + c_1\tau + c_1\tau^2$, entails

$$\int_0^{\Delta\tau_1} S(\tau)e^{-\tau} d\tau = S_0w_0 + c_1w_1 + c_2w_2 \quad (5.12)$$

The coefficients of Eq. 5.12 are expressed in terms of the differences of the source functions

$$d_1 = (S_0 - S_1)/\Delta\tau_1 \quad (5.13)$$

$$d_2 = (S_2 - S_0)/\Delta\tau_2 \quad (5.14)$$

$$c_1 = (d_2\Delta\tau_1 + d_1\Delta\tau_2)/(\Delta\tau_1 + \Delta\tau_2) \quad (5.15)$$

$$c_2 = (d_2 - d_1)/(\Delta\tau_1 + \Delta\tau_2) \quad (5.16)$$

with the weights

$$\begin{aligned}
 w_0 &= 1 - e^{\Delta\tau_1} \\
 w_1 &= w_0 - \Delta\tau_1 e^{\Delta\tau_1} \\
 w_2 &= w_1 - \Delta\tau_1^2 e^{\Delta\tau_1}
 \end{aligned}$$

As the above definitions imply, the weights may be found by recursion. At the boundary, linear interpolation takes place with $c_1 = d_1$ and $c_2 = 0$. The use of linear interpolation does not generate significant error (as normally would occur) due to the optically-thin nature of the boundary layer.

In consideration of the entire grid, it is necessary to sum over all directions with the d values of Eq. 5.13 and Eq. 5.14 defined by setting $S_0 = 1$ and taking the other S to be 0. Then, the SC formal solution of the transfer equation can proceed in an iterative manner. Appendix A contains the additional code for the MOOG program which incorporates the short characteristics methodology.

5.6 Elimination of Abundance with Wavelength Trend

The improved code was first employed to re-determine the atmospheric parameters of M15 RGB stars. Figure 5.3 demonstrates the efficacy of the MOOG code modifications. Displayed in this figure are the Fe I abundances as a function of wavelength for the RGB star K341 ($T_{\text{eff}} = 4320$ and $\log g = 0.25$). In the upper panel and middle panels of Figure 5.3, a least-squares fit to observed data (trendline) is shown. This trendline clearly indicates the degree to which the blue transitions bias the abundance results toward erroneously high values. As shown, my development of a

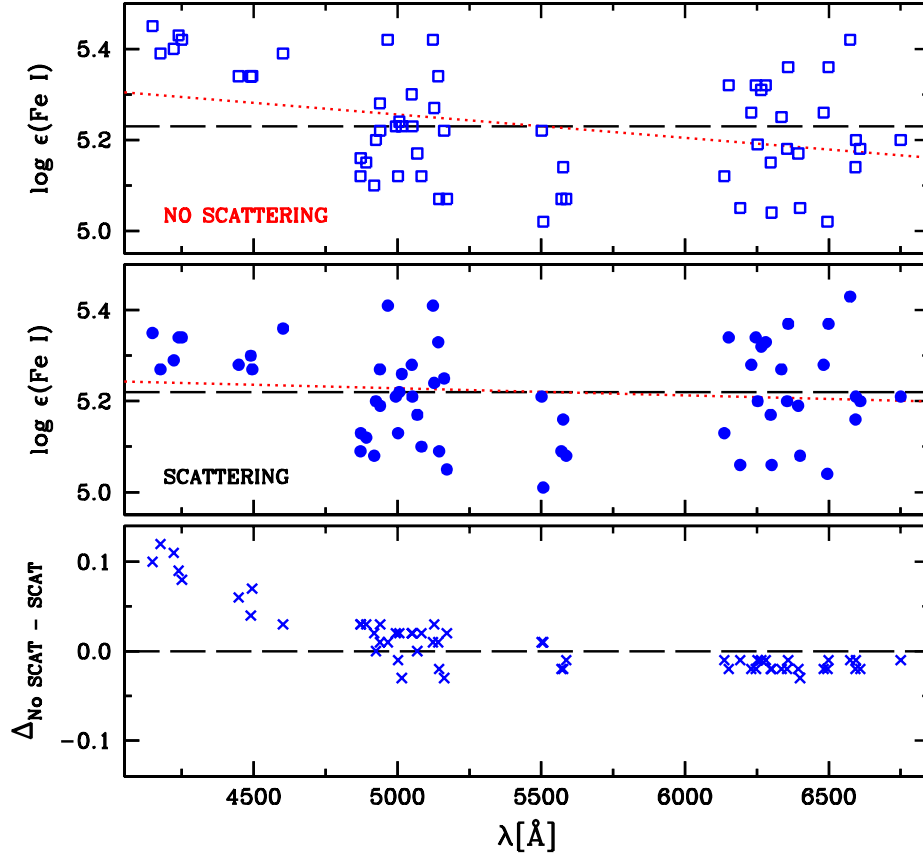


Figure 5.3 Plot of the Fe I abundance as a function of wavelength for the RGB tip star K341 (model atmosphere parameters: $T_{\text{eff}} = 4320$ K; $\log g = 0.25$; $[\text{Fe}/\text{H}] = -2.2$).

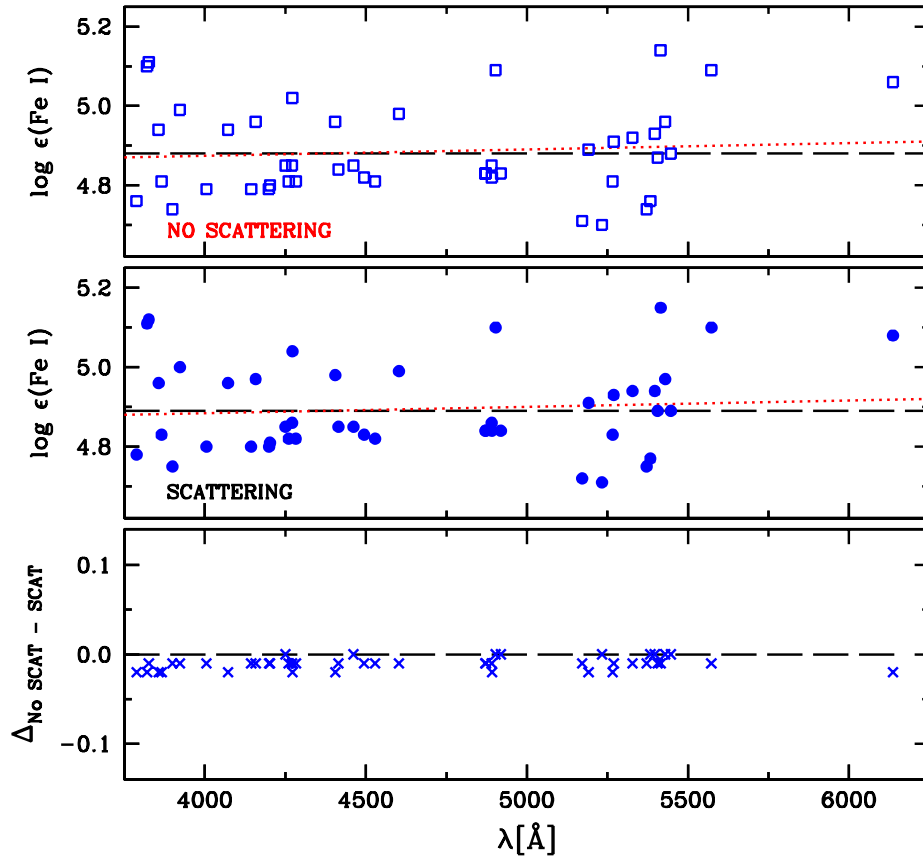


Figure 5.4 Plot of the Fe I abundance as a function of wavelength for the RHB star B412 (model atmosphere parameters: $T_{\text{eff}} = 6200$ K; $\log g = 2.70$; $[\text{Fe}/\text{H}] = -2.5$).

code which employs a more advanced radiative transfer approximation largely reduces the abundance trend with wavelength (upper versus middle panel). Also as expected, only the blue lines are substantially affected.

Figure 5.4 is similar to Figure 5.3 except that Fe I abundances of the RHB star B412 ($T_{\text{eff}}=6200$ and $\log g=2.70$) are considered. No effect in the abundances is seen with the use of the new MOOG program. This is in line with expectations as B412 is a warmer, more dense star (and the H^-_{BF} opacity contribution becomes large due to the increased electron pressure).

5.7 Presentation of Results and Discussion

Table 5.2 lists the element abundances for the 9 stars of the current M15 study. It also contains the associated standard deviation values. Mean iron abundances may be obtained from Table 4.2 for both sets of M15 stars: $\langle [Fe_I/H] \rangle_{RGB} = 5.16$ ($\sigma = 0.07$) and $\langle [Fe_{II}/H] \rangle_{RGB} = 5.15$ ($\sigma = 0.07$); and $\langle [Fe_I/H] \rangle_{RHB} = 4.82$ ($\sigma = 0.06$) and $\langle [Fe_{II}/H] \rangle_{RHB} = 4.87$ ($\sigma = 0.05$). The difference between the iron abundance of the RGB and RHB stars is approximately 0.30 dex and does not fall within the quadrature addition of the errors (0.09 dex). The employment of the new MOOG code did not affect the *average* RGB iron abundances ($\Delta_{OLD-NEW} = 0.01$ for Fe I and $\Delta_{OLD-NEW} = -0.03$ for Fe II). The substantial disagreement between the RGB and RHB stars is not understood at this time. Note that the two sets of data were taken on different instruments (though there is no evidence to suggest that one data set is more reliable than the other).

Figure 5.5 presents titanium and calcium abundances as a function of metallicity for the stars of M15. As shown, $[Ti_{II}/Fe_{II}]$ is virtually the same in both data sets. For the RHB stars, $[Ti_I]$ and $[Ti_{II}]$ tend toward agreement whereas in the

Table 5.2. Neutron Capture Abundance Values for the M15 Stars

Species	Sun	K341	K462	K583	B009	B028	B224	B262	B412	B584
Ca I	6.36	-1.99	-2.12	-2.13	-2.21	-2.23	-2.25	-2.25	-2.16	-2.17
σ	...	0.10	0.09	0.08	0.11	0.12	0.11	0.12	0.11	0.16
Sc II	3.10	-2.22	-2.36	-2.37	-2.22	-2.33	-2.26	-2.50	-2.16	-2.21
σ	...	0.12	0.16	0.12	0.13	0.11	0.10	0.05	0.20	0.00
Ti I	4.99	-2.22	-2.20	-2.37	-2.15	-2.37	-2.25	-2.47	-1.82	-1.92
σ	...	0.13	0.11	0.14	0.16	0.13	0.14	0.12	0.09	0.15
Ti II	4.99	-1.84	-1.91	-2.00	-2.32	-2.39	-2.30	-2.43	-2.10	-2.15
σ	...	0.11	0.14	0.11	0.08	0.08	0.13	0.06	0.05	0.06
Cr I	5.67	-2.58	-2.50	-2.68	-2.89	-2.97	-3.02	-3.01	-2.74	-2.89
σ	...	0.05	0.09	0.06	0.15	0.11	0.14	0.21	0.10	0.07
Cr II	5.67	-2.27	-2.21	-2.30	-2.49	-2.35	-2.45	-2.67	-2.25	-2.30
σ	...	0.20	0.24	0.10	0.19	0.07	0.00	0.08	0.02	0.15
Fe I	7.52	-2.30	-2.34	-2.44	-2.70	-2.74	-2.77	-2.74	-2.64	-2.64
σ	...	0.11	0.12	0.11	0.11	0.11	0.11	0.12	0.11	0.16
Fe II	7.52	-2.33	-2.34	-2.45	-2.66	-2.69	-2.68	-2.71	-2.59	-2.61
σ	...	0.07	0.13	0.11	0.09	0.11	0.13	0.15	0.07	0.12
Ba II	2.13	-2.00	-1.87	-2.46	-2.26	-2.53	-2.48	-2.41	-2.40	-2.54
σ	...	0.29	0.40	0.17	0.08	0.20	0.12	0.09	0.15	0.23
La II	1.22	-2.07	-1.83	-2.34	-2.15	...	-2.17	-2.42	...	-2.08
σ	...	0.08	0.07	0.06	0.07	...	0.10	0.09	...	0.14
Ce II	1.55	-2.02	-1.88	-2.45	-2.14	-2.28
σ	...	0.17	0.12	0.11	0.05	0.08
Nd II	1.50	-1.89	-1.73	-1.84	-2.13	-2.21
σ	...	0.14	0.08	0.09	0.10	0.16
Eu II	0.51	-1.44	-1.26	-1.79	-1.75	-2.08	-1.80	-2.04	-1.48	-1.71
σ	...	0.09	0.12	0.11	0.03	0.07	0.09	0.06	0.15	0.15

RGB stars, the two abundance values contrast starkly. The three RGB stars report a consistent Ca I abundance. Similarly, there is no variation of the Ca I abundance seen in the six RHB stars. However, $[Ca_I/Fe_I]$ differs greatly between the RGB and RHB stars. A possible explanation for these departures is the overionization of the RGB stars. If $J > B$ in the atmospheric region where bound-free transitions occur, then the rates of photoionization will surpass the LTE prediction (Asplund 2005b). For species which exist in their minority ionization state, this overionization can cause a significant alteration of the line opacity and considerably weaken the lines. In stars such as the M15 giants, the most susceptible transitions are those in the UV where B decreases much faster with atmospheric height than J (which becomes roughly constant once the wavelength becomes optically thin; Asplund 2005b).

Figures 5.6, 5.7, and 5.8 establish abundance trends for the n-capture elements. Again, a clear distinction is seen in Figure 5.6 between the RGB and RHB stars. Figure 5.7 shows some star-to-star abundance scatter in the RGB with the data from K583 being the most disparate. Notwithstanding the appreciable Ba scatter, a positive correlation of both Ba and La with Eu is shown in Figure 5.8. The upper right panel with $[Ba_{II}/Eu_{II}]$ as a function of $[Eu_{II}/Fe_{II}]$ appears to indicate that there are no differences between the two data sets (though again, note that the Ba scatter is sizable). Alternatively, the lower right panel seems to suggest that $[La_{II}/Eu_{II}]$ as a function of $[Eu_{II}/Fe_{II}]$ is lower in RGB stars than in RHB stars. The abundances from the Otsuki et al. (2006) survey of M15 stars have been added to this plot. Though they did not distinguish between evolutionary stages, the Otsuki et al. data seem to confirm that from the current study.

Figure 5.9 displays $\log\epsilon(X)$ abundances as a function of atomic number for select n-capture elements. One average abundance from all RGB stars and one

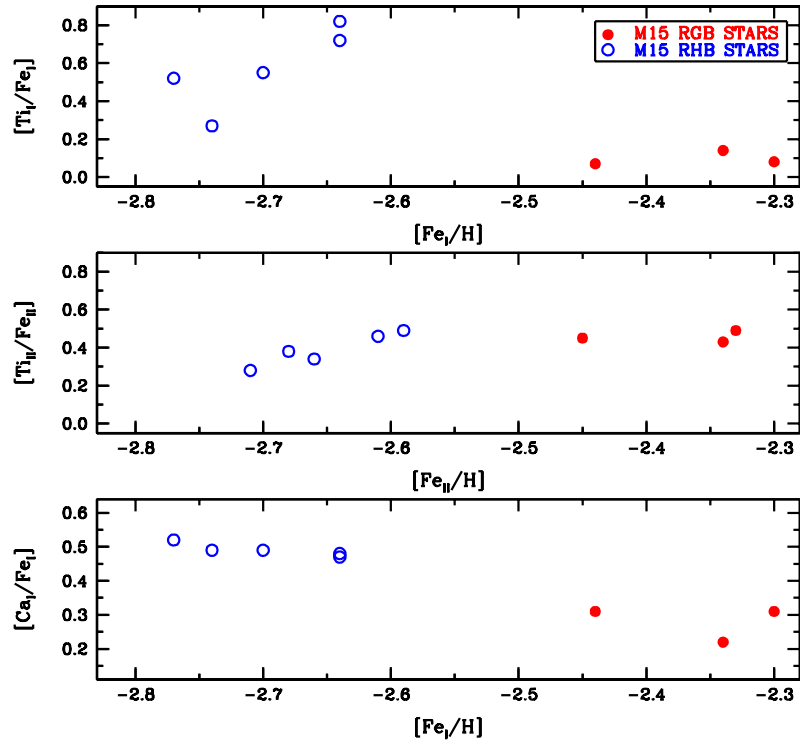


Figure 5.5 Plot of light element abundances as a function of metallicity for the M15 RGB stars (red, filled circles) and RHB stars (blue, open circles).

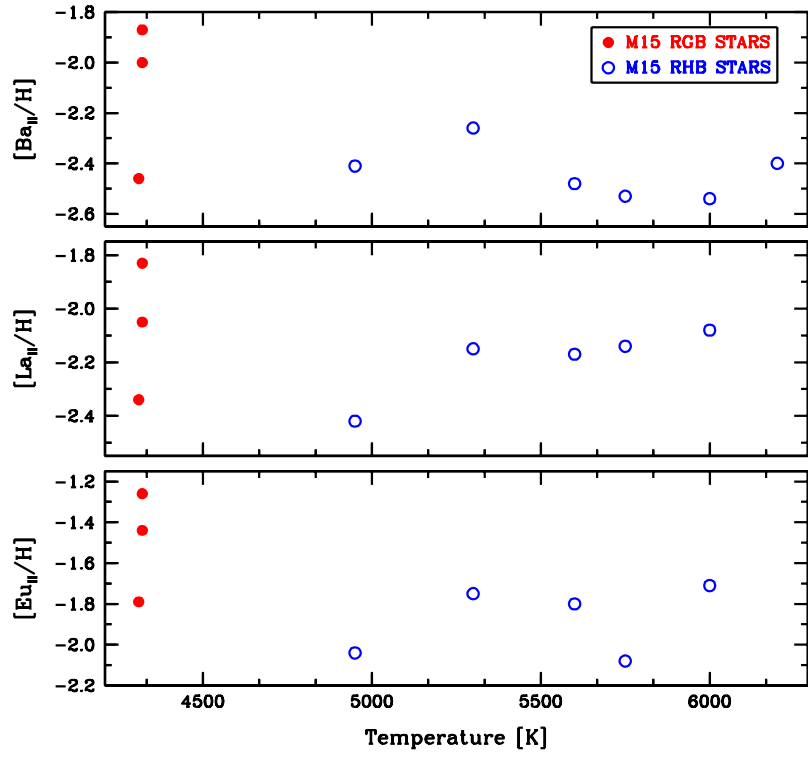


Figure 5.6 Plot of n-capture element abundances as a function of temperature for the M15 RGB stars (red, filled circles) and RHB stars (blue, open circles).

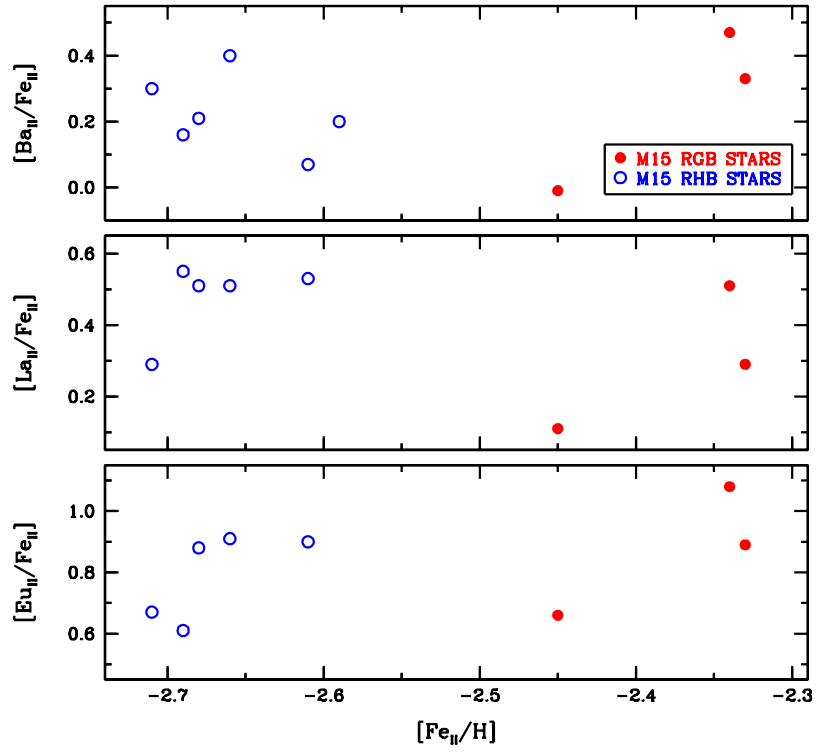


Figure 5.7 Plot of n-capture relative abundances as a function of metallicity for the M15 RGB stars (red, filled circles) and RHB stars (blue, open circles).

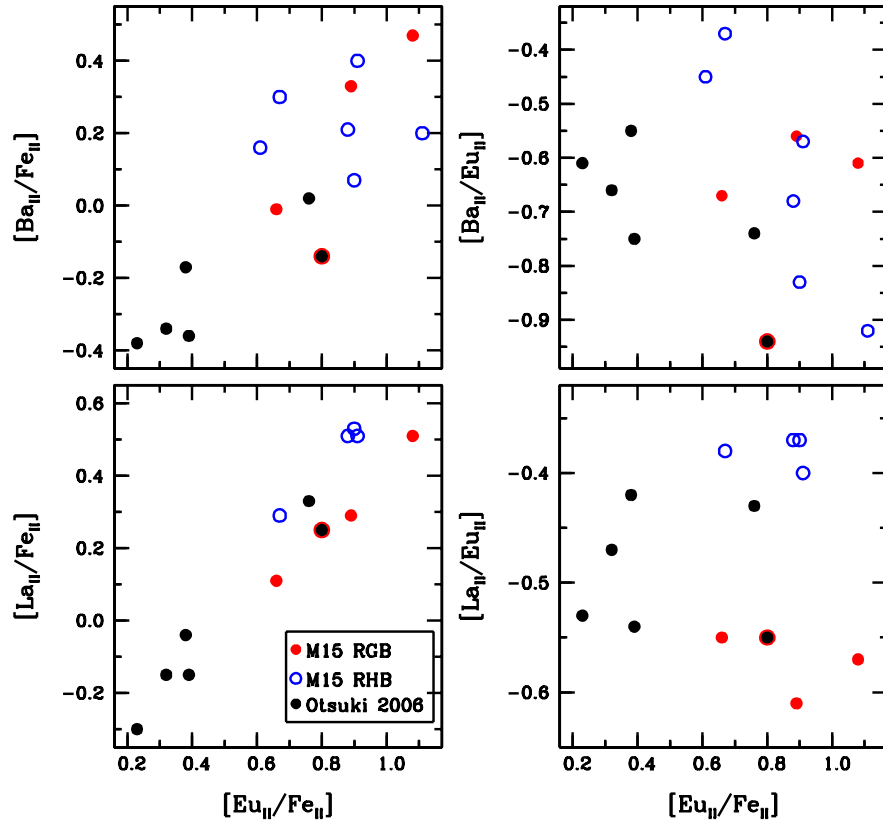


Figure 5.8 Abundance variation in the n-capture elements. The plot also includes the Otsuki et al. 2006 M15 RGB abundances. The one star that the Otsuki et al. and the present study have in common is indicated as a black dot encircled in red.

average abundance from all RHB stars is reported per element. In this figure, the scaled solar r- and s-process predictions from Simmerer et al. 2004 are plotted. Figure 5.9 also includes abundance data from the r-process rich, metal-poor red giant HD 221170 (Ivans et al. 2006). Note that the r-process prediction as well as the average abundances from HD 221170 and the RHB stars have been normalized to the $\langle \log\epsilon(Nd_{II}) \rangle$ value of the RGB stars.

To first approximation, $\langle \log\epsilon(Ba_{II}/Nd_{II}) \rangle$ and $\langle \log\epsilon(Eu_{II}/Nd_{II}) \rangle$ agree in RGB stars, HD 221170, and RHB stars. The slightly high $\langle \log\epsilon(La_{II}/Nd_{II}) \rangle$ values of the RHB stars and HD 221170 still fall within the error. Yet, $\langle \log\epsilon(Ce_{II}/Nd_{II}) \rangle$ is largely aberrant for both HD 221170 and the RHB stars. In general, the M15 abundance data match the predicted scaled solar r-process values (which is suggestive of r-process enhancement). Prior to the completion of the current work, determination of the other n-capture abundances will occur (from elements such as Sr, Y, and Zr in order to establish the entire abundance trend). For the verification of these results, additional spectra should be taken of M15 RGB and RHB stars with the same telescope-detector configuration.

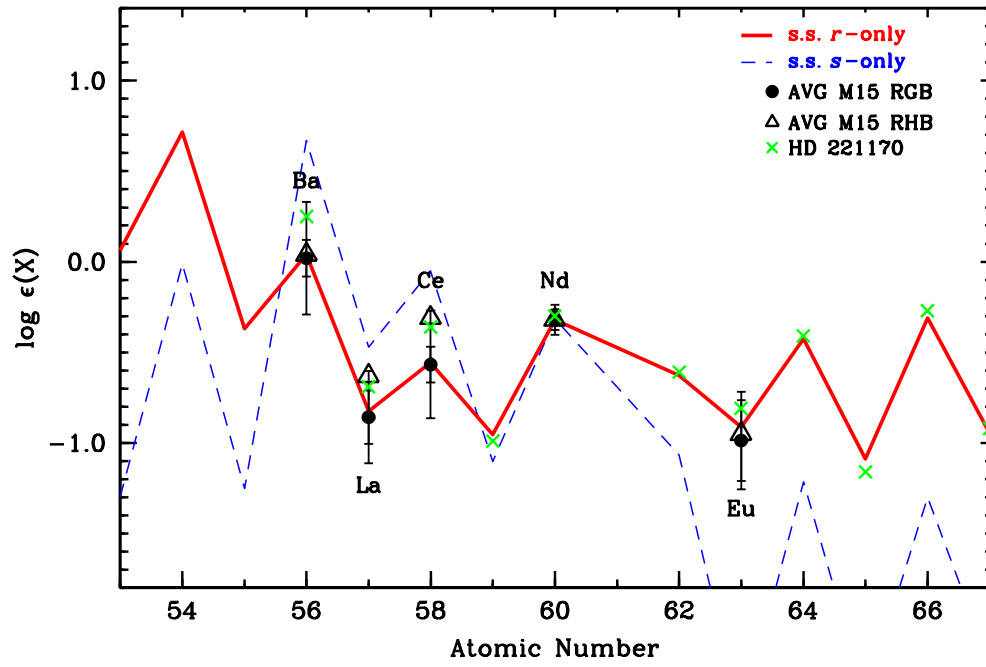


Figure 5.9 Abundance as a function of atomic number for a few n-capture elements. All values are normalized to the average Nd abundance of the M15 RGB stars. The plot also includes the HD 221170 abundances from Ivans et al. (2006).

Chapter 6

Conclusions and Future Study

This dissertation is a compilation of four projects that address aspects of abundance derivation (and its implications).

In the current work, the Mn abundance trend with metallicity has been established for hundreds of globular cluster, open cluster, and halo field stars. Globular cluster stars display a mean relative abundance of $\langle [Mn/Fe] \rangle = -0.37 \pm 0.01$ ($\sigma = 0.10$) in the range $-0.7 > [Fe/H] > -2.7$; almost the same as that of halo field stars, $\langle [Mn/Fe] \rangle = -0.36 \pm 0.01$ ($\sigma = 0.08$). No statistically significant difference exists between the Mn abundance of halo globular cluster and field stars.

The calculation of oscillator strengths for 263 lines of Cr I has been done with the combination of FTS branching fraction measurements and published radiative lifetime determinations. With this new set of transition probabilities, the solar photospheric abundance of Cr I, $\log \epsilon = 5.64 \pm 0.01$ ($\sigma = 0.07$), has been found from 58 lines. The Cr I abundance was also determined in three other stars (varying in metallicity and evolutionary state): HD 140283, CS 22892-052, and HD 75732. With the aid of Cr II oscillator strength data from the FERRUM project, the Cr II

abundance was also examined. In none of the aforementioned stars was chromium ionization equilibrium achieved with the use of plane-parallel models and LTE line formation codes. Cr I transitions were consistently underabundant with respect to Cr II Lines for all targets. Neither internal error sources nor external ones can account for the difference.

With the utilization of LS Coupling, a simple Fortran routine has been constructed to compute semi-empirical transition probability values. Employing this code, the calculated gf values and those from experiment agree well with one another (note that these are initial efforts). For those lines that possess experimental values only for radiative lifetimes (and lack branching fraction information), then these semi-empirical oscillator strengths represent a good approximation.

In the present study, an abundance analysis has been performed for six RHB stars and three RGB stars of the M15 globular cluster. A disparity in the $[Fe/H]$ values between the RGB and RHB stars was detected. The $\Delta(\langle [Fe/H] \rangle_{RGB-RHB}) \approx 0.2$ dex discrepancy is stubborn as no apparent cause for the departure between the two values has yet been found. There is good overall agreement between the derived n-capture abundances for the RHB stars and the scaled solar r-process predictions. This alludes to a r-process enrichment scenario for M15 (with minimal s-process contribution).

Completion of the M15 abundance survey (by determination of remaining light and n-capture element abundances) as well as the continuation of the semi-empirical calculation of Cr I transition probabilities are near term goals. Many courses of future work are available which include laboratory efforts to determine the oscillator strengths of the neutral species of titanium and manganese and an abundance investigation of the RGB and RHB stars of the globular cluster M68

(observations are currently underway). One potential impact of the iron-peak gf study is the further characterization of nLTE processes in stars. The M68 globular cluster abundance analysis will particularly examine the metallicity issue and discern the $[Fe/H]$ trend in stars of varying evolutionary states.

Appendix A

Short Characteristics Subroutine for the MOOG Program

A.1 Introduction

The section below contains code only for the subroutine Shortcharac.f. The alteration or addition of a few other subroutines to the MOOG program was necessary in order to accommodate Shortcharac.f. These routines include: Cdcalc.f, Fluxint.f, Gausi.f, Inmodel.f, and Scat.com. More extensive documentation may be found in the release of the latest version of MOOG found on the website: <http://verdi.as.utexas.edu/moog.html>.

A.2 Shortcharac.f Subroutine

```
SUBROUTINE Shortcharac
```

```
implicit real*8 (a-h,o-z)
```

```
include 'Chars.com'
```

```
include 'Atmos.com'
```

```
include 'Linex.com'
```

```
include 'Feautr.com'
```

```
include 'Scat.com'
```

```
integer IT
```

```
data IVERB /2/
```

```
C*** Local Arrays
```

```
real*8 THOMSON (75), PLANCK(75)
```

```
real*8 DDM(75), DTAU1(75), ALO(75), XJ_OLD(75)
```

```
real*8 ETA(75), OOD(75), ETAT(75), OPASCAT(75)
```

```
real*8 XJ(75), DDMM(75), DTAU1MI(75), OPA_THERM(75)
```

```
real*8 DTAU(75), WOP(75), W1(75), W0(75)
```

```
C*** Globally-defined quantities in MOOG format:
```

```
C slamMOOG(i), xjMOOG(i), fluxMOOG
```

```
C*** Convergence Loop Criteria (Relaxation of standards)
```

```
C*** Originally: eps_jcont = 1.e-5 and maxit_jcont = 10
```

```
EPS_JCONT = 2.E-3
```

```
MAXIT_JCONT = 50
```

```
C*** Prepare rhox for MODELS that do not contain these values.  
C*** An additional conatnst might be necessary as kappa unit vary
```

```
do i=1, ntau  
    if (modtype .eq. 'KURTYPE' .or.  
>    modtype .eq. 'KURUCZ') CYCLE  
    rhox(i) = (tauref(i)/(kapref(i)/rho(i)))  
enddo
```

```
C*** Prepare DTAU1 (delta(tau))
```

```
do i=1, ntau  
    OOD(i) = kaplam(i) / rho(i)  
    IF (i .EQ. 1) CYCLE  
    DDM(i) = 0.5 * abs((rhox(i) - rhox(i-1)))  
    DTAU1(i) = DDM(i) * (OOD(i-1) + OOD(i))  
    IF (i .EQ. ntau) CYCLE  
    DDMM(i) = 0.25 * (rhox(i+1) - rhox(i-1))  
    DTAU1MI(i) = 1. / (DDMM(i) * (OOD(i-1) + OOD(i+1)))  
enddo
```

```
C*** Prepare THOMSON
```

```
do i=1, ntau  
    THOMSON(i) = kaplamsca(i)/kaplam(i)  
enddo
```

```

C*** Setup Approximate Lambda Operator
C*** GAMMA controls the amount of acceleration
C***     = 0 : No Acceleration
C***     = 1 : Full Acceleration
C***     > 1 : Acceleration with dampening

      GAMMA = 1.
      IF (GAMMA .EQ. 0.) THEN
        do i=1, ntau
          ALO(i) = 1.
        enddo
      ELSE
        DO i=1, ntau
          IF (i .EQ. 1) THEN
            DTAU_ALO      = DTAU1(2)
          ELSE IF (i .EQ. ntau) THEN
C*** Extra Dampening for the inner boundary
            DTAU_ALO      = 0.5 * DTAU1(ntau)
          ELSE
            DTAU_ALO      = 0.5 * (DTAU1(i) + DTAU1(i+1))
          ENDIF
        END
C*** Dampening by 2. * Gamma
C*** Sum (Integral) of 1/mu * dmU = Sum of mu * dmU = 0.5
c      DTAU_ALO          = DTAU_ALO * 1. /

```

```

        DTAU_ALO          = DTAU_ALO * THOMSON(i) /
>          (2. * GAMMA)

C*** Lambda Operator with THOMSON factor applied
        EXP_DTAU_ALO = EXP(-DTAU_ALO)
        IF (EXP_DTAU_ALO .NE. 1.) THEN
            ALO(i) = DTAU_ALO / (1. - EXP(-DTAU_ALO))
        ELSE
            ALO(i) = 1.
        ENDIF
    ENDDO
ENDIF

C*** Prepare tau scale and possible verbose output
        IF (IVERB .GE. 1) THEN
c          WRITE (0,*) 'i tau_rte(i) thomson(i) dtau1(i)'
            tau_rte(1) = 0.
            DO i=2, ntau
                tau_rte(i) = tau_rte(i-1) + DTAU1(i)
c          WRITE (0,'(I4,1p7e10.2)') i,tau_rte(i),thomson(i),
c          >          dtau1(i)
            ENDDO
            tau_rte(1) = tau_rte(2) / 10.
        ENDIF

```

```
C*** Prepare OPASCAT and OPA_THERM (opacities)
```

```
do i=1, ntau
```

```
    OPASCAT(i) = kaplam(i) * THOMSON(i)
```

```
    OPA_THERM(i) = kaplam(i) - OPASCAT(i)
```

```
enddo
```

```
C*** Emissivity from Planck Function and Preparation of Inner Boundary
```

```
C1 = 1.43878858E08
```

```
C2 = 3.972610376E08
```

```
HNUEK = C1 / wave
```

```
HNUEKCORE = HNUEK / t(ntau)
```

```
BCORE = C2 / ((EXP(HNUEKCORE)-1.) * wave * wave * wave)
```

```
HNUEKCORE1 = HNUEK / t(ntau-1)
```

```
BCORE1 = C2 / ((EXP(HNUEKCORE1)-1.) * wave * wave * wave)
```

```
DBCORE = BCORE-BCORE1
```

```
DO i=1, ntau
```

```
    HNUEKT = HNUEK / t(i)
```

```
    PLANCK(i) = C2 / ((EXP(HNUEKT)-1.) * wave * wave * wave)
```

```
    XJ_OLD(i) = PLANCK(i)
```

```
    ETA(i) = PLANCK(i) * OPA_THERM(i)
```

```

    ETAT(i)  = OPASCAT(i) * XJ_OLD(i)
    slam(i)  = (ETA(i) + ETAT(i)) / kaplam(i)
ENDDO

C*** Iteration loop
IT  = 0
DO
    IT = IT + 1
    do i=1,ntau
        XJ_OLD(i) = XJ(i)
        XJ(i)      = 0.
        slam(i)   = (ETA(i) + ETAT(i)) / kaplam(i)
    enddo

C*** Angle loop
    FLUXsc = 0.
    DO j=1, mmu

C*** Use 1st-order short-characteristics
C*** No incident radiation
    XI = 0.

C*** Second Depth Loop : Integration inwards
    DO i=2, ntau
        DTAU(i) = DTAU1(i) / mu(j)
        EXP_TAU = dexp(-DTAU(i))
    
```



```

        WOP(i) = (EXPTAU - 1.) / DTAU(i)
        W0(i)  = 1. + WOP(i)
        W1(i)  = -EXPTAU - WOP(i)
        XI     = XI * EXPTAU + W0(i) * slam(i) + W1(i) * slam(i-1)
        XJ(i)  = XJ(i) + 0.5 * wtmu(j) * XI

C*** End of second Depth Loop
        ENDDO

C*** Prepare Inner Boundary, multiplied by 2/dtau
        XI = 0.5 * wtmu(j) * (BCORE + (DBCORE * mu(j) / DTAU1(ntau)))

C*** Inner Boundary Condition
        XJ(ntau) = XJ(ntau) + XI

C*** Third Depth Loop : Integration outwards
        DO i=ntau-1, 1, -1
            DTAU(i) = DTAU1(i+1) / mu(j)
            EXPTAU  = dexp(-DTAU(i))
            WOP(i)  = (EXPTAU - 1.) / DTAU(i)
            W0(i)   = 1. + WOP(i)
            W1(i)   = -EXPTAU - WOP(i)
            XI      = XI * EXPTAU + W0(i) * slam(i) + W1(i) * slam(i+1)
            XJ(i)   = XJ(i) + 0.5 * wtmu(j) * XI
        ENDDO

C*** End of third Depth Loop
        ENDDO

```

```

C*** Flux (not in MOOG terms)
      FLUXsc = FLUXsc + XI * 0.5 * wtmu(j) * mu(j)

C*** End of Angle Loop
      ENDDO

C*** Calculate New ETAT and Exit Iteration Loop :: ALI applied!
      QMAX = 0.
      iMAX = 0.

      DO i=1, ntau
C*** Original ETAT_NEW and DELTA-ETAT
          ETAT_NEW = OPASCAT(i) * XJ(i)
          DE      = ETAT_NEW - ETAT(i)

C*** Accelerated DELTA-ETAT and improved ETAT_NEW
          DE      = DE * ALO(i)
          ETAT_NEW = ETAT(i) + DE
          QNA     = (ETAT_NEW - ETAT(i)) / ETAT_NEW
          Q       = ABS(ETAT_NEW - ETAT(i)) / ETAT_NEW
          IF (Q .GT. QMAX) THEN
              QMAX = Q
              QMAXNA = QNA
              iMAX = i
          
```

```

        ENDIF

        ETAT(i) = ETAT_NEW

    ENDDO

C*** Uncomment below if necessary. Progress monitor.
c      IF (IVERB .GE. 2) THEN
c          WRITE (0,'(A,I3,1x,F17.9,1x,F17.9,1x,I3,1x,I3)')
c      >      'CALC_JCONT1S : Iter, Qmax= ', IT, QMAX, QMAXNA, iMAX, i
c      ENDIF

IF (QMAX .LE. EPS_JCONT .OR. MAXIT_JCONT .EQ. 1) EXIT

IF (IT .GE. MAXIT_JCONT) THEN
    WRITE (0,'(A,F12.5,1X,1p7e10.2,1X,I3,1X,I3)')
    >      'CALC_JCONT1S :: ETAT Iteration exceeded : wave, QMAX= ',
    >      wave, QMAX, iMAX, ntau

    EXIT

ENDIF

C*** Final verbose output. If necessary, uncomment the verbose output below
c      IF (IVERB .GE. 1) THEN
c          WRITE (*,'(A,I3)') '* Iteration = ', IT
c          WRITE (*,'(A)') 'N=? tau_rte XJ Slam'
c          do i=1,ntau
c              WRITE (*,'(i2, 1p7e10.3)') i, tau_rte(i), XJ(i), slam(i)

```

```

c          enddo
c          WRITE (*,'(A)') 'FINISH'
c          ENDIF

C*** End of iteration loop
        ENDDO

C*** Write to file various quantities
        write (nwrite,1002) int(wave), it, qmax
1002  format (//'MEAN INTENSITY at WAVE = ', i6,': after ',
.          i2, ' iterations, ', 'error = ', f6.4/
.          ' i', 2x, 'tau_rte', 4x, 'Flux', 6x, 'XJ',
.          6x, 'Planck', 6x, 'S', 5x, 'kaplam',
.          2x, 'THOMSON')
        i = 1
        write (nwrite,1003) (i, tau_rte(i), FLUXsc, XJ(i),
.          Planck(i),slam(i),kaplam(i),
.          THOMSON(i),i=1,ntau)
1003  format (i3, 1p7e10.3)

C*** Conversion of global variables to MOOG format (Flux(lambda, T))
        write (nwrite,'(A)') 'Conversion to MOOG format'
        do i=1,ntau
            slamMOOG(i) = 2.9977518E26*(1/(wave**2))

```

```
>          *slam(i)
          xjMOOG(i) = 2.9977518E26*(1/(wave**2))
>          *XJ(i)
          fluxMOOG = 2.9977518E26*(1/(wave**2))
>          *FLUXsc
          write (nwrite, '(i2, 1p7e10.3)') i, slamMOOG(i), xjMOOG(i),
>
          fluxMOOG
enddo
```

RETURN

END

nwrite(*,*) 'Shall we play a game?'

nwrite(*,*) 'How about Global Thermonuclear Warfare?'

nwrite(*,*) 'Wouldn't you prefer a good game of chess?'

Bibliography

- [1] Adams, D. L., & Whaling, W. 1981, *J. Opt. Soc. Am.*, 71 , 1036
- [2] Allende Prieto, C., Barklem, P. S., Lambert, D. L., & Cunha, K. 2004, *Å*, 420, 183
- [3] Anders, E., & Grevesse, N. 1989, *Geochim. Cosmochim. Acta*, 53, 197
- [4] Anstee, S.D., O'Mara, B. J., & Ross, J. E. 1997, *MNRAS*, 284, 202
- [5] Aoki, W., Honda, S., Beers, T. C., Kajino, T., Ando, H., Norris, J. E., Ryan, S. G., Izumiura, H., Sadakane, K., & Takada-Hidai, M. 2005, *ApJ*, 632, 611
- [6] Asplund, M., Nordlund, A., Trampedach, R., & Stein, R. F. 2000, *A&A*, 359, 743
- [7] Asplund, M., Grevesse, N., Sauval, A. J., Allende Prieto, C., & Kiselman, D. 2004, *A&A*, 417, 751
- [8] Asplund, M., Grevesse, N., & Sauval, A. J. 2005a, *ASPC*, 336, 117
- [9] Asplund, M. 2005b, *ARA&A*, 43, 481
- [10] Auer, L. H. 1984, *Methods in Radiative Transfer*, ed. W. Kalkofen, Cambridge: University Press

- [11] Auer, L. H., & Paletou, F. 1994, *A&A*, 285, 675
- [12] Barklem, P. S., Anstee, S. D., & O'Mara, B. J. 1998, *PASA*, 15, 336
- [13] Barklem, P. S., Piskunov, N., & O'Mara, B. J. 2000, *A&AS*, 142, 467
- [14] Barklem, P. S., & Aspelund-Johansson, J. 2005, *A&A*, 435, 373
- [15] Becker, U., Bucka, H., & Schmidt, A. 1977, *A&A*, 59, 145
- [16] Bernstein, R., Shectman, S. A., Gunnels, S. M., Mochnacki, S., & Athey, A. E. 2003, *Proc. SPIE*, 4841, 1694
- [17] Beynon, T. G. R. 1978, *A&A*, 64, 145
- [18] Biemont, E. 1974, *Sol. Phys.*, 38, 15
- [19] Biemont, E., Grevesse, N., & Huber, M. C. E. 1978, *Sol. Phys.*, 67, 87
- [20] Biemont, E., Baudoux, M., Kurucz, R. L., Ansbacher, W., & Pinnington, E. H. 1991, *A&A*, 249, 1991
- [21] Blackwell, D. E., Petford, A. D., Shallis, M. J., & Simmons, G. J. 1982, *MNRAS*, 199, 43
- [22] Blackwell, D. E., Menon, S. L. R., & Petford, A. D. 1984a, *MNRAS*, 207, 533
- [23] Blackwell, D. E., Booth, A. J., & Petford, A. D. 1984b, *A&A*, 132, 236
- [24] Blackwell, D. E., Booth, A. J., Menon, S. L. R., & Petford, A. D. 1986, *MNRAS*, 220, 303
- [25] Blackwell, D. E., Booth, A. J., Menon, S. L. R., & Petford, A. D. 1987, *A&A*, 180, 229

- [26] Blackwell, D. E., Lynas-Gray, A. E., & Smith, G. 1995, 296, 217
- [27] Booth, A. J., Shallis, M. J., & Wells, M. 1983, MNRAS, 205, 191
- [28] Booth, A. J., Blackwell, D. E., & Shallis, M. J. 1984, MNRAS, 209, 77
- [29] Brault, J. W. 1976, J. Opt. Soc. Am., 66, 1081
- [30] Buonanno, R., Corsi, C. E., & Fusi Pecci, F. 1985, A&A, 145, 97
- [31] Butler, R. P., Marcy, G. W., Williams, E., Hauser, H., & Shirts, P. 1997, ApJ, 474, 115
- [32] Carretta, E., Cohen J. G., Gratton, R. G. & Behr, B. B. 2001, AJ, 122, 1469
- [33] Carretta, E., Bragaglia, A., Gratton, R.G., & Tosi, M. 2005, *Å*, 441, 131
- [34] Caretta, E. et al. 2006, in preparation
- [35] Castelli, F., Gratton, R. G., & Kurucz, R. L. 1997, *Å*, 318, 841
- [36] Cayrel, R., Depagne, E., Spite, M., Hill, V., Spite, F., Francois, P., Plez, B., Beers, T., Primas, F., Andersen, J., Barbuy, B., Bonifacio, P., Molaro, P., & Nordstrom, B. 2004, A&A, 416, 1117
- [37] Chamberlain, J. W., & Aller, L. H. 1951, ApJ, 114, 52
- [38] Chen, Y. Q., Zhao, G., Nissen, P. E., Bai, G. S., & Qiu, H. M. 2003, ApJ, 591, 925
- [39] Cohen, J. G. 1978, ApJ, 223, 487
- [40] Cohen, J. G. 2004a, AJ, 127, 1545

- [41] Cohen, J. G., Christlieb, N., McWilliam, A., Shtetman, S., Thompson, I., Wasserburg, G. J., Ivans, I. I., Dehn, M., Karlsson, T., & Melendez, J. 2004b, *ApJ*, 612, 1107
- [42] Condon, E. U., & Shortley, G. H. 1935, *The Theory of Atomic Spectra*, Cambridge: University Press
- [43] Condon, E. U., & Shortley, G. H. 1959, *The Theory of Atomic Spectra*, Cambridge: University Press
- [44] Cooper, J. C., Gibson, N. D., & Lawler, J. E. 1997, *J. Quant. Spec. Rad. Trans.*, 58, 85
- [45] Corliss, C. H., & Bozman, W. R. 1962, *Experimental Transition Probabilities for the Spectral Lines of Seventy Elements*, U. S. Natl. Bur. Standards Monograph 53, (Washington: U. S. Government Printing Office)
- [46] Cowan, R. D. 1981, *The Theory of Atomic Structure and Spectra*, Univ. of California Press, Berkeley
- [47] Cowley, C., Weise, W. L., Fuhr, J., & Kuznetsova, L. A. 2000, *Allen's Astrophysical Quantities*, ed. A.N. Cox, Springer-Verlag, 53
- [48] Dalgarno, A., & Williams, D. A. 1962, *ApJ*, 136, 690
- [49] Danzmann, K., & Kock, M. 1982, *J. Opt. Soc. Am.*, 72 1556
- [50] Delbouille, L., Roland, G., & Neven, L. 1973, *Photometric Atlas of the Solar Spectrum from λ 3000 to λ 10000* (Liège, Inst. D'Ap., Univ. de Liège)
- [51] Delbouille, L., Roland, G., & Neven, L. 1990, *Liege: Universite de Liege Institut d'Astrophysique*

- [52] Denissenkov, P. A. & Weiss, A. 2004, ApJ, 603, 119
- [53] Feautrier, P. 1964, SAO Special Report, 167, 80
- [54] Feltzing, S., & Gustafsson, B. 1998, A&AS, 129, 237
- [55] Fitzpatrick, M. J. & Sneden, C. 1987, BAAS, 19, 1129
- [56] Francois, P., Depagne, E., Hill, V., Spite, M., Spite, F., Plez, B., Beers, T. C., Barbuy, B., Cayrel, R., Andersen, J., Bonifacio, P., Molaro, P., Nordström, B., & Primas, F. 2003, A&A, 403, 1105
- [57] Friel, E. D., Jacobson, H. R., Barrett, E., Fullton, L., Balachandran, S. C., & Pilachowski, C. 2003, AJ, 126, 2372
- [58] Fulbright, J. P. 2000, AJ, 120, 1841
- [59] Gonzalez, G., & Wallerstein, G. 1998, AJ, 116, 765
- [60] Gonzalez, G., & Wallerstein, G. 2000, PASP, 112, 1081
- [61] Gratton, R. G. 1989, A&A, 208, 171
- [62] Gratton, R. G., & Sneden, C. 1991, A&A, 241, 501
- [63] Gratton, R. G., Carretta, E., Claudi, R., Lucatello, S., & Barbieri, M. 2003, A&A, 404, 187
- [64] Gratton, R. G., Sneden, C., & Carretta, E. 2004, ARA&A, 42, 385
- [65] Gray, D. F. 1976, The Observation and Analysis of Stellar Photospheres, Wiley: New York
- [66] Grevesse, N., Noels, A., & Sauval, A. J. 1996, ASPC, 99, 117

- [67] Grevesse, N., & Sauval, A. J. 1998, *Space Sci. Rev.*, 85, 161
- [68] Grevesse, N., & Sauval, A. J. 1999, *A&A*, 347, 348
- [69] Grigoriev, I. S., & Melikhov, E. Z. 1997, *Handbook of Physical Quantities* (Boca Raton, CRC Press)
- [70] Grundahl, F., Briley, M., Nissen, P. E., & Feltzing, S. 2002, *A&A*, 385, L14
- [71] Gustafsson, B., Bell, R. A., Eriksson, K. & Nordlund, A. 1975, *A&A*, 42, 407
- [72] Gustafsson B., Edvardsson B., Eriksson K., Mizuno-Wiedner M., Jorgensen U. G., & Plez B. 2002, *ASP Conf. Ser. Vol. 288*, (I.Hubeny, D.Mihalas, K.Werner eds.), p. 331
- [73] Halenka, J. & Grabowski, B. 1986, *A&AS*, 64, 496
- [74] Hannaford, P., & Lowe, R. M. 1981, *J. Phys. B*, 14, L5
- [75] Hannaford, P., Lowe, R. M., Grevesse, N., & Noels, A. 1992, *A&A*, 259, 301
- [76] Hashiguchi, S., & Hasikuni, M. 1985, *J. Phys. Soc. Japan*, 54, 1290
- [77] Helfer, H. L., Wallerstein, G., & Greenstein, J. L. 1960, *ApJ*, 132, 553
- [78] Heilig, K., & Wendlandt D. 1967, *Phys. Lett. A*, 25, 277
- [79] Holweger, H., & Müller, E. A. 1974, *Sol. Phys.*, 39, 19
- [80] Heise, C., & Kock, M. 1990, *A&A*, 230, 244
- [81] Holweger, H., Heise, C., & Kock, M. 1990, *A&A*, 232, 510
- [82] Holweger, H., Bard, A., Kock, A., & Kock, M. 1991, *A&A*, 249, 545

- [83] Holweger, H., Kock, M., & Bard, A. 1995, *A&A*, 296, 233
- [84] Hubeny, I. 1997, *Stellar Atmospheres: Theory and Observations*, 497, 1
- [85] Irwin, A. W. 1981, *ApJS*, 45, 621
- [86] Ivans, I. I., Sneden, C., Kraft, R. P., Suntzeff, N. B., Smith, V. V., Langer, G. E. & Fulbright, J. P. 1999, *AJ*, 118, 1273
- [87] Ivans, I. I., Kraft R. P., Sneden, C., Smith, G. H., Rich, R. M. , & Shetrone, M. 2001, *AJ*, 122, 1438
- [88] Ivans, I. I., Simmerer, J., Sneden, C., Lawler, J. E., Cowan, J. J., Gallino, R., & Bisterzo, S. 2006, *ApJ*, 645, 613
- [89] Iwamoto, K., Brachwitz, F., Nomoto, K., Kishimoto, N., Umeda, H., Hix, W. R., & Thieleman, F. K. 1999, *ApJS*, 125, 439
- [90] Janes, K. A., & Phelps, R. L. 1994, *AJ*, 108, 1773
- [91] Johnson, J. A. 2002, *ApJS*, 139, 219
- [92] King, J. R., Stephens, A., Boesgaard, A. M., & Deliannis, C. P. 1998, *AJ*, 115, 666
- [93] Korn, A. J. 2004, *Carnegie Centennial Symposium: Origin and Evolution of the Elements*
- [94] Kraft, R. P., Sneden, C., Langer, G. E., Shetrone, M. D., & Bolte, M. 1995, *AJ*, 109, 2586
- [95] Kraft, R. P., Sneden, C., Smith, G. H., Shetrone, M. D., Langer, G. E., & Pilachowski, C. A. 1997, *AJ*, 113, 279

- [96] Kraft, R. P., Sneden, C., Smith, G. H., Shetrone, M. D. & Fulbright, J. 1998, AJ, 115, 1500
- [97] Kraft, R. P., & Ivans, I. I. 2003, PASP, 115, 143
- [98] Kunasz, P., & Auer, L. H. 1988, J. Quant. Spect. Rad. Trans., 39, 67
- [99] Kupka F., Piskunov N.E., Ryabchikova T.A., Stempels H.C., & Weiss W.W. 1999, A&AS, 138, 119
- [100] Kurucz, R. L., & Peytremann, E. 1975, SAO Special Report No. 362, Part 1
- [101] Kurucz, R. L. 1993, Kurucz CD-ROM 13, ATLAS 9 (Cambridge:SAO)
- [102] Kwiatowski, M., Micali, G., Werner, K., & Zimmerman, P. 1981, A&A, 103, 108
- [103] Kwong, H. S., & Measures, R. M. 1980, Appl. Opt., 19, 1025
- [104] Laird, J. B., Rupen, M. P., Carney B. W., & Latham, D. W. 1988, AJ, 96, 1908
- [105] Lederer, M. C., & Shirely, V. S. 1978, Table of Isotopes, 7th ed. (New York: Wiley)
- [106] Lee, H.-W., & Kim, H. I. 2004, MNRAS, 347, 802
- [107] Lee, H.-W. 2005, MNRAS, 358, 1472
- [108] Lee, J. W., & Carney, B. W. 2002, AJ, 124, 1511
- [109] Limongi, M., & Chieffi, A. 2005,
- [110] Lodders, K. 2003, AJ, 591, 1220

- [111] Luck, R. E., & Heiter, U. 2005, *AJ*, 129, 1063
- [112] Magain, P. 1989, *A&A*, 209, 211
- [113] Marek, J., & Richter, J. 1973, *A&A*, 26, 155
- [114] Marek, J. 1975, *A&A*, 44, 69
- [115] Martin, G. A., Fuhr, J. R., & Wiese, W. L. 1988, *J. Phys. Chem. Ref. Data* 17, Suppl. 3
- [116] Martin, W. C., Fuhr, J. R., Kelleher, D. E., Musgrove, A., Sugar J., Wiese, W. L., Mohr, P. J., & Olsen, K. 1999, *NIST Atomic Spectra Database, Version 2.0* (Gaithersburg: NIST)
- [117] McWilliam, A., Preston, G. W., Sneden, C., & Searle, L. 1995, *AJ*, 109, 2757
- [118] McWilliam, A. 1997, *ARA&A*, 35, 503
- [119] McWilliam, A., Rich, M. R., & Smecker-Hane, T. A. 2003, *ApJ*, 592, L21
- [120] McWilliam, A., & Rich, M. R. 2004, *Carnegie Centennial Symposium: Origin and Evolution of the Elements*
- [121] Measures, R. M., Drewell, N., & Kwong, H. S. 1977, *Phys. Rev. A.*, 16, 1093
- [122] Mihalas, D., Auer, L. H., & Mihalas, B. R. 1978, *ApJ*, 220, 1001
- [123] Milford, P. N., O'Mara, B. J., & Ross, J. E. 1994, *A&A*, 292, 276
- [124] Mishenina, T. V., Kovtyukh, V. V., Soubraïn, C., Travaglio, C., & Busso, M. 2002, *A&A*, 396, 189
- [125] Moore, C. E., Minnaert, M. G. J., & Houtgast, J. 1966, *The Solar Spectrum 2935 Å to 8770 Å NBS Monograph 61* (Washington: U. S. G. P. O.)

- [126] Nakamura, T., Umeda, H., Nomoto, K., Thielmann, F. K., & Burrow, A. 1999, *ApJ*, 517, 193
- [127] Nilsson, H., Ljung, G., Lundberg, H., & Nielsen, K. E. 2006, *A&A*, 445, 1165
- [128] Norris, J. E., & Da Costa, G. S. 1995, *ApJ*, 447, 680
- [129] O'Brian, T. R., Wickliffe, M. E., Lawler, J. E., Whaling, W., & Brault, J. W. 1991, *J. Opt. Soc. Am. B*, 8, 1185
- [130] O'Mara, B. J., & Barklem, P. S. 2003, *Proc. 12th Cambridge Workshop on Cooler Stars, Stellar Systems, & The Sun*, 1097 (Colorado)
- [131] Otsuki, K., Honda, S., Aoki, W., Kajino, T., & Mathews, G. J. 2006, *ApJ*, 641, L117
- [132] Pauls, U., Grevesse, N., & Huber, M. C. E. 1990, *A&A*, 231, 536
- [133] Preston, G. W., Sneden, C., Thompson, I. B., Sackett, S. A., & Burley, G. S. 2006, *AJ*, 132, 85
- [134] Prochaska, J. X., & McWilliam, A. 2000, *ApJ*, 537, 57
- [135] Prochaska, J. X., Naumov, S. O., Carney, B. W., McWilliam, A., & Wolfe, A. M. 2000, *AJ*, 120, 2513
- [136] Raassen, A. J. J., & Uylings, P. H. M. 1998, *A&A*, 340, 300
- [137] Ramírez, I., & Meléndez, J. 2005, *ApJ*, 626, 465
- [138] Ramirez, S. V., & Cohen, J. G. 2002, *ApJ*, 123, 3277
- [139] Reddy, B. E., Tomkin, J., Lambert, D. L., & Allende Prieto, C. 2003, *MNRAS*, 340, 304

- [140] Reddy, B. E., Lambert, D. L., & Allende Prieto, C. 2006, MNRAS, submitted
- [141] Ryan, S. G., Norris, J. E., & Bessell, M. S. 1991, AJ, 102, 303
- [142] Samland, M. 1998, ApJ, 496, 155
- [143] Schnabel, R., Kock, M. & Holweger, H. 1999, A&A, 342, 610
- [144] Shchukina, N. & Trujillo Bueno, J. 2001, ApJ, 550, 970
- [145] Shetrone, M. D., Bolte, M., & Stetson, P. B. 1998, AJ, 115, 1888
- [146] Shetrone, M. D., & Keane, M. J. 2000, AJ, 119, 840
- [147] Simmerer, J. A., Sneden, C, Ivans, I. I., Kraft, R. P., Shetrone, M. D., & Smith, V. V. 2003, AJ, 125, 2018
- [148] Simmerer, J. A., Sneden, C., Cowan, J. J., Collier, J., Woolf, V. M., & Lawler, J. E. 2004, ApJ, 617, 1091
- [149] Simmons, G. J., & Blackwell, D. E. 1982, A&A, 112, 209
- [150] Smith, G. H., Sneden, C., & Kraft, R. P. 2002, AJ, 123, 1502
- [151] Sneden, C. 1973, ApJ, 184, 839
- [152] Sneden, C, Gratton, R. G., & Crocker, D. A. 1991a, A&A, 246, 354
- [153] Sneden, C., Kraft, R. P., Prosser, C. F., & Langer, G. E. 1991b, AJ, 102, 2001
- [154] Sneden, C., Kraft, R. P., Langer, G. E., Prosser, C. & Shetrone, M. 1994, AJ, 107, 1773
- [155] Sneden, C., Preston, G. W., McWilliam, A., & Searle, L. 1994, ApJ, 431, L27

- [156] Sneden, C., Kraft, R. P., Shetrone, M. D., Smith, G. H., Langer, G. E., & Prosser, C. F. 1997 AJ, 114, 1964
- [157] Sneden, C., Johnson, J., Kraft, R. P., Smith, G. H., Cowan, J. J., & Bolte, M. S. 2000, ApJ, 536, L85
- [158] Sneden, C., Kraft, R. P., Prosser, C. F., & Langer, G. E. 1991, AJ, 102, 2001
- [159] Sneden, C., Cowan, J. J., Lawler, J. E., Ivans, I. I., Burles, S., Beers, T. C., Primas, F., Hill, V., Truran, J. W., Fuller, G. M., Pfeiffer, B., & Kratz, K. L. 2003, ApJ, 591, 936
- [160] Sneden, C., Kraft, R. P., Guhathakurta, P., Peterson, R., & Fulbright, J. P. 2004, AJ, 127, 2162
- [161] Sugar, J., & Corliss, C. 1985, J. Phys. Chem. Ref. Data 14 Suppl., 2, 264
- [162] Takeda, Y., Hashimoto, O., Taguchi, H., Yoshioka, K., Takada-Hidai, M., Saito, Y., & Honda, S. 2005, PASJ, 57, 751
- [163] Thevenin, F. 1990, A&AS, 82, 179
- [164] Thevenin, F., & Idiart, T. P. 1999, ApJ, 521, 753
- [165] Thielemann, F. K., Nomoto, K., & Hashimoto, M. 1996, ApJ, 460, 408.
- [166] Timmes, F. X., Woosley, S. E., & Weaver, T. A. 1995, ApJS, 98, 617
- [167] Tozzi, G. P., Brunner, A. J., & Huber, M. C. E. 1985, MNRAS, 217, 423
- [168] Truran, J. W., Cowan, J. J., Pilachowski, C. A., & Sneden, C. 2002, PASP, 114, 1293

- [169] Tull, R. G., MacQueen, P. J., Sneden, C., & Lambert, D. L. 1995, *PASP*, 107, 251
- [170] Umeda, H. & Nomoto, K. 2002, *ApJ*, 565, 385
- [171] Valenti, J. A. & Fischer D. A. 2005, *ApJS*, 159, 141
- [172] Vogt, S. S. 1987, *PASP*, 99, 1214
- [173] Vogt, S. S. et al. 1994, *Proc. SPIE*, 2198, 362
- [174] Wallerstein, G. 1962, *ApJS*, 6, 407
- [175] Whaling, W., Carle, M. T., & Pitt, M. L. 1993, *J. Quant. Spec. Rad. Trans.*, 50, 7
- [176] Wickliffe, M. E., Lawler, J. E., & Nave, G. 2000, *J. Quant. Spec. Rad. Trans.*, 66, 363
- [177] Wolnik, S. J., Berthel, R. O., Larson, G. S., Carnevale, E. H., & Wares, G. W. 1968, *Phys. Fluids*, 11, 1002
- [178] Wolnik, S. J., Berthel, R. O., Carnevale, E. H., & Wares, G. W. 1969, *ApJ*, 157, 983
- [179] Wolnik, S. J., Berthel, R. O., & Wares, G. W. 1970, *ApJ*, 162, 1037
- [180] Woosely, S. E., & Weaver, T. A. 1995, *ApJS*, 101, 181
- [181] Wujec, T., & Weniger, S. 1981, *J. Quant. Spec. Rad. Trans.*, 25, 167
- [182] Yong, D., Grundahl, F., Nissen, P. E., Jensen, H. R., & Lambert, D. L. 2005, *A&A*, 438, 875

[183] Zoccali, M., Barbuy, B., Hill, V., Ortolani, S., Renzini, A., Bica, E., Momany, Y., Pasquini, L., Minniti, D., & Rich, R. M. 2004, *A&A*, 423, 507

Vita

Jennifer Sunshine Sobeck was born in Delray Beach, Florida on July 26, 1974, the daughter of Charles Sobeck and Michele Ellison Sobeck (sister of Christina Sobeck Henninger). She graduated from the University of Texas at Austin in December 1996 with a Bachelor of Science Degree in Physics. With the desire to obtain a Ph.D. in Biophysics, Jennifer attended both the University of Texas at Houston Graduate School of Biomedical Sciences and Rice University in 1997 and 1998. After some introspection, she decided to leave the UT Houston graduate program. In the summer of 1999, Jennifer enrolled as a full-time graduate student at the University of Texas of Austin in pursuit of a Physics Ph.D. She married Emre Kadri in April 2004.

Permanent Address: 525 Village View Drive
Canyon Lake, Texas 78133

This dissertation was typeset with $\text{\LaTeX} 2_{\epsilon}$ ¹ by the author.

¹ $\text{\LaTeX} 2_{\epsilon}$ is an extension of \LaTeX . \LaTeX is a collection of macros for \TeX . \TeX is a trademark of the American Mathematical Society. The macros used in formatting this dissertation were written by Dinesh Das, Department of Computer Sciences, The University of Texas at Austin, and extended by Bert Kay, James A. Bednar, and Ayman El-Khashab.